Description of Ultra-High wind-wave-solar hindcast models
D6.6

Baki, B.; Alday Gonzalez, M.F.; Lavidas, G.

Publication date
2024

Document Version
Final published version

Citation (APA)
Baki, B., Alday Gonzalez, M. F., & Lavidas, G. (2024). *Description of Ultra-High wind-wave-solar hindcast models: D6.6*. European Scalable Offshore Renewable Energy Source.

European Scalable Offshore Renewable Energy Source (EU-SCORES)

D6.6 'Description of Ultra-High wind-wave-solar hindcast models'

Delivery Date 03/06/2024
Dissemination Level PU
Status DELIVERED
Version FINAL
Keywords WRF, WW3, SWAN, hindcast, wave energy, solar, wind energy, resource assessments

Disclaimer

Document Information

Grant Agreement Number	101036457
Project Acronym	EU-SCORES
Work Package	WP6
Related Task(s)	Task 6.1, 6.2
Deliverable	D 6.6
Title	Description of Ultra-High wind-wave-solar hindcast models
Author(s)	Harish Baki Matias Alday Gonzalez George Lavidas
File name	D6.6_EU-SCORES_FINAL

Revision History

Revision	**Date**	**Description**	**Reviewer**
01	26/02/2024	TUD revision	George Lavidas
02	15/03/2024	TUD revision	Harish Baki Matias Alday-Gonzalez
03	25/03/2024	TUD revision	George Lavidas
04	27/05/2024	Consortium revision	All partners
05	01/06/2024	Final	George Lavidas Matias Alday-Gonzalez Harish Baki

This project has received funding from the Europeans Union's Horizon 2020 research & innovation programme under grant agreement number 101036457.

Contents

This project has received funding from the Europeans Union's Horizon 2020 research & innovation programme under grant agreement number 101036457.

This project has received funding from the Europeans Union’s Horizon 2020 research & innovation programme under grant agreement number 101036457.

This project has received funding from the Europeans Union's Horizon 2020 research & innovation programme under grant agreement number 101036457.

This project has received funding from the Europeans Union’s Horizon 2020 research & innovation programme under grant agreement number 101036457.

This project has received funding from the Europeans Union's Horizon 2020 research & innovation programme under grant agreement number 101036457.

Executive summary

Renewable energy project require long term climate information, offshore renewable energies in particular are in need of higher fidelity information as both power production, reliability and survivability rely on them. Existing open source datasets are too coarse, and often do not have the suitable physics based solutions to resolve high fidelity areas.

While for power production different datasets may be needed wind speeds, solar radiation, ambient temperature, metocean conditions, the common thread is that all information provided by often open source free dataset carry large deviations that can be catastrophic or under-estimate power production significantly.

This deliverable aims to bridge the gap and offer the EU-SCORES project three custom models wind, solar, wave and are then used for ultra high-fidelity assessment (sub 500m). The physical parametrisation are specifically calibrated with the need of EU-SCORES, and the models are intensively validated against in-situ and satellite information. This report describes the different models used for the construction of the open-source databases for wind-wave-solar information, from 1990-2021. All models have been developed, calibrated and validated against in-situ measurements, providing with the uncertainty levels for the hindcasts.

The physics behind the wave model were specifically tuned for the Atlantic region and considered, winds, surface currents, tidal levels& currents, ice concentration and coastal orography. The validation against satellite significant wave height (H_{m0}) overall showed that the wave hindcast ECHOWAVE, achieved a normalised mean bias 0-4%, a scatter index (SI) ≈10%, with large waves >10 m having a difference ≈6% in the coastal shelf. Validation with H_{m0} buoy data in shallow coastal locations showed enhanced performance, when compared to open source datasets, for most locations there is a small positive bias of ≈0.1-0.2 m and a SI ≈10-12%, proving that the physical parametrisation in ECHOWAVE produce reliable data. Similarly for the peak wave period (Tp) at several locations and years, the bias is slightly over-estimated ≈1-3 sec and with SI ≈12-20%.

For the wind model the parametrisations were adjusted considering Terrestrial Data, Meteorological Gridded Data, and Observational Data that allowed to simulate phenomena such as Low Level Jets much better than expected. The boundary information used a state-of-the-at 5 Km climate input, that allowed to efficiently reach the 500m desired resolution, resolving the physical aspects better. Unlike wave buoy data, wind mast long-term conditions in the offshore regions are rare. The validation of the models used a mix of wind mast and wind power produced data (where available), and ERA5 to have a direct comparison. With regards to wind at all the different regions our model showed only a slight under-estimation of ≈0.2-0.7 m/s, inline closer to observation, while the ERA5 dataset showed a large under-estimation ≈2-4 m/. In addition, our models manage to represent wind speeds >13m/s much better than ERA5. In terms of power production, our custom model replicated impacts of Low Level Jets better than with only slight over-estimated 200MW. ERA5 missed the impact on power production, over-estimating by 600 MW.

This project has received funding from the Europeans Union's Horizon 2020 research & innovation programme under grant agreement number 101036457.

For the solar model, a special module extending the capabilities of the atmospheric model was employed, as in line with international literature. For the EU-SCORES database cloud effects on shortwave radiation is activated, as well as convection. Similarly, offshore solar measurements are rare, but in-situ buoys data of atmospheric conditions were used to validate the model such as air temperature, and also cross compared with ERA5. Across all the different high fidelity regions our built data have a higher correlation ≈97-99%, a SI 7-9%, and negligible biases 0.1-0.3 Celcius.

This project has received funding from the Europeans Union’s Horizon 2020 research & innovation programme under grant agreement number 101036457.

1 Wave Energy Resource Assessment

1.1 Limitations of Existing Wave Databases

One of the main sources of uncertainty in the estimation of the available wave power, is related to the accuracy of the used data. This is the main reason why the creation and usage of a dataset specially adjusted and validated is the first step to properly develop a wave energy resource assessment.

Currently there are several global reanalysis or hindcasts available to the scientific and engineering community (Alday, Accensi, Ardhuin, & Dodet, 2021; Accensi, et al., 2021; Hersbach H. a.-S., 2020; Rascle & Ardhuin, 2013; Chawla, Spindler, & Tolman, Validation of a thirty year wave hindcast using the Climate Forecast System Reanalysis winds, 2013). These datasets provide extensive spatial and temporal coverage. They represent a useful source to draw an initial mapping of the wave resource, but there are some important limitations to consider when interpreting the results of an analysis based on these data sources.

The first, and probably most obvious limitation when it comes to global models, is the spatial resolution, typically ranging from 0.5° to 0.25° (~0.3° in the case of the ERA5 wave product), which is equivalent to ~55 km to ~27 km. Thus, it could be generalized that the closest output from the models' gridded data is about 20 to 30 km offshore. In most cases this corresponds to deep water conditions, where wave propagation is not affected by interactions with the surrounding bathymetry. Additionally, the main objectives behind these different datasets are different. Which implies that specific attention is paid to a wide range of elements, ranging from temporal and spatial resolution to wave breaking and its effect in ocean-atmosphere gas exchange.

In this section, the implementation, adjustment and validation of a high resolution wave hindcast specially developed for the European North Atlantic coasts is presented.

1.2 High resolution wave model for European coasts

A high resolution spectral wave model has been implemented, adjusted and validated for North Atlantic European waters using the WAVEWATCH III modelling framework (The WAVEWATCH III® Development Group, 2019). The main aim of this implementation, is to generate a database adequate for the assessment of the available wave resource within intermediate to shallow water conditions. To achieve this, the following steps have been considered:

1. Selection of the bathymetry and forcing fields sources.
2. Definition of the model nesting scheme and discretization (spatial and spectral).
3. Adjustment of the physical parameterizations to improve performance of the sea states' simulations.
4. Validation of the generated sea states with altimeter and buoy data.

It is important to highlight that the generation of a high quality wave dataset for a specific coastal region, starts by assessing the sea states' characteristics in open

This project has received funding from the Europeans Union's Horizon 2020 research & innovation programme under grant agreement number 101036457.

ocean (or deep waters) conditions. Which is why the adjustments of physical parameterizations at basin scale is key is so important, especially in a nesting scheme where boundary conditions are first defined in deep waters. The local wave climate, and thus the quantification of the wave resource, in coasts exposed to the North Atlantic swells (e.g.; Portugal, Ireland and Northern Scotland) are the most affected by the quality of the boundary conditions used (Alday, Ardhuin, Dodet, & Accensi, 2022).

In the following sections, details on the wave model setup, adjustments and validation of the 32 years (1990 to 2021) generated dataset, ECHOWAVE (**E**uropean **C**oasts **H**igh resolution **O**cean **WAVE**s), are provided.

The total required time to generate the ECHOWAVE dataset was ~4000 hrs of cpu usage. In average 1 year required a total of 432 cores (normally distributed in 9 hpc nodes).

1.2.1 The WAVEWATCH III model

WAVEWATCH III (from hereon WW3) is a third generation wave model originally developed at the US National Centers for Environmental Prediction (NOAA/NCEP), based on the initial work from Hendrik Tolman (Tolman, 1991; Tolman, 1992). To date, as the core of a modelling framework community, the model includes the latest developments in the field of wind-wave modelling dynamics, including processes of generation, propagation and different sources of dissipation.

WW3 solves the spectral action density balance equation, with the assumption that water depth, currents, as well as the wave field vary on time and space scales that are much larger than a single wavelength or period. Physical processes in the governing equation are incorporated as “source terms” which include parameterizations for: Wave growth due to the action of the wind, different forms to account for nonlinear wave to wave interactions and wave evolution, scattering caused by wave-bottom interactions, bottom friction, triad wave interactions, and dissipation effects due to whitecapping, depth induced breaking, and interactions with mud and ice.

The wave governing equation is solved in terms of the wave action (*N(k,ϑ)*) because in general, the wave action is conserved. In cartesian coordinates the wave action balance equation is expressed as follows:

Equation 1

$$\frac{DN(k,\theta)}{Dt} = \frac{\partial N}{\partial t} + \nabla_x \cdot \dot{x}N + \frac{\partial \dot{k}N}{\partial k} + \frac{\partial \dot{\theta}N}{\partial \theta} = \frac{S}{\sigma}$$

with

$$N = \frac{E(k,\theta,x,t)}{\sigma}$$

$$\sigma = 2\pi/T$$

$$x = c_g + U$$

$$\dot{k} = \frac{\partial \sigma}{\partial d}\frac{\partial d}{\partial s} - k \cdot \frac{\partial U}{\partial s}$$

$$\dot{\theta} = -\frac{1}{k}\left[\frac{\partial \sigma}{\partial d}\frac{\partial d}{\partial m} + k \cdot \frac{\partial U}{\partial m}\right]$$

where *N* is the wave action, *E* the wave directional spectrum. *σ* is the relative (or intrinsic) radian frequency observed from a reference frame that moves with the mean current and ω is the absolute wave frequency observed from a fixed frame of reference. *T* is the wave period, d the mean depth, ***k*** is the wave number vector, and ***U*** the mean current vector depth and time averaged over the scale of individual waves. Then, $\boldsymbol{c_g} = (c_g\cos(\theta), c_g\sin(\theta))$ is the wave group celerity vector, *s* a local coordinate in the direction of θ and *m* a local coordinate perpendicular to *s*.

In Equation 1, the quasi-uniform linear wave theory is used considering slowly varying currents and depth changes. Thus, the following expression for the dispersion relation (Equation 2) and Doppler shift effect (Equation 3):

Equation 2 $$\sigma^2 = gk\,tanh\,(kd)$$

Equation 3 $$\omega = \sigma + k \cdot U$$

For large scale applications, Equation 1 is expressed in spherical coordinates:

Equation 4 $$\frac{\partial N}{\partial t} + \frac{1}{cos(\emptyset)}\frac{d}{d\emptyset}\dot{\emptyset}Ncos(\theta) + \frac{\partial}{\partial\lambda}N + \frac{\partial}{\partial k}\dot{k}N + \frac{\partial}{\partial\theta}\dot{\theta}N = \frac{S}{\sigma}$$

with $$\dot{\phi} = \frac{C_g\cos(\theta)+U_\phi}{R}$$

$$\dot{\lambda} = \frac{C_g\sin(\theta)+U_\lambda}{Rcos(\phi)}$$

Where R is the Earth's radius, λ the longitude, ϕ the latitude, and U_ϕ and U_λ are the projected current components.

On the right hand side of Equation 1 and Equation 4, ***S*** is the net source term which includes the effect of all parameterizations to account for energy input, spectral evolution, and sink terms (loss of energy from the waves). In deep waters there are typically 3: The wind input term $\boldsymbol{S_{in}}$ for atmosphere-wave interactions. The nonlinear interactions term $\boldsymbol{S_{nl}}$ to account for the wave-wave resonant mechanism, which is key for the transfer of energy from high to lower frequencies of the spectrum. And finally, the wave-ocean interactions term dominated by wave breaking dissipation $\boldsymbol{S_{ds}}$.

$\boldsymbol{S_{in}}$ describes better the dominant exponential wind-wave growth process, which is why for model initialization a linear input term $\boldsymbol{S_{ln}}$ is added to simulate a more realistic initial wave growth.

Within intermediate to shallow waters, other processes must be taken into account. These mainly include shoaling, depth-induced refraction, triads interactions $\boldsymbol{S_{tri}}$, energy dissipation due to bottom friction $\boldsymbol{S_{bot}}$,, or in very shallow water conditions depth-induced wave breaking $\boldsymbol{S_{db}}$.

Other source terms included in the WW3 implementation for EU-SCORES are wave-interactions $\boldsymbol{S_{ice}}$, and wave reflection at coastlines $\boldsymbol{S_{ref}}$. Taking into account all these parameterizations, the net source term can be expressed as:

Equation 5: $$S = S_{ln} + S_{in} + S_{nl} + S_{ds} + S_{bot} + S_{db} + S_{tri} + S_{ice} + S_{ref}$$

1.2.2 Model setup

The WW3 implementation was especially design to generate a reliable high resolution dataset for European waters that will allow to reduce uncertainties in the estimation of the available resource in intermediate to shallow waters. To that effect, the first important step is to define an adequate model setup, which allows to properly capture the sea states characteristics relevant for the intended application, and the use of affordable computing resources.

In this section the selected domain, nesting scheme, main parameterizations used and used forcing fields are described.

1.2.2.1 Model domain and nesting scheme

The model use a multi-grid system with a 2-way nesting scheme, which means that higher rank grids, in this case with higher resolution too, feed spectral information back to the lower rank grids (Chawla, et al., 2013; Tolman, 2008). Three regular grids have been defined with increasing resolution: The base grid N_ATL-15M with a spatial resolution of 0.25°, an intermediate grid for European waters (N_ATL-8M) with 0.125° resolution, and a coastal grid (EU_ATL-2M) with high spatial resolution of 0.03°. In Figure 1 is possible to observe the multi-grid nesting scheme layout. N_ATL-8M covers the full North Atlantic basin from latitude 0.25° to 80° North and provides boundary conditions to N_ATL-8M on deep waters, mostly outside the European coastal shelf. At the same time, N_ATL-8M provides boundary conditions to the coastal grid EU_ATL-2M with active computing nodes only in intermediate to shallow waters. Note that boundary conditions in N_ATL-8M and EU_ATL-2M are prescribed along the outer edge of the active nodes (see Figure 1.b). Details of the spatial resolution and extension of each grid are presented in Table 1.

All land features like islands, with surface smaller than a particular grid's resolution are treated like (sub-grid) blocking obstacles (Chawla & Tolman, 2008).

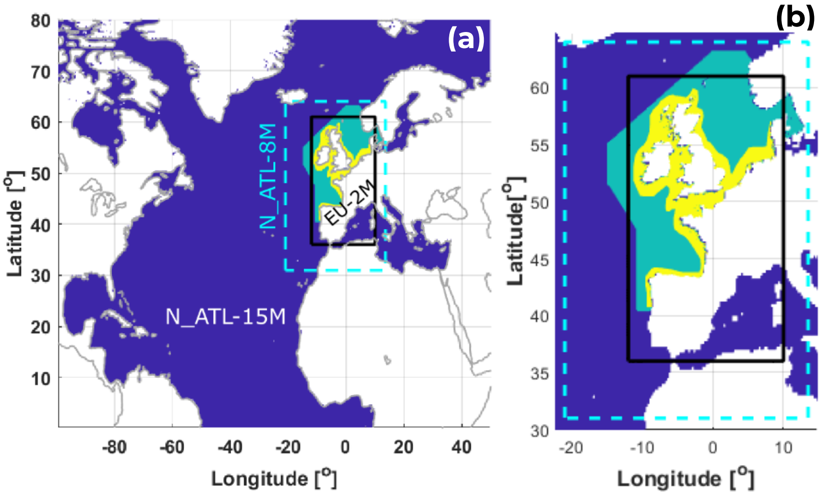

Figure 1: (a) Multi-grid nesting scheme adapted from Alday, et al. (2023). (b) Detail of N_ATL-8M and EU_ATL-2M.

Obs.: In blue, active nodes from N_ATL-15M. In cyan dashed lines the limits of N_ATL-8M, with its active nodes in green. Black lines show the limits of EU_ATL-2M, its active grid nodes in yellow. Computations are only perform on active grid nodes.

Table 1: Model grids details.

Grid Name	Grid Rank	Longitude [°]	Latitude [°]	Spatial resolution

		Min	Max	Min	Max	[°]	[m]
N_ATL-15M	1	-99.5	50.0	0.25	80.0	0.25	18125,0
N_ATL-8M	2	-21.0	64.0	31.0	64.0	0.125	9062,5
EU_ATL-2M	3	-12.0	10.0	36.0	61.0	0.03	2175,0

Obs.: Spatial resolution in m estimated for dx considering 1° as 72.5 km (at 50° latitude). Resolution in dy should be estimated using 1° = 111 km approx.

1.2.2.2 Parameterizations and numerical choices

The following main physical parameterizations have been considered in the model implementation:

1. Wind-wave growth, wave breaking and swell dissipation expressions from the WW3 ST4 parameterizations package (Ardhuin, et al., 2010; Lekler, Ardhuin, Filipot, & Mironov, 2013).
2. 4-wave nonlinear interactions are represented with the Discrete Interaction Approximation (DIA) to reduce computing time (Hasselmann & Hasselmann, 1985)
3. Wave scattering in sea ice with a wave-induced ice break-up (Boutin, Ardhuin, Dumont, Sévigny, & Girard-Ardhuin, 2018; Ardhuin, Otero, Merrifield, Grouazel, & Terrill, 2020) and dissipation below ice plates (Stopa, Ardhuin, & Girard-Ardhuin, 2016) from the IS2 and IC2 parameterizations packages.
4. Bottom friction effects are accounted with the SHOWEX parameterization (WW3 switch BT4), which includes sub-grid parameterization for the variability of water depth (Ardhuin, O'Reilly, Herbers, & Jessen, 2003; Tolman, 1995).
5. An ad hod constant 5% reflection is considered at coastlines using the REF1 parameterization switch (Ardhuin & Roland, 2012).

The complete list of switches use to activate parameterizations in the used WW3 implementation is included in Appendix A.

1.2.2.3 Forcing fields and bathymetry

Wind fields

Wind fields are the main forcing in the model for wave generation. In this case, the fifth generation ECMWF global atmospheric reanalysis, ERA5 (Hersbach, et al., 2020), is employed. This reanalysis was created with the Integrated Forecast System (IFS) model cycle 41r2, which includes 4D-var data assimilation. The amount of assimilated data ranges from 0.75 million measurements per day to ~24 million between 1979 to 2018. The dataset present hourly output of wind velocity components, *u* and *v*, at 10 m above sea level with a 0.25° spatial resolution (25 to 30 km approx.). This forcing filed is applied in all grids (N_ATL-15M, N_ATL-8M, EU_ATL-2M).

Global surface current

Global surface currents are included to account for changes in the effective wind vector, which is the result of the combined effects of the wind and the surface current vectors. In regions where the main current characteristics are well constrained, including them in the model help to improve wave generation and to account for current induced refraction at larger scales (Marechal & Ardhuin, 2021; Echevarria, Hemer, & Holbrook, 2021; Alday, Accensi, Ardhuin, & Dodet, 2021).

The global surface current fields are taken from the CMEMS-Globcurrent product[1]. This current field is the sum of geostrophic and Ekman components (Rio, Mulet, & Picot, 2014), using an updated mean dynamic topography (MDT) from CNES-CLS (Mulet, et al., 2021). The MDT is used to estimate surface currents when the geostrophic approach is used. This product has a spatial resolution of 0.25° with 3-hourly data. This forcing field is only applied to the N_ATL-15M grid.

Tidal levels and currents

Tidal currents become dominant within the European shelf, developing intensities that can be much larger than those induced by geostrophic currents, as it is for example in the English Channel, northern Scotland and the Irish sea. Tidal currents have a significant effect in wave advection, current induced refraction due to larger velocity gradients reduced spatial scales that can be of the order of the dominant wave lengths. Wave focusing and blocking, and induced breaking can occur as waves propagate against strong current jets with increasing velocities (Ardhuin, et al., 2012).

Tidal levels become more important in shallow water regions or in those areas with large tidal amplitude regimes where changes in the waves' propagation conditions are induced. Tidal currents and level fields are taken from the Atlantic European North West Shelf Ocean Physics Reanalysis product[2]. This product presents hourly data with a spatial resolution of ~7km (1/16°), and covers the North-West European coastal shelf (longitudes -19.89° to 12.99°, and latitudes 40.07° to 65.00°). Tidal current forcing is applied to N_ATL-8M and EU_ATL-2M. Tidal levels are only used in EU_ATL-2M, as it expresses a higher spatial representation near coastal areas with tidal resource.

Ice concentration

At high latitudes, ice coverage seasonal changes play an important role in wave dumping and scattering. Additionally, in the artic circle, changes in the ice coverage affect also the fetch extension for wind generation. To account for this effects, ice concentration data is taken from the Ifremer SSMI-derived daily product (Girard-Ardhuin & Ezraty, 2012). Due to limited knowledge on ice thickness distributions, a constant 1 m thickness was considered.

Bathymetry

High resolution bathymetry accurately describing intrinsic features in coastal areas, becomes more important in intermediate to shallow waters as waves interact with the sea bottom, which results in wave refraction and shoaling.

---

[1] Global Ocean Multi Observation Product, MULTIOBS_GLO_PHY_REP_015_004

[2] NWSHELF_MULTIYEAR_PHY_004_009 (https://doi.org/10.48670/moi-00059)

This project has received funding from the Europeans Union's Horizon 2020 research & innovation programme under grant agreement number 101036457.

Here, the GEBCO 2021 gridded bathymetry product is used. This product presents depth/elevation data referenced to the mean sea level (MSL), with a spatial resolution of 15 arc-second (~450 m).

1.3 Parameterizations' adjustments (model calibration)

To improve the model performance within the analysed area (with the described setup), it is necessary to make adjustments to the physical parameterizations used. In this case, these are mainly applied to the wind-wave growth and dissipation terms from the atmosphere-wave interactions parameterization (Ardhuin, et al., 2010). Here, only the expressions which terms are modified in the tuning process are included. The source term has the following expression:

Equation 6

$$S_{atm}(f,\theta) = S_{out}(f,\theta) + \frac{\rho_a}{\rho_w}\frac{\beta_{max}}{\kappa^2} exp(Z)\, Z^4 \left(\frac{u'_*}{C}\right)^2 \times max\{cos(\theta - \theta_u), 0\}^p \sigma F(f,\theta)$$

with S_{out} the energy flux from the ocean to the atmosphere representing the swell dissipation effect (Equation 7). This expression is based on observations of swell evolution from satellite data (Ardhuin, Chapron, & Collard, Observation of swell dissipation across oceans, 2009):

Equation 7

$$S_{out}(k,\theta) = r_{vis} S_{out,vis}(k,\theta) + r_{tur} S_{out,tur}(k,\theta)$$

where r_{vis} and r_{tur} are 2 the "weight" terms to give the relative importance of viscous and turbulent swell attenuation which effects are controlled by the ratio of the significant Reynolds Number Re and its critical value Re_c:

Equation 8

$$r_{vis} = 0.5[1 - tanh((Re - Re_c)/s7)]$$

Equation 9

$$r_{tur} = 0.5[1 + tanh((Re - Re_c)/s7)]$$

with $Re = 2u_{orb,s}H_s/\nu_a$

S_{out} includes the effects of the transitions from (linear) viscous boundary layer to (non-linear) turbulent boundary layer to account for the Rayleigh distribution of wave heights (Perignon, Ardhuin, Cathelain, & Robert, 2014). Particular adjustments are introduced to enhance the turbulent dissipation term in Equation 7 ($S_{out,tur}$) which has the following form:

Equation 10

$$S_{out,tur}(k,\theta) = \frac{\rho_a}{\rho_w}\left(16 f_e \sigma^2 u_{orb}/g\right) F(k,\theta)$$

with

$$f_e = s1\left(f_{e,GM} + [|s_3| + s_2 \cos(\theta - \theta_u)]u_*/u_{orb}\right)$$

In Equation 6, β_{max} is the non-dimensional wind-wave growth coefficient, ρ_a and ρ_w are the density of the air and the water respectively, and κ is the von Karman's constant. Then, $Z = \log(\mu)$, with μ the dimensionless critical height (Janssen, 1991), C is the phase celerity and u'_* is a frequency-dependent modified friction velocity used to reduce the wind input source term. θ is the wave direction, θ_u the wind direction, and as explained before, σ the wave relative frequency observed from a reference frame moving with the mean current.

In Equation 8 and Equation 9, s7 is a "tuneable" parameter used to change the range of wave heights with turbulent boundary layers over groups of larger waves

This project has received funding from the Europeans Union's Horizon 2020 research & innovation programme under grant agreement number 101036457.

and viscous boundary layer on the groups of lowest waves (Perignon, Ardhuin, Cathelain, & Robert, 2014). Equation 10, f_e includes the adjustable effects of wind speed on the surface roughness, where $f_{e,GM}$ is the Grant and Madsen's friction factor (Grant & Madsen, 1979) for rough oscillatory boundary layers without a mean flow. In particular,*s1* is an adjustable parameter of O(1) that can be used to enhance the effect of turbulent swell dissipation.

1.3.1 Performance parameters

To assess changes/improvements of the simulation related to changes introduced in the model parameterizations, the following expressions are used: The Normalized Mean Bias (NMB), the Scatter Index (SI), and the Hanna Heinhold index (HH).

Equation 11

$$\boldsymbol{NMB = 100\frac{\sum(X_{mod}-X_{obs})}{\sum X_{obs}}}$$

Equation 12

$$\boldsymbol{SI = \sqrt{\frac{[(X_{mod}-\overline{X_{mod}})-(X_{obs}-\overline{X_{obs}})]^2}{\sum {X_{obs}}^2}}}$$

Equation 13

$$\boldsymbol{HH = \sqrt{\frac{\sum(X_{mod}-X_{obs})^2}{\sum(X_{mod}X_{obs})}}}$$

From Equation 10 to Equation 13, X_{obs} and X_{mod} are the observed and modelled quantities respectively. For example significant wave heights, peak or mean periods. Overbars on top of variables denote the mean of the analysed quantity.

Is should be noticed that the HH index, also known as the "symmetrically normalized root mean squared error", has been chosen instead of the more known Normalized Root Mean Squared Error. The main reason for this , is that the HH index is less sensitive to the presence of large biases of fluctuations (Mentaschi, Besio, Cassola, & Mazzino, 2015), which is more common in model-measurement comparisons for wave heights larger than ~8 m. It is expected that the HH index together with the SI, will provide a more adequate idea of the random errors for large wave heights. It is also important to mention that, when comparing with altimeter data, attention is paid mainly to wave heights > 1.0 m. This is due to the poorer accuracy of altimeters for resolving smaller wave heights, which is related to the instruments' bandwidth limitations (Smith & Scharroo, 2015).

For most model-altimeter comparisons, the NMB, SI and HH index are computed for an along-track type analysis. To perform this analysis, wave height values from the closest 4 points of the model grid to an altimeter measurement location, are interpolated in time and space to collocate the model data along the altimeter track.

1.3.2 Adjustment effects at basin scale

The parameterization adjustment is based on the method described in Alday et al. (2021) for global scales. In this case the adjustments are applied to improve model performance in the North-East Atlantic first comparing modelled H_s fields with altimeter data from the ESA Sea State Climate Change Initiative (CCI) Version 3 product (Piolle, et al., 2022) and then verifying the results with H_s and T_p time series with a set of buoys placed mainly in deep and intermediate waters.

This project has received funding from the Europeans Union's Horizon 2020 research & innovation programme under grant agreement number 101036457.

All model-altimeter comparisons are done within a subregion that covers longitudes -40° to 37.5°, and latitudes 15° to 80°, excluding the Mediterranean, the Black, and Baltic Sea. This is done to verify how all changes introduced affect (improve) the sea states representation exclusively in the area of interest. All model "tuning" tests are done comparing 1-year simulations of significant wave heights (H_s) fields from the N_ATL-15M grid, with altimeter data from the Jason-2 altimeter. Jason-2 is selected since it is the altimeter used to intercalibrate all of the missions included in the CCI dataset (Dodet, et al., 2020)

The T475 parameterization values (Alday, Accensi, Ardhuin, & Dodet, 2021), are used as a starting point for the adjustments' sensitivity analysis. As done for the adjustments that lead to T475, the year 2011 was selected to perform the model tuning here. On the one hand, this allows to have a more direct comparison with the results previously obtained in Alday et. al (2021) and quantify the improvement of the model results with the proposed WW3 implementation. Conversely, the highest wave heights detected by altimeters were recorded on February 2011 (Hanafin, et al., 2012), which makes this year suitable for performing the calibration of the model using a wide range of sea states. The main tuning tests with their relevant adjusted parameters are listed in ***Table 2***, including the terms used to correct underestimation of wind intensities >20 m/s in the ECMWF atmospheric products (Pineau-Guillou, et al., 2018). All other parameters values not included in ***Table 2***, are equal to those of T475. Wind intensities correction expression is detailed in Equation 14. There, $U_{10,corr}$ is the corrected wind intensity used to force the model, $U_{10,input}$ is the wind intensity as read from the wind fields, x_c is the correction factor and U_c the wind intensity threshold from which the correction starts working.

Table 2: Parameters adjusted per test.

Test Name	β_{max}	s_7	Re_c	s_1	U_c [m/s]	x_c
T475	1.75	4.32×10^5	1.15×10^5	0.66	21	1.05
Bm1.65-WC	1.65	4.32×10^5	1.15×10^5	0.66	20.5	1.04
Bm1.65-WC-s7-s4	1.65	3.60×10^5	0.90×10^5	0.66	20.5	1.04
TUD-165	1.65	3.60×10^5	0.90×10^5	0.68	20.5	1.04

Obs.: β_{max}, s_7, Re_c, s1, Uc, and xc correspond to input parameters BETAMAX, SWELLF7, SWELLF4, WCOR1 and WCOR2 in WW3.

Equation 14

$$\boldsymbol{U_{10,corr} = U_{10,input} + x_c max\,\{U_{10,input} - U_c, 0\}}$$

In Figure 2.a is possible to observe that, for the analysed area (North-East Atlantic), the use of T475 gives a large NMB, of about 5 %, in the neighbourhood of the most frequent H_s (2 m; see distribution in Figure 3). This over estimation increases for smaller H_s. There is also, in average, a non-negligible positive bias of 2.5 % for wave heights in the 2.5 to 6 m range. Reducing the overall overestimation for Hs<6 m is of vital importance, since this is main wave heights operation range for wave energy converters (WEC). This is first done by reducing the β_{max} parameter and slightly modifying the wind correction applied to the ERA5 wind forcing to prevent an excessive underestimation of Hs >7 m (see test Bm1.65-WC in Figure 2.a).

With Bm1.65-WC there is still a noticeable overestimation for $H_s \leq 2$ m. This is partially reduced in two steps. First by decreasing the *s7* parameter to 3.6×10^5 as proposed originally for the T471 parameterization (Rascle & Ardhuin, 2013). Then, the turbulent swell dissipation was enhanced by reducing the critical Reynolds Re_c (see Bm1.65-WC-s7-s4 in Figure 2.a). Note that these changes in the swell dissipation parameterization have also a beneficial effect in terms of minimizing the H_s distributions compared to the altimeter data (Figure 3). Finally it is noticed that with a slight intensification of the $S_{out,tur}$ term in Equation 7, increasing *s1* to 0.68, helps to further reduce an extra ~1.2 % the NMB for $H_s \leq 1.5$ m. This set of parameters values are defined as parameterization TUD-165.

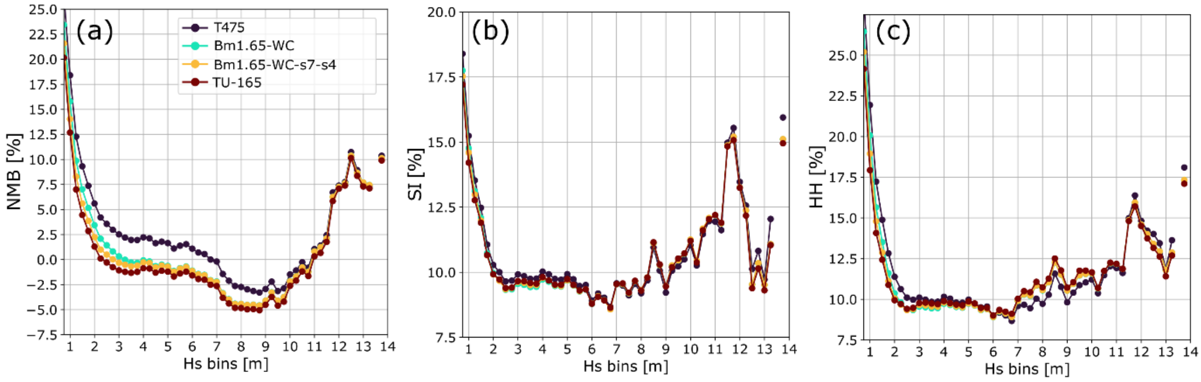

Figure 2: Model performance for parameterization adjustment tests (WW3 – Jason-2), year 2011. (a) Hs normalized mean bias (NMB), (b) scatter index (SI), and (c) Hanna Heinhold index (HH).

Obs.: H_s bins width is 0.25 m.

Compared to T475, using TUD-165 helps to reduce about 5 % the bias for wave heights <2 m in the North-East Atlantic. Additionally a small H_s NMB of about -1.2 % is obtained in the range of 2.5 to 6 m. Although there is an increase of the negative bias of about 2.5% in the range of 7.5 to 9 m, this is a great improvement in the model accuracy for most of the wave heights contained within the WECs operational range.

It is observed that throughout all the different parameterizations tests, no significative changes are introduce to the H_s SI values for the complete range of analysed wave heights (Figure 2.b). On the other hand, with TUD-175, there is a clear reduction of 2 to 2.5 % of the HH for wave heights < 2 m compared to T475 (Figure 2.c). As mentioned before, changes in the swell dissipation parameterization, have an effect in the shape of the H_s distribution. This is due to the modifications introduced to the transition from a laminar boundary layer above the group of smaller waves to a turbulent one on the group of larger waves. It is this combined effect that is key to account for the Raleigh distribution of waves. In Figure 3.a is possible to observe that, in general, all tests closely follow the distribution curve obtained with the Jason-2 altimeter. By making the occurrences differences (model-altimeter) it becomes more clear the main changes are introduced (Figure 3.b). Most noticeable effects of TUD-165 are found between H_s of 1 to 1.5 m, with a clear reduction of the underestimation of occurrences (e.g.; about 1 % at H_s=1.25 m).

This project has received funding from the Europeans Union's Horizon 2020 research & innovation programme under grant agreement number 101036457.

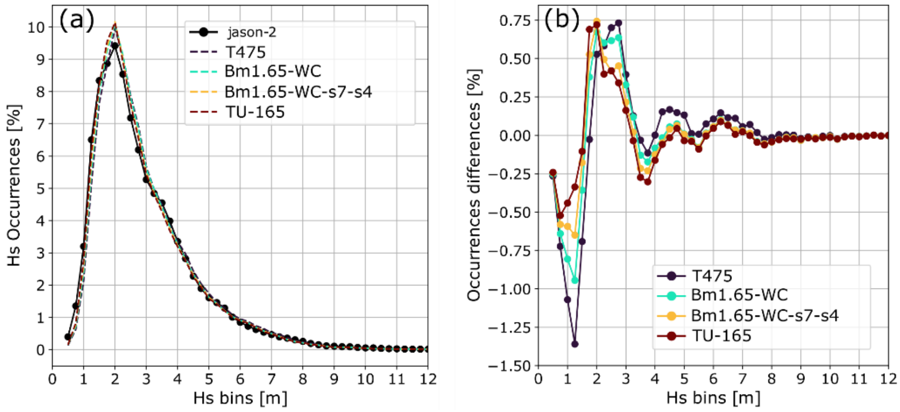

Figure 3: Significant wave heights normalized distributions for parameters' adjustment tests (year 2011).(a) Hs occurrences normalized by total amount of data (1,113,727). (b) Normalized occurrences differences (model – altimeter) with respect to Jason-2 CCI V3.

Obs.: H_s bins width is 0.25 m.

1.3.3 Adjustments verification with merged altimeter tracks and buoy data

The parameterizations' adjustments leading to TU-165 have been done analysing their effect on the simulated wave heights at "basin scales", comparing Jason-2 data with output from the N_ATL-15M grid. Here the analysis is extended to verify the model performance using TUD-165 within the European coastal shelf for the calibration year (2011). To that end, the integrated altimeter tracks from Jason-1, Jason-2, and Envisat (with available measurements for 2011) are used as reference to compare with H_s fields form the N_ATL-8M grid, which has higher resolution.

Using combined altimeter missions helps to increase the measurements density in the area, and to increase the number of repetitions in places crossed by several altimeter tracks. Using a higher resolution grid within the coastal shelf, helps to better capture changes in the wave field due to waves' interaction with the sea bottom and wave-tides interactions that become important in this area (Alday, Ardhuin, Dodet, & Accensi, 2022).

Considering the resolution from the model grid used here, altimeter measurements closer than 12 km from the coastline are not considered in the present analysis.

In this case, instead of looking at the wave heights' NMB and SI distribution as function of H_s, the performance parameters are analysed in terms of their spatial distribution (Figure 4). This provides additional information regarding mean accuracy levels within different areas of the model domain. In general, outside the coastal shelf, at depths >500 m, the wave heights bias is < 5 %. Higher values are found at the south of the Bay of Biscay where the H_s NMB can reach about 10 % (Figure 4.a). Within the coastal shelf The North sea, Ireland and Portugal stand out as zoned with low mean bias (≥5 %). Some areas with larger values (≥ 12 %) are found in the South of the Irish Sea, the south of the Bay of Biscay (close to the Spanish-French boarder). The largest bias values (> 15 %) are found between the Hebrides and Scotland, and the Danish straits. These areas also present the highest SI values (≥ 16 %; Figure 4.b). For these particular locations, the combined high NMB and SI are thought to related to the high noise to signal ratio in the measurements taken close to land. The "noise" in the altimeter measurement corresponds to the

This project has received funding from the Europeans Union's Horizon 2020 research & innovation programme under grant agreement number 101036457.

detection of the non-Gaussian land surface that alters the retrieval of the waves' geophysical signal in the radar footprint. As a result, this leads to errors in the estimation of the significant wave heights.

In general, outside the afore mentioned areas, the H_s SI ranges between 10 to 12 % which aligns with previous studied in the area using altimeter data by Alday et al. (2022).

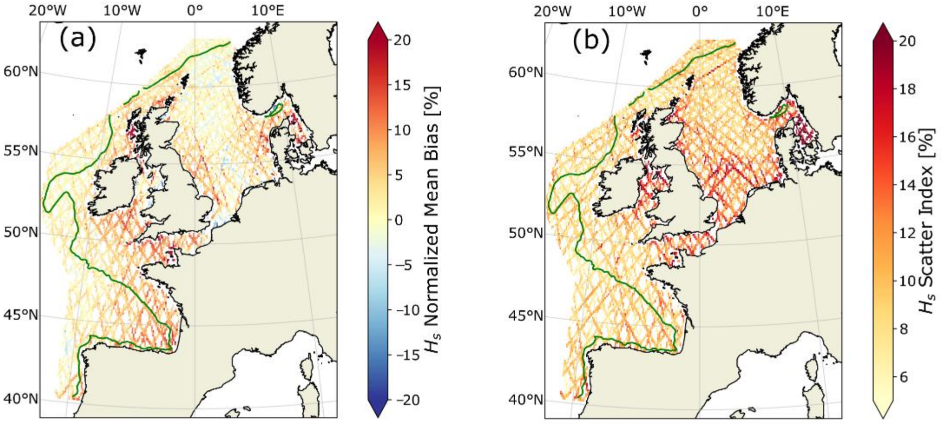

Figure 4: Performance parameters for calibration year (2011) using TUD-165 compared with integrated tracks from Jason-1, Jason-2 and Envisat. (a) H_s Normalized mean bias (NMB) and (b) H_s scatter index (SI).

Obs.: Green lines indicate the 500 m depth contour.

Figure 4 gives a good idea of the model performance obtained with TUD-165 within the coastal shelf. Nevertheless, it is still necessary to verify the model performance with in situ measurements from buoys which provide records of a wider range of sea states at specific locations. Using buoy data also allows to use other parameters that characterize the sea state, like the wave peak period, mean periods and mean wave direction.

A selection of 34 buoys located within the coastal shelf, covering a wide variety of depths, utilised in order to verify the model accuracy in the simulations of H_s, the peak period T_p, the T_{02} mean period, and the mean wave direction D_m. Results for the NMB, BIAS, SI and the Pearson correlation index (CORR) are presented in Figure 5. All wave parameters from buoy measurements were obtained from the CMEMS In Situ Thematic Assembly Center (TAC). Details of the buoys locations and depths are presented in Table 3 at the end of this section.

First thing observed in Figure 5, is that wave heights' NMB in the South of the Bay of Biscay is, smaller than previously estimated with altimeter data, ranging from -4.2 to 6.5 % along the Spanish North coast (Figure 5.a). This is equivalent to a bias of -0.2 to 0.2 m. Along Portuguese waters the H_s NMB is ≤1.7 % except at the location of buoy 6200199 with NMB = 9.9 % (equivalent to 0.2 m). Note that, in general, for the rest of the domain the wave heights' NMB is typically <5 %. Largest NMB are found at the location of the 2 buoys in the English Channel 6200103 and 6200027, with values of 35 % and 19.5 % respectively, equivalent to 0.46 and 0.26 m. The highest Hs SI values are also found at these locations (19.3 % at 6200103 and 16.6 % at 6200027). It is thought that this combined high biases and SI are related to inadequate resolution of the tidal and wind forcing within the English Channel,

This project has received funding from the Europeans Union's Horizon 2020 research & innovation programme under grant agreement number 101036457.

leading to an overestimation of the effective wind. In this area the wave conditions are dominated by the local wind, thus the effect of boundary conditions (or waves incoming from the North Atlantic) is negligible (Alday, Ardhuin, Dodet, & Accensi, 2022).

Overall, the spatial distribution of the H_s scatter index obtained with buoys, follows the distribution obtained previously with altimeter data (Figure 4.b). Although, results at the location of buoy L91, close to the Dutch coast, show a SI considerably lower (12.8 %) compared to the previously estimated value with merged altimeter tracks (~18 %). Wave heights' correlation between model and buoy are typically > 0.95, with the exception of the Donostia-buoy, which is 0.92. This results points to a close agreement between the simulation of wave heights evolution and the recorded H_s time series.

The model performance in terms of peak periods (T_p) are presented in Figure 5.b. This parameter commonly presents high temporal variability from measurements, which is mainly related to its dependence on the local wind conditions (which is highly dynamic).The measuring instrument characteristics (namely accuracy and sampling rate) should also be taken into account as a source of potential differences in the estimation of T_p between instruments. Thus, it is not rare to find larger SI or biases when comparing with spectral model results, mainly because such temporal variability is not properly captured. This is mainly related to the wind forcing characteristics, and the wave nonlinear interactions discretization (e.g., DIA). Frequencies discretization of the spectrum in the model can also affect where the peak period is estimated. To partially reduce the high temporal variability of T_p from buoy measurements, a moving average with a 2-hours window was applied.

About half of the 34 buoys recorded T_p data. It is observed that the highest peak period NMB values are obtained when comparing with buoys from Puertos del Estado (6200024, 6200025, 6200083, and 6200084). At these locations, the model-buoy comparisons point to a T_p NMB of about 14 % (equivalent to 1.2 s). For the rest of the analysed locations the NMB ranges between -1.2 % to 2 % in average.

This project has received funding from the Europeans Union's Horizon 2020 research & innovation programme under grant agreement number 101036457.

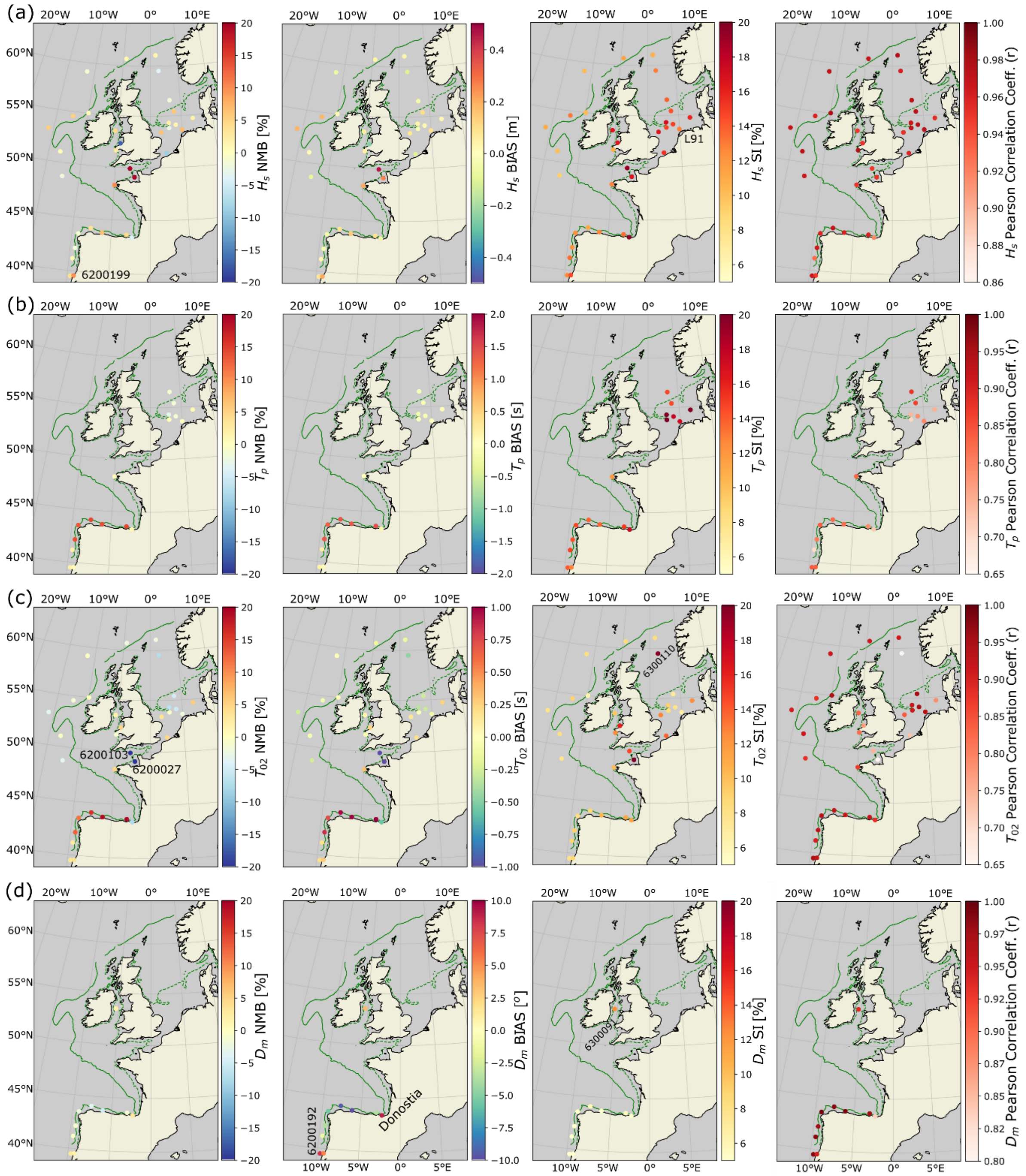

Figure 5: Model performance indicators obtained comparing with buoy data for (a) H_s, (b) T_p, (c) T_{02} and (d) D_m. Results for calibration year 2011 using TUD-165.

Obs.: Green lines indicate the 500 m depth contour, dashed green lines indicate the 50 m depth contour. Depth data obtained from the N_ATL-8M model grid.

For the SI of the peak periods, the highest values are observed in The North Sea, at the location of buoys D151 (20 %), J61 (21.9 %), and NsbIII (24.7 %). These locations also show the lowest CORR values, ranging from 0.7 to 0.75. This high SI and lower correlations are mainly caused by differences in the estimation of the peak period during calm sea states (characterized by small H_s). Examples of this effect is presented in Figure 6.a,b between May 30 and June 4 2011. While the overall energy contained in the spectrum is well simulated, observed as a high agreement in model-buoy H_s (Figure 6a), large jumps of the modelled T_p are observed (Figure 6.a,

This project has received funding from the Europeans Union's Horizon 2020 research & innovation programme under grant agreement number 101036457.

mid panel). These “events” are more frequent when there is a reduction of the H_s (from an already low energy sea state), which is logically related to a drop in the local wind intensities.

It is possible that, under very low wind intensities, the model underestimates the energy input to the spectrum, which leads to a slower growth of the wind sea component. As a result, the peak of energy is identified in the swell component carrying more energy (probably just slightly more), which is why the simulated peak periods are closer to 8 s than the 4 s identified in the buoy. This effect can be observed in Figure 6.b (highlighted events in orange rectangles), and the overall effect on the T_p “scattered” is shown in Figure 6.d.

It is also possible that the wind input form ERA is too mild, and that is the cause of the underestimation of the local wind sea. In the absence of spectral data form the buoy, it is not possible to fully assess the source of these differences. On the other hand, there good correlation, lower SI, and almost negligible bias of the T_{02} mean period (especially in the range of the most frequent occurrences). This is another proper example of how the overall energy levels in the spectrum are well simulated (Figure 6.c).

More details on the model performance in terms of the T_{02} mean period are presented in Figure 5.c. Overall the NMB levels are well constrained (as for H_s), ranging from -3.5 % to 5.5 %. Nevertheless, two main exceptions are found. First, at the location of buoys 6200024, 6200025, 6200083, and 6200084 (off the North coast of Spain), where the T_{02} NMB ranges between 11 to 18 %, equivalent to 0.7 to 1.2 s. And Second, at the English Channel when comparing with buoys 6200103 and 6200027 where the largest NMB values are found, -26 % and -35 % respectively. These latter values might be misleading since the comparison with the buoy data was done using the mean zero-crossing period (T_z) and not the T_{02} obtained from the integration of spectral data. Thus, Its suitability can be questioned. Nevertheless, the comparison was still considered as a reference.

The T_{02} scatter index spatial distribution is similar to that of the H_s, with even lower values ranging from 7 to 12 %. One exception is found at the location of buoy 6300110 (19.7 %) in the North Sea. Once again the comparison was done with T_z. Note how the SI obtained by comparing with buoy 6300112 immediately to the North is only 8.25 %. Most likely, the 19.7 % is related to problems in the periods data from buoy 6300110 and should be considered an outlier.

Outside results compared with 6300110, correlation values obtained for T_{02} are typically >0.85, with values > 0.9 along the Bay of Biscay, Portuguese and Irish waters, and in most analysed locations in the North Sea (Figure 5.c, right panel).

Finally, on Figure 5.d, is possible to observed that only 10 of the 34 buoys used for comparison provide time series of the wave mean direction (D_m), most of them located along the Portuguese and Spanish waters (Bay of Biscay). NMB are <5 % at all locations. In absolute terms, the bias can range from about -9.5° at 6200192 and 6200082 to ~8.9° at Donostia-buoy (of the order of the model directional discretization). The mean direction scatter index is < 6 % in all locations except when comparing with buoy 6200091 (in the Irish Sea), where it reaches 12.4 %. As

This project has received funding from the Europeans Union’s Horizon 2020 research & innovation programme under grant agreement number 101036457.

for the other 2 parameters obtained from spectral integration, correlation values for D_m are typically high ≥ 0.94, with the exception of Donostia-buoy with CORR=0.84.

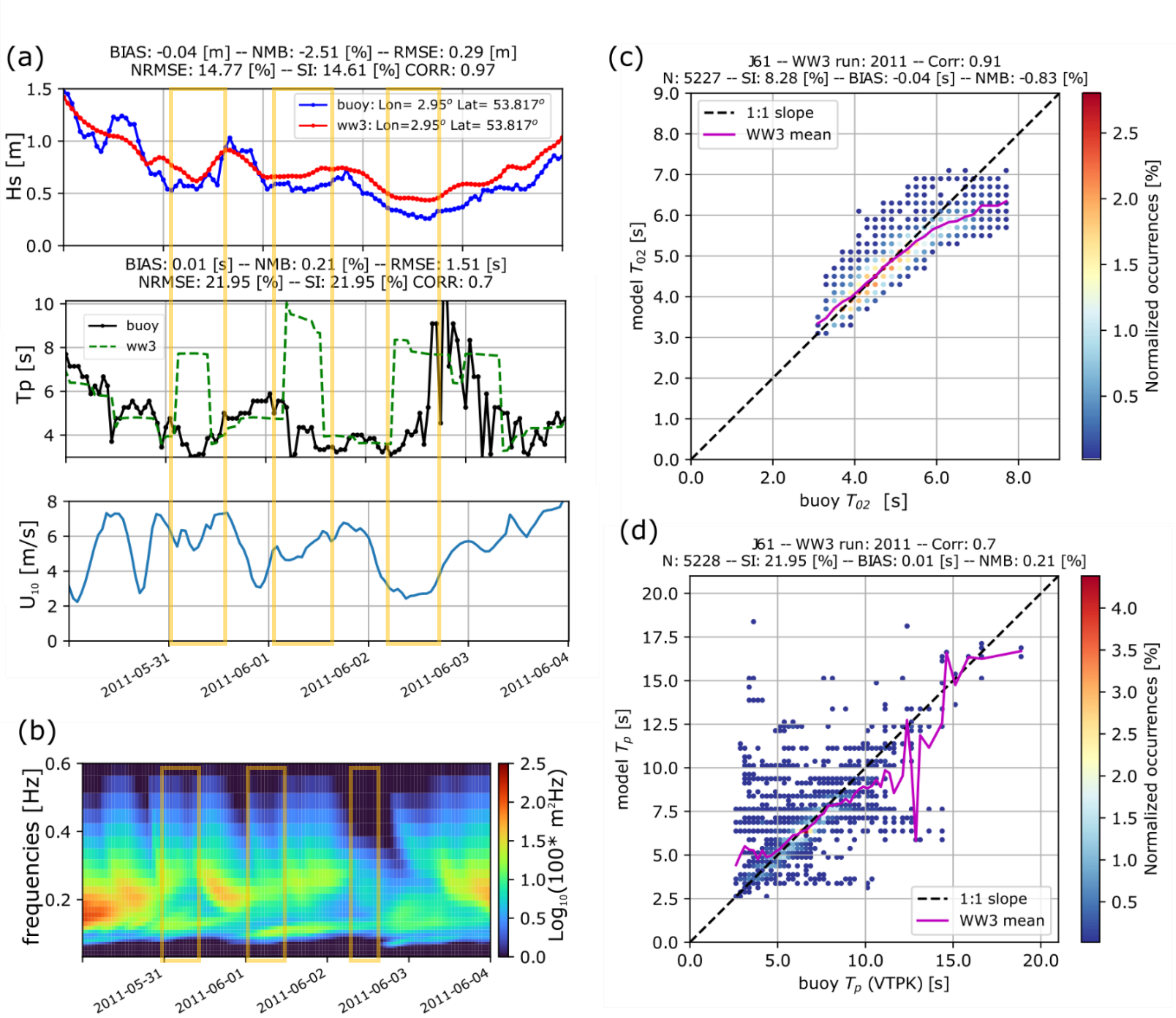

Figure 6: Model-buoy performance details at buoy J61. (a) Time series of recorded and modelled Hs. and Tp on top and mid panels, and wind intensity as read in WW3 on bottom panel. (b) Time series of the modelled wave spectra at J61. Scatter plot and performance parameters of T02 and Tp in (c) and (d) respectively.

Obs.: Time series of peak periods in (a) is as given by the buoy records. Orange rectangles highlight time windows where differences in the estimation of the T_p are found during low energy sea states. In (c) and (d), N is the total amount of analysed data.

Table 3: Selected buoys for validation.

Buoy ID	Longitude [°]	Latitude [°]	Depth [m]	Data type
6200024	3.040	43.64	887.42	Wave parameters
6200025	−6.167	43.733	597.88	Wave parameters
6200027	−2.218	49.082	27.21	Wave parameters
6200029	−12.401	48.701	2046.10	Wave parameters
6200066	−1.614	43.53	53.50	Spectral
6200069	−4.968	48.29	58.39	Spectral/Wave param.
6200081	−13.301	51	2010.18	Wave parameters
6200082	−7.618	44.064	1149.46	Wave parameters
6200083	−9.21	43.49	378.53	Wave parameters
6200084	−9.374	42.121	488.27	Wave parameters
6200091	−5.431	53.484	87.45	Wave parameters
6200093	−9.999	55.002	121.15	Wave parameters

6200095	−15.862	53.017	3246.79	Wave parameters
6200103	−2.900	49.9	65.05	Wave parameters
6200105	−12.367	54.55	2944.47	Wave parameters
6200144	1.700	53.4	24.74	Wave parameters
6200191	−9.580	41.15	2326.12	Wave parameters
6200192	−9.640	39.51	1114.15	Wave parameters
6200199	−9.210	39.56	118.50	Wave parameters
6200301	−4.50	52.3	22.74	Wave parameters
6200303	−5.100	51.603	35.22	Wave parameters
6300110	1.500	59.5	109.75	Wave parameters
6300112	1.000	61.1	152.74	Wave parameters
6400045	−11.401	59.1	1856.19	Wave parameters
6400046	−4.500	60.701	1107.67	Wave parameters
A121	3.817	55.417	30.46	Wave parameters
D151	2.933	54.317	40.78	Wave parameters
Donostia-buoy	−2.026	43.569	87.20	Wave parameters
Ekofisk	3.224	56.543	69.38	Wave parameters
F161	4.017	54.117	46.83	Wave parameters
J61	2.950	53.817	39.73	Wave parameters
L91	4.961	53.614	23.733	Wave parameters
NsbIII	6.783	54.683	38.15	Wave parameters
Westhinder	2.436	51.381	26.34	Wave parameters

1.4 Wave dataset validation

In the present section, validation of the generated hindcast is presented. As previously done for the parameterizations' adjustments, the validation of the model is done using first altimeter data, and then with in situ buoy measurements. This approach helps to take advantage of the large spatial and temporal wave heights' coverage provided by altimeters, plus the possibility to evaluate the model's results in terms of other parameters outside H_s.

1.4.1 Validation with altimeter data

Validation of the model output using altimeter data to compare, is done in 2 steps. First, to provide an idea of the interannual range of variability of wave heights' NMB, SI and HH index, these performance parameters are computed for each year available in the CCI V3 dataset for the Jason-2 altimeter, from 2008 to 2019. Then, to have a more generalized accuracy level of the H_s simulations, considering longer time windows, the performance parameters are computed using 5 altimeter missions, integrating all available years: Envisat (2002 to 2012), Jason-1 (2002 to 2012), Jason-2 (2008 to 2019), Jason-3 (2016 to 2020), and Saral (2013 to 2018). With this approach the full time window provided by the CCI V3 dataset is utilized.

All comparisons with altimeter data in this section are done using H_s fields from the N_ATL-8M grid. As done in section 1.3.3, altimeter measurements closer than 12 km from the coastline are not considered in the present analysis.

The H_s performance values for years 2008 to 2019 are presented in Figure 7, which provides a good idea of the accuracy changes range at each H_s level. Close to the most frequent wave heights (2 m) the NMB is in average 3 % with a variation range < 2%. This range increases for larger wave heights, and can be of about 4 % between H_s of 2.75 to 6.5 m. Note that the NMB values per year in this wave heights range basically "oscillates" around 0 %. In some cases the bias variability range can reach up to 9 % for H_s > 7 m (Figure 7.a). Inter-annual variability range of the H_s SI is ≤ 1.2 % for the most frequent wave heights, it then increases up to 2.5 % for wave heights between 2.75 to 6.5 m, and can reach values of ~8 % for H_s = 9.75 m (Figure 7.b). Note that the HH index presents a similar behaviour (Figure 7.c).

The largest inter-annual variability ranges, when comparing with altimeter data, are observed for H_s > 7 m. It is thought that this could be partly due to the “simple” wind intensities correction applied to the ERA5 forcing, used to mitigate the underestimation of larger wave heights. A slight increase of the H_s SI was already observed at global scales in Alday et al. (2021) for different wind intensities correction tests. A complementary explanation is related to the changing accuracy of the wind fields in time, which can be linked to the amount of assimilated data in the ECMWF atmospheric model (from 0.75 million per day in 1979 to 24 million in 2018).

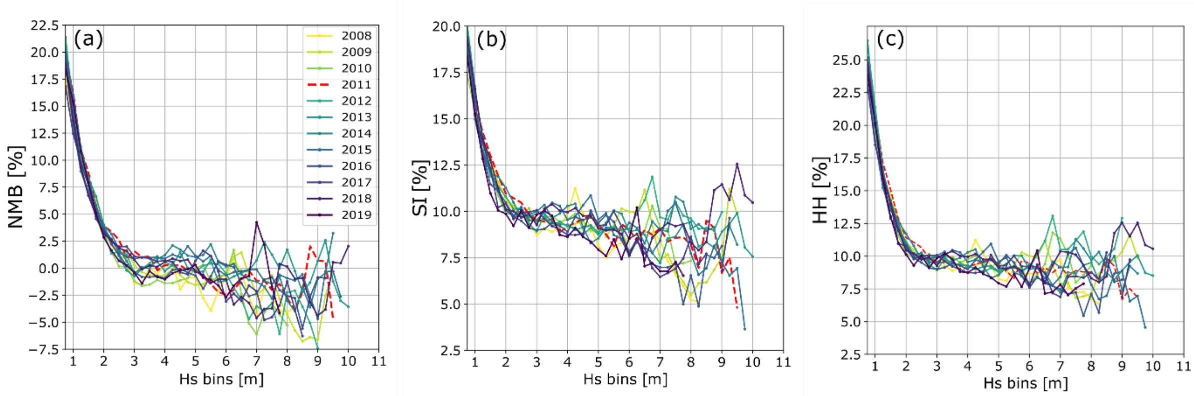

Figure 7: Inter-annual variability of performance indicators for wave heights using Jason-2. (a) Normalized mean bias (NMB), (b) scatter index (SI), (c) Hanna Heinhold index (HH).

Obs.: Calibration year 2011 in dashed red line. H_s bin size is 0.25 m.

Paying particular attention to the calibration year 2011, some differences can be found between the results shown previously in Figure 2 (red line) and the one from Figure 7. For example, there is a slight “shift” of the NMB to positive values (about 1.5 %) for $H_s \leq 3$ m, and a general reduction of the underestimation of H_s > 7 m (when comparing 2011 from Figure 7.a to the red line in Figure 2.a). This is mainly related to the use of a higher resolution grid (N_ATL-8M), which helps to better capture the wave field evolution within the coastal shelf. Additionally, and related to the use of a higher resolution grid, the inter-annual accuracy analysis considers altimeter measurements closer to the coast, down to 12 km offshore.

Validation of the hindcast using the complete mission duration for Envisat, Jason-1, Jason-2, Jason-3, and Saral, is presented in Figure 8. It is expected that different instruments will have their own measuring accuracy, and their use provide further insights on the expected accuracy ranges of the simulations. It should be noticed that the CCI V3 dataset provides measurements from Saral until year 2021, but in the present analysis only data until 2018 was used, 2 years into the altimeter’s drifting phase (Dibarboure, Lamy, Pujol, & Jettou, 2018). This is done to ensure the quality of the data used from the Saral altimeter (Krishna, Vikram, & Sreejith, 2023).

This project has received funding from the Europeans Union’s Horizon 2020 research & innovation programme under grant agreement number 101036457.

In Figure 8.a, it is observed that the NMB for wave heights between 1.25 to 6 m, is very similar when computed with all selected altimeters, with a differences range ≤ 2 %. A NMB differences range ≤ 2 % is observed for wave heights between 1.25 to 6 m, which means that with al altimeters the results are very close (Figure 8.a). This difference range is similar up to H_s of 9.5 m except for Jason-3.

Comparisons with Jason-3 point to a slight H_s overestimation from the simulations (from 1.5 to 3 %). More different results per altimeter are observed for wave heights > 10 m. Specially from comparisons with Jason-1, which gives the largest overestimation (NMB = 14 %) at H_s = 11.25 m. Jason-2 and Envisat, in terms of NMB levels, show a more comparable behaviour for large wave heights, with a differences range < 3.5 %. These results show that the reduction of the larger wave heights underestimation is accomplished with the wind intensities correction used in TUD-165. Regardless of some high NMB values observed for the tuning year at basin scale (Figure 2.a), the overestimation of Hs>10 m within the coastal shelf is typically ≤ 6 % when the analysis is done over longer time windows.

Similar values are observed for the SI and HH index (Figure 8.b,c). As for the NMB, there is a clear difference between the results obtained with Jason-1 and the rest of the altimeters for H_s > 10 m. This is thought to be related to inaccuracies of Jason-1 when it comes to the detection of large wave heights (Durrant, Greenslade, & Simmonds, 2009).

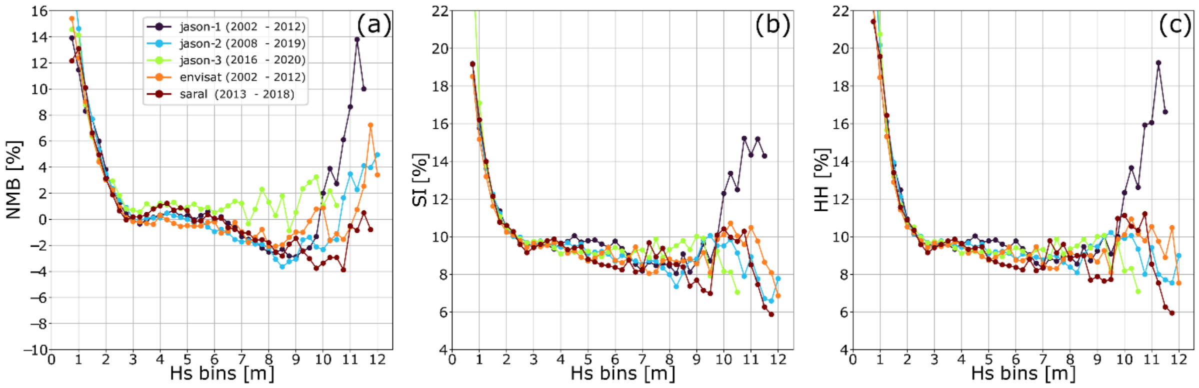

Figure 8: Hindcast validation obtained with different altimeters' (full) mission time windows. (a) H_s normalized mean bias (NMB), (b) scatter index (SI) and (c) Hanna Heinhold index (HH).

Obs.: H_s bin size is 0.25 m. Statistical parameters are computed using at least 50 occurrences per H_s bin.

Overall, for time windows larger than 4 years, considering Jason-2, Jason-3, Envisat and Saral, the SI and HH is ≤ 10 % for wave heights in the range of 2 to 12 m range.

1.4.2 Validation with buoy data

Validation with altimeter data allows to cover a large portion of the modelled domain, but it only gives a good idea of the model performance in terms of H_s. Other wave parameters characterizing the sea states can be analysed with buoy data. On the downside, given the vast amount of data generated for a 30 years hindcast, it becomes necessary to select specific locations to perform a more complete validation. First, from Figure 10 to Figure 12, 4 different years have been selected (2005, 2010, 2015 and 2020) including the results from all buoys listed in Table 3 (similar to Figure 5). Then, in Table 4 and Table 5, a summary of the model performance is presented for 11 years (2010 to 2020) at 6 locations representative of areas of interest in the context of the present project: 6200014, 6200093, 6200191, 6400046.

In general the model performance for H_s, T_p, T_{02} and D_m do not differ much from the results already analysed for the tuning year 2011 (see Figure 5). The higher biases for peak and mean periods are apparently persistent over time on the North of Spain (Donostia buoy and 6200024). Detailed results can be seen in Table 4 for location 6200024. Low NMB levels for the significant wave height and mean directions oscillate between -5 to 5 %. Larger H_s bias levels might be found within the English Channel (e.g.; Figure 11.a) but this is not a trend. The overall poorer values of performance parameters for periods at L91 (close to the Dutch coast) for years 2013 and 2014 are due to an odd behaviour from the buoy (Table 5). This was verified in the time series from the buoy source file, where excessively large periods were observed, unrealistic for this area (e.g.; T_p > 20 s). High correlation values for H_s (>0.95) and the mean period T_{02} (typically > 0.9) are satisfactory achieved for all analysed locations, with random errors (SI) in the range of 10 to 14%. The larger SI values are normally found in areas with reduced depth. It should be noted that larger SI values do not necessarily imply a poorer performance of the model.

From the buoy selection presented in Table 4 and Table 5, particularly good results for H_s and T_{02} (in all performance parameters) are found at 6200191 (Portugal), 6200093 (Ireland) and J61 (North sea). The lowest NMB and SI are found at these locations.

This project has received funding from the Europeans Union’s Horizon 2020 research & innovation programme under grant agreement number 101036457.

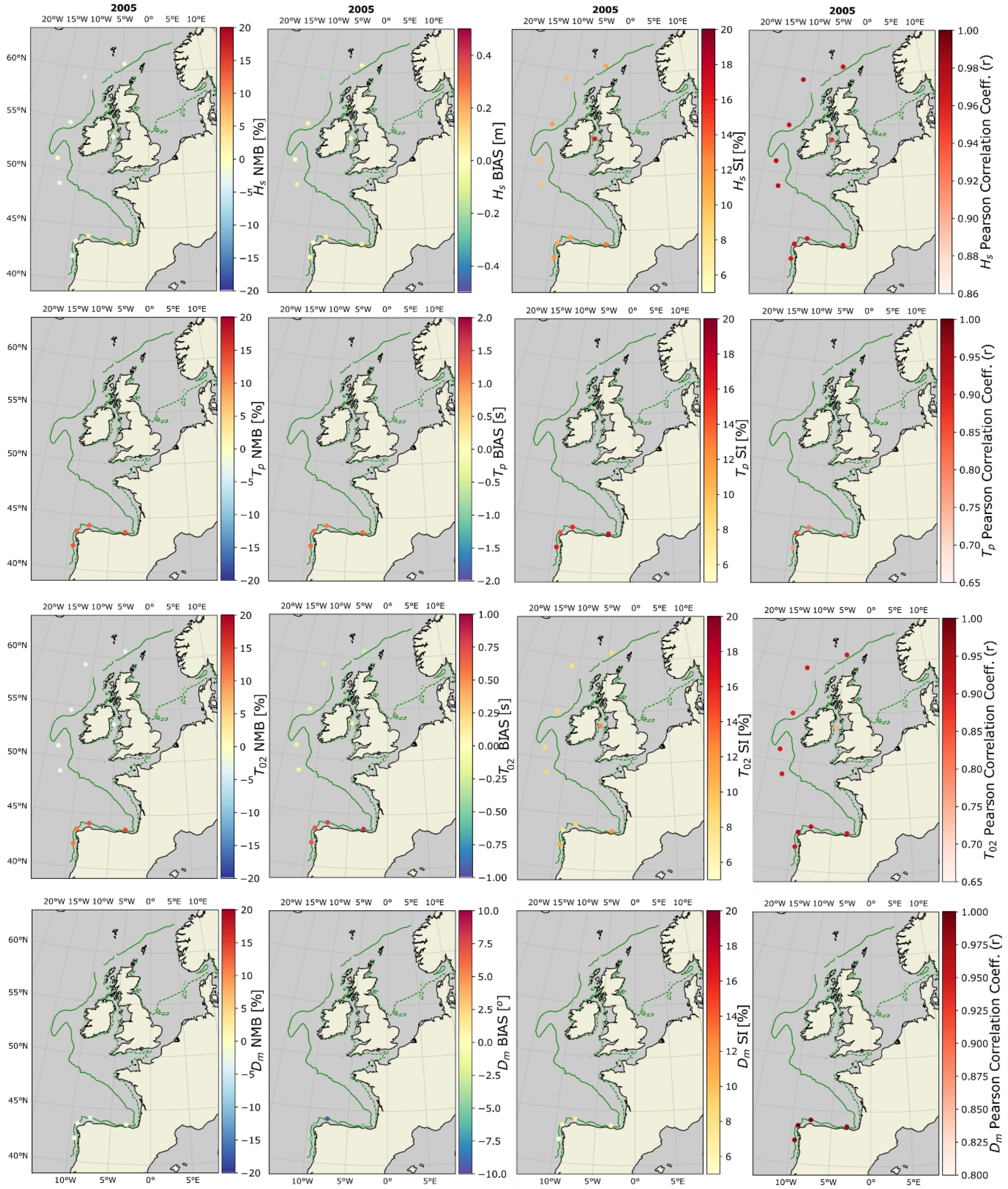

Figure 9: Model performance indicators obtained comparing with buoy data for (a) H_s, (b) T_p, (c) T_{02} and (d) D_m. Results for validation year 2005 using TUD-165.

Obs.: Green lines indicate the 500 m depth contour, dashed green lines indicate the 50 m depth contour. Depth data obtained from the N_ATL-8M model grid

This project has received funding from the Europeans Union's Horizon 2020 research & innovation programme under grant agreement number 101036457.

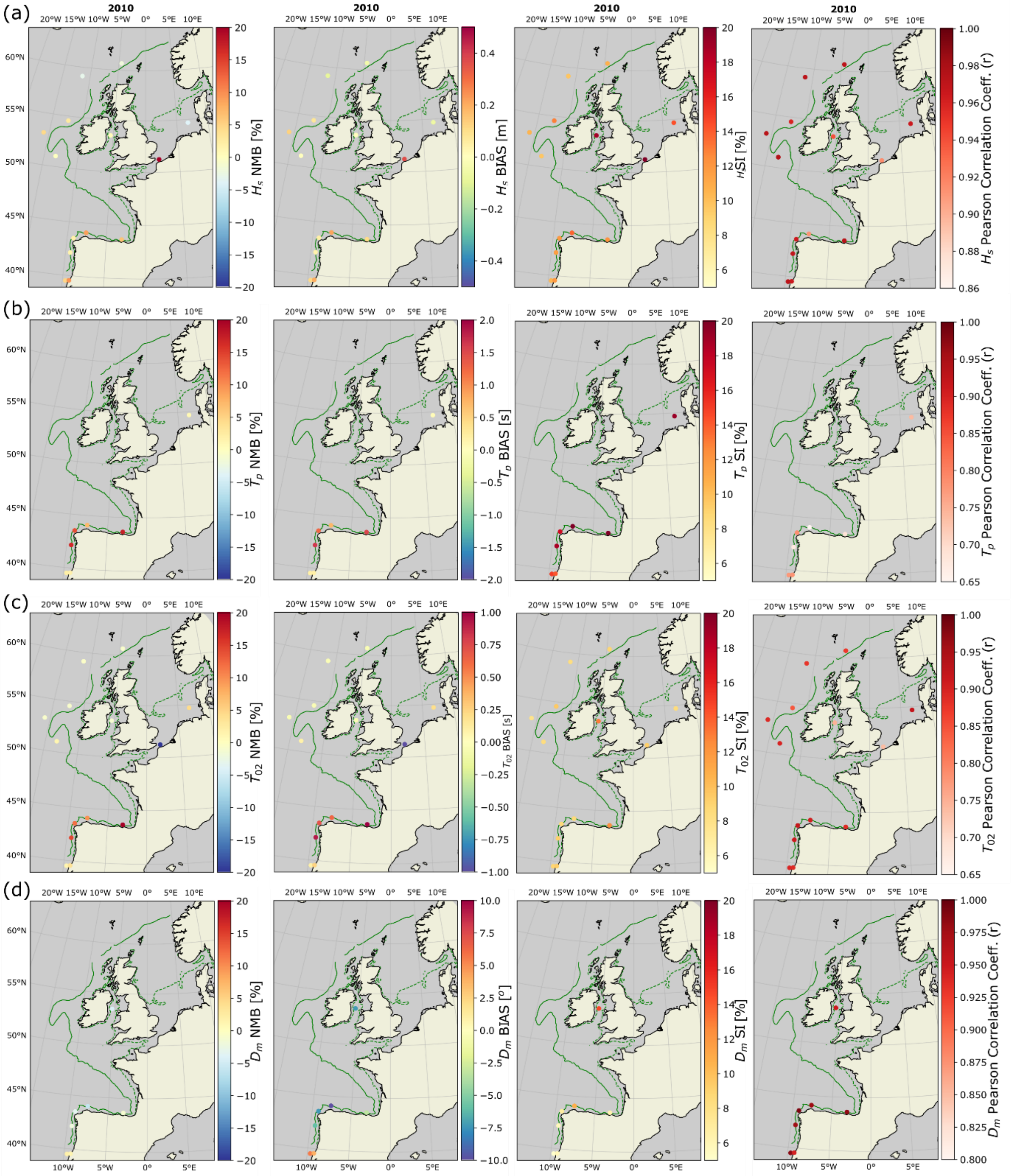

Figure 10: Model performance indicators obtained comparing with buoy data for (a) H_s, (b) T_p, (c) T_{02} and (d) D_m. Results for validation year 2010 using TUD-165.

Obs.: Green lines indicate the 500 m depth contour, dashed green lines indicate the 50 m depth contour. Depth data obtained from the N_ATL-8M model grid.

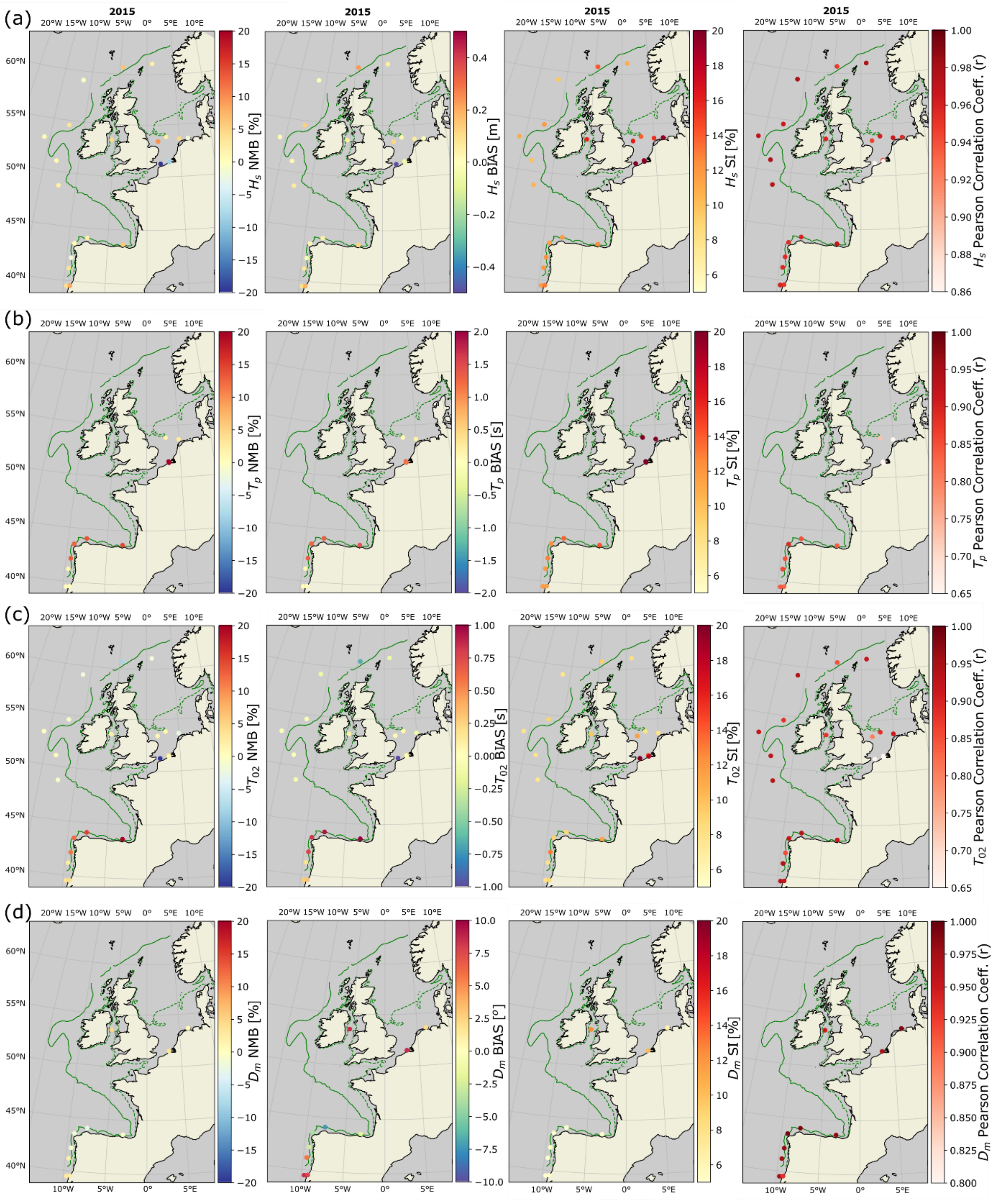

Figure 11: Model performance indicators obtained comparing with buoy data for (a) H_s, (b) T_p, (c) T_{02} and (d) D_m. Results for validation year 2015 using TUD-165.

Obs.: Green lines indicate the 500 m depth contour, dashed green lines indicate the 50 m depth contour. Depth data obtained from the N_ATL-8M model grid.

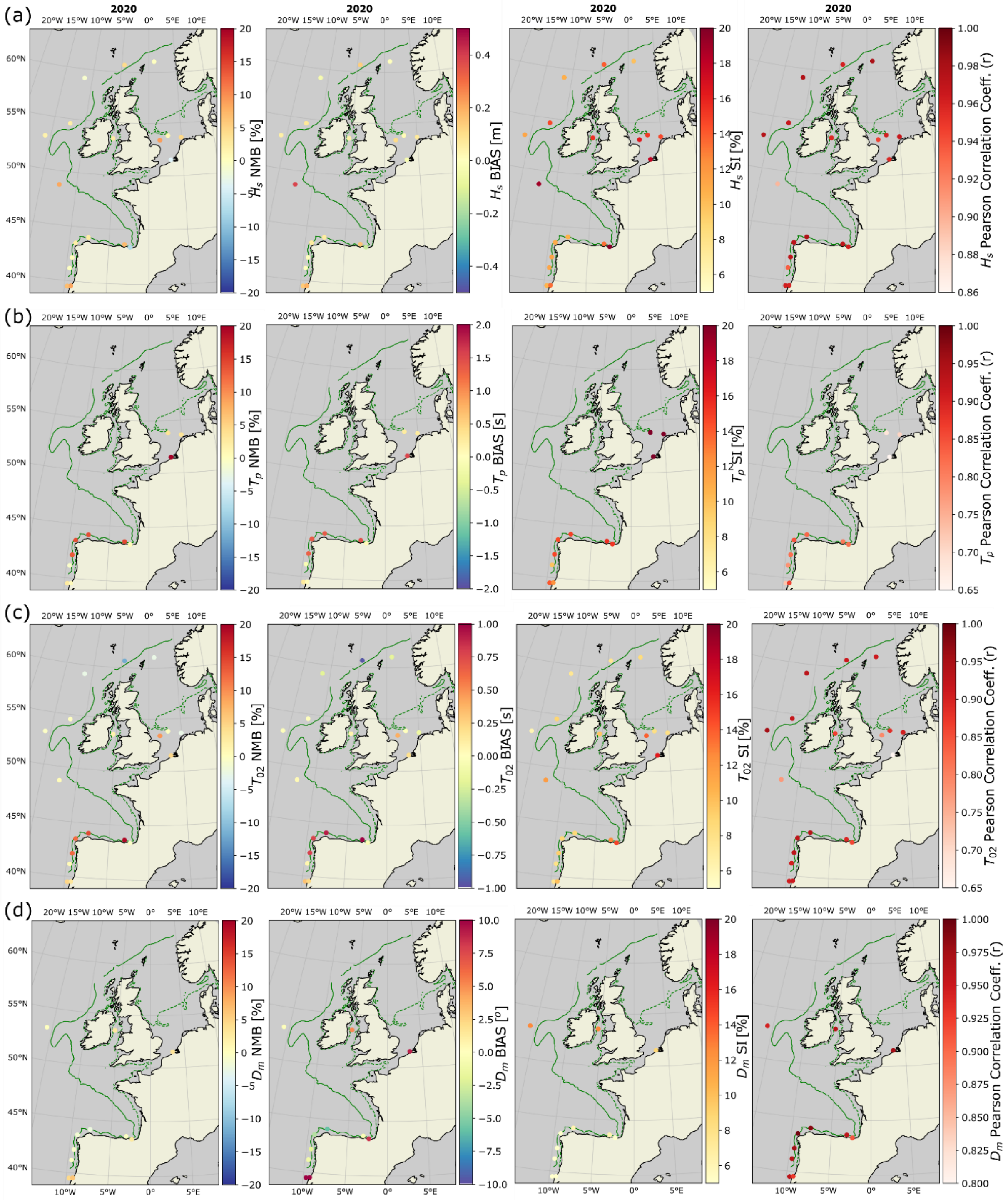

Figure 12: Model performance indicators obtained comparing with buoy data for (a) H_s, (b) T_p, (c) T_{02} and (d) D_m. Results for validation year 2020 using TUD-165.

Obs.: Green lines indicate the 500 m depth contour, dashed green lines indicate the 50 m depth contour. Depth data obtained from the N_ATL-8M model grid.

Table 4: Hindcast performance parameters for years 2010 to 2020. WW3-buoy comparison at locations: 6200024, 6200093, 6200191.

Buoy ID	year	Hs				Tp				T02			
		NMB [%]	BIAS [m]	SI [%]	CORR	NMB [%]	BIAS [s]	SI [%]	CORR	NMB [%]	BIAS [s]	SI [%]	CORR
6200024	2010	6.39	0.11	12.22	0.97	17.31	1.52	21.94	0.69	20.69	1.13	12.38	0.89
	2011	4.25	0.08	13.45	0.96	14.53	1.46	15.07	0.79	19.47	1.22	11.27	0.92
	2012	10.94	0.2	12.48	0.97	14.97	1.4	14.88	0.81	20.31	1.2	11.89	0.9
	2013	1.84	0.04	12.41	0.97	13.02	1.27	15.73	0.81	17.17	1.05	11.17	0.92
	2014	2.91	0.06	13.15	0.97	11.76	1.17	14.62	0.86	18.38	1.15	12.66	0.91
	2015	5.83	0.12	12.63	0.97	14.52	1.42	14.2	0.84	19.66	1.23	11.42	0.92
	2016	6.47	0.13	12.85	0.97	13.67	1.34	15.54	0.81	20.21	1.25	12.36	0.92
	2017	6.37	0.11	12.55	0.97	12.56	1.21	17.23	0.76	19.94	1.17	12.72	0.89
	2018	4.72	0.1	14.13	0.96	10.69	1.1	16.68	0.79	17.81	1.12	12.72	0.89
	2019	4.8	0.09	12.24	0.97	14.19	1.33	14.9	0.82	19.03	1.14	11.18	0.92
	2020	7.07	0.15	13.4	0.97	14.45	1.43	15.5	0.81	19.06	1.21	12.5	0.9
6200093	2010	2.75	0.07	10.58	0.96	----	----	----	----	3.85	0.26	8.88	0.87
	2011	0.64	0.02	10.25	0.98	----	----	----	----	0.25	0.02	6.32	0.95
	2012	-0.22	-0.01	10.35	0.96	----	----	----	----	0.5	0.04	6.27	0.92
	2013	1.18	0.03	11.64	0.98	----	----	----	----	0.13	0.01	7.06	0.95
	2014	0.38	0.01	11.36	0.98	----	----	----	----	0.32	0.02	7.06	0.95
	2015	-1.1	-0.05	9.95	0.97	----	----	----	----	-0.83	-0.07	6.13	0.92
	2016	-1.73	-0.06	10.74	0.97	----	----	----	----	0.56	0.04	6.66	0.93
	2017	-0.61	-0.02	10.27	0.97	----	----	----	----	1.51	0.12	6.06	0.93
	2018	4.75	0.12	11.55	0.96	----	----	----	----	2.79	0.18	6.7	0.92
	2019	2.22	0.06	10.62	0.98	----	----	----	----	1.14	0.08	6.75	0.94
	2020	2.33	0.08	10.58	0.98	----	----	----	----	1.94	0.14	7.22	0.94
6200191	2010	----	----	----	----	----	----	----	----	----	----	----	----
	2011	0.84	0.02	13.42	0.93	1.79	0.21	14.76	0.7	2.59	0.19	8.83	0.90
	2012	4.15	0.09	10.47	0.97	1.91	0.19	12.7	0.85	2.79	0.18	7.05	0.94
	2013	6.43	0.14	11.99	0.96	2.41	0.23	11.97	0.87	2.68	0.17	6.58	0.94
	2014	7.7	0.15	11.8	0.97	3.27	0.3	15.81	0.8	3.36	0.2	7.16	0.94
	2015	3.33	0.08	11.92	0.96	0.79	0.09	11.95	0.86	2.46	0.17	7.77	0.94
	2016	4.59	0.11	11.1	0.97	1.7	0.18	12.32	0.86	2.87	0.2	8.23	0.94
	2017	4.6	0.1	12.19	0.97	1.39	0.16	12.87	0.83	4.2	0.3	9.06	0.92
	2018	4.7	0.11	11.3	0.97	3.38	0.37	14.3	0.82	3.92	0.27	8.19	0.94
	2019	5.02	0.13	12.94	0.96	1.78	0.2	13.37	0.84	3.11	0.22	8.6	0.93
	2020	-0.18	-0.01	11.32	0.93	-0.77	-0.1	9.85	0.78	0.68	0.06	7.92	0.90

Obs: Color scales consider maximum and minimum values from results including Table 4 and Table 5.

Table 5: Hindcast performance parameters for years 2010 to 2020. WW3-buoy comparison at locations: 6400046, J61, L91.

Buoy ID	year	Hs				Tp				T02			
		NMB [%]	BIAS [m]	SI [%]	CORR	NMB [%]	BIAS [s]	SI [%]	CORR	NMB [%]	BIAS [s]	SI [%]	CORR
6400046	2010	-1.96	-0.05	10.72	0.97	----	----	----	----	-0.92	-0.06	8.82	0.87
	2011	1.07	0.04	11.36	0.97	----	----	----	----	-2.11	-0.15	8.36	0.91
	2012	----	----	----	----	----	----	----	----	----	----	----	----
	2013	4.8	0.13	13.53	0.96	----	----	----	----	3	0.19	8.98	0.91
	2014	6.83	0.17	13.65	0.97	----	----	----	----	1.5	0.1	8.9	0.92
	2015	6.25	0.23	14.12	0.95	----	----	----	----	-8.22	-0.68	9.25	0.85
	2016	6.59	0.19	14.15	0.96	----	----	----	----	-12.81	-1.02	7.56	0.91
	2017	4.46	0.14	30.32	0.79	----	----	----	----	-12.65	-1	7.02	0.9
	2018	4.62	0.14	13.36	0.95	----	----	----	----	-12.38	-1.01	7.74	0.88
	2019	4.77	0.14	13.86	0.95	----	----	----	----	-12.22	-0.97	7.77	0.9
	2020	4.23	0.13	14	0.96	----	----	----	----	-11.96	-0.97	7.6	0.91
J61	2010	----	----	----	----	----	----	----	----	----	----	----	----
	2011	-2.51	-0.04	14.61	0.97	0.21	0.01	21.95	0.7	-0.83	-0.04	8.28	0.91
	2012	0.91	0.01	14.17	0.96	0.86	0.06	22.5	0.67	1.25	0.06	8.36	0.88
	2013	0.26	0	14.61	0.97	0.42	0.03	19.89	0.74	0.98	0.05	9.56	0.85
	2014	0.19	0	12.85	0.97	1.01	0.07	21.07	0.71	0.8	0.04	8.23	0.87
	2015	2.13	0.03	13.93	0.96	1.51	0.1	20.22	0.73	1.21	0.06	7.87	0.88
	2016	0.83	0.01	14.35	0.96	1.52	0.1	21.89	0.69	0.99	0.05	7.73	0.9
	2017	0.95	0.01	15.75	0.96	0.84	0.06	22.26	0.71	-0.2	-0.01	7.98	0.9
	2018	-0.07	0	14.95	0.97	0.46	0.03	24.96	0.63	-0.96	-0.05	7.38	0.92
	2019	0.14	0	14.35	0.96	1.25	0.09	23.27	0.71	-0.55	-0.03	7.95	0.9
	2020	0.92	0.01	15.03	0.96	3.48	0.24	25.07	0.68	-0.12	-0.01	8.16	0.89
L91	2010	----	----	----	----	----	----	----	----	----	----	----	----
	2011	6.82	0.09	12.85	0.97	-0.18	-0.01	17.42	0.79	-2.18	-0.1	6.71	0.93
	2012	----	----	----	----	----	----	----	----	----	----	----	----
	2013	6.64	0.09	22.12	0.93	-35.83	-3.85	18.38	0.76	-35.04	-2.6	12.71	0.89
	2014	3.65	0.05	14.28	0.97	-26.87	-2.48	25.04	0.58	-27.03	-1.75	18.6	0.59
	2015	4.52	0.07	15.5	0.97	2.55	0.17	24.1	0.65	-2.54	-0.13	7.8	0.91
	2016	5.22	0.07	14.51	0.96	1.53	0.1	21.38	0.72	-2.84	-0.14	7.11	0.92
	2017	5.06	0.07	15.93	0.96	0.93	0.06	21.36	0.73	-2.56	-0.13	8.39	0.91
	2018	5.86	0.08	14.88	0.96	0.36	0.02	23.09	0.66	-3.14	-0.15	8.08	0.9
	2019	4.5	0.06	15.11	0.97	1.79	0.12	24.49	0.68	-2.81	-0.14	8.02	0.91
	2020	4.48	0.07	14.66	0.97	3.41	0.24	23.56	0.71	-2.71	-0.14	8.09	0.9

Obs: Color scales consider maximum and minimum values from results including Table 4 and Table 5.

This project has received funding from the Europeans Union’s Horizon 2020 research & innovation programme under grant agreement number 101036457.

2 Wind Energy Resource Assessment

2.1 Limitations of Existing Wind Databases

The utilization of numerical weather prediction models has been proven to be the best alternative in addressing offshore wind resource assessment. In the last few years, atmospheric reanalysis provided a significant boost to the offshore wind resource assessment, particularly due to their spatial resolution, temporal coverage, and free availability to the end users (Gualtieri, 2022). Several researchers have utilized state-of-the-art global and regional reanalysis datasets, such as ERA-Interim (Dee, 2011), MERRA2 (Gelaro, 2017), and ERA5 (Hersbach H. a.-S., 2020), in addressing the spatiotemporal variability of offshore wind resources, as well as in understanding the influence of atmospheric circulation patterns on wind power production.

These reanalysis data are capable of predicting the wind resource patterns over time. However, there are some limitations that persist with such reanalysis datasets, due to the still coarse grid resolution and hourly temporal frequency. Firstly, they seem to suffer uncertainties near the coastal boundaries due to poor representation of land-sea interactions (Gualtieri, 2022; Frank, 2020). Secondly, wind farm operations are significantly impacted by wind ramps at scales ranging from ten minutes to hours. Global reanalyses systematically underestimate the occurrence of more intense ramp rates and overestimate that of weak ramp rates (Frank, 2020). Thirdly, wind turbine wakes are one of the most important aspects of wind power meteorology because they decrease the power production and increase the loading of downstream wind turbines (Rodrigo, 2020; Port{\'e}-Agel, 2020). A horizontal resolution of a few hundred meters is inevitable to place each turbine of a wind farm in individual cells and account for intra-farm wake effects (Fischereit, 2022).

The most recent state-of-the-art regional reanalysis called Copernicus Regional Reanalysis for Europe (CERRA) (Schimanke S., 2021) has a resolution of 5.5 km, which is still insufficient to explain the intra-farm wake effects. In addition, for energy and economics modelling, it often needs 10 min time series data, which cannot be provided by reanalysis datasets. In tackling these limitations, regional numerical models, particularly the Weather Research and Forecasting (WRF) model, offer a cost-effective solution, providing extensive temporal coverage and sampling while maintaining high spatial resolution.

According to the studies of (Jimenez P. A., 2015; Eriksson, 2015), a horizontal grid resolution of turbine separation scale (a few hundred meters) is inevitable to accurately quantify the intra-farm wake effects. Even such super-scale resolution simulations come under the grey zone region, where large coherent overturning structures with a dominant turbulent length scale equal to that of the grid resolution will be partially resolved. This violates the fundamental assumption behind the turbulence parameterization, implying the accuracy of such simulations is compromised (Fischereit, 2022). Thus, a rigorous validation of such simulations is of paramount importance to quantify their accuracy.

This project has received funding from the Europeans Union's Horizon 2020 research & innovation programme under grant agreement number 101036457.

The majority of the relevant studies conducted so far have estimated wind resources for a limited period of time, ranging from one year to 25 years, and grid resolutions ranging from 5 km to 1 km. However, a curated dataset at turbine separation scale resolution is needed to accurately assess the potential wind resources and the wake losses over a region of interest, which is one of the motivations of the current study.

2.2 Wind model description (WRF)

Numerical Weather Prediction (NWP) models play a crucial role in achieving accurate representations of the atmospheric state. These models can be broadly categorized into two types: global models, which operate at resolutions of ten to hundreds of kilometers, and regional mesoscale models, which operate at a much finer resolution. The Weather Research and Forecasting (WRF) model falls under the category of regional mesoscale models. It utilizes initial and lateral boundary conditions from global models and simulates weather phenomena at a more localized scale.

Apart from the WRF model, there are several other notable regional models, including the Fifth-Generation Penn State/NCAR Mesoscale Model (MM5), the Hurricane Weather Research and Forecasting (HWRF) model, and the Tropical Cyclone Model (TCM3). However, due to its widespread availability and applicability for both research and operational weather prediction across various spatial scales ranging from meters to thousands of kilometers, the WRF model is considered to be one of the most reliable models for conducting numerical experiments.

The flowchart of the WRF model used within this framework (as depicted in Figure 13) is comprised by three major programs: the WRF Preprocessing System (WPS), Initialization, and the Advanced Research WRF (ARW) dynamical core. The WPS is responsible for preparing the driving data for the actual numerical simulations. It involves the Geogrid program, which defines the model domain and horizontal grid projection, and the Ungrib and Metgrid, which extract and interpolate meteorological data from external sources to be used by the WRF model.

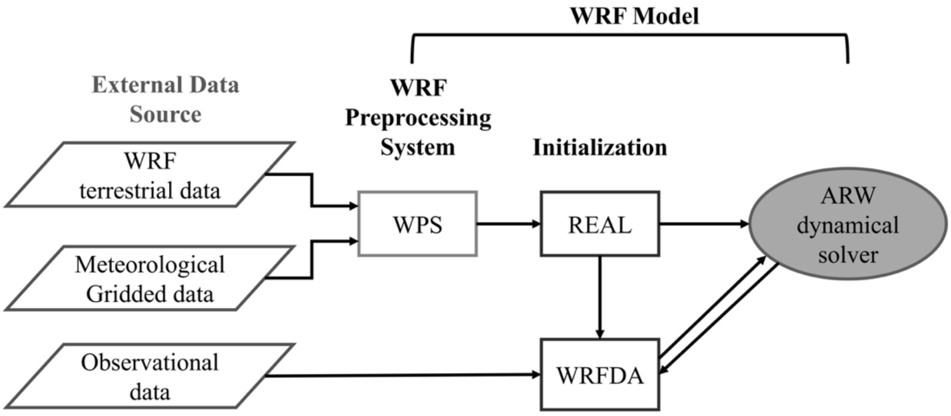

Figure 13: Flow chart of the WRF model, illustrating the basic components.

This project has received funding from the Europeans Union's Horizon 2020 research & innovation programme under grant agreement number 101036457.

Our Initialization program sets up the initial atmospheric conditions for the WRF simulation, while the ARW dynamical core forms the heart of the model, solving the fundamental equations of atmospheric motion and thermodynamics to simulate the evolution of the atmosphere over the specified regional domain.

To perform numerical simulations, the WRF model relies on driving data obtained from various external sources. This data includes both initial conditions (prepared by the Initialization program) and lateral boundary conditions, often sourced from global numerical weather prediction models that operate at coarser resolutions.

After completing the simulation, postprocessing tools are utilized to visualize and analyze the numerical simulation data obtained from the WRF model. These tools are invaluable in interpreting the model's output, enabling researchers and forecasters to extract valuable insights and make informed decisions.

In the subsequent sections, a comprehensive description of each component will be provided to explain the functionality and significance of the WRF model, in accurately representing atmospheric conditions through numerical experiments. A better description of the WRF model can be found in the WRF user guide (Powers, 2017).

2.2.1 External data source

The WRF model relies on specific data from various external sources to perform accurate numerical integration. The required data can be broadly categorized into three types: Terrestrial Data, Meteorological Gridded Data, and Observational Data.

2.2.1.1 Terrestrial Data

Terrestrial data constitute static geographical information that remains time-invariant. It includes essential characteristics of the Earth's surface, which are crucial for initializing the model and defining the simulation domain. Examples of terrestrial data used in the WRF model are:

- Soil categories
- Land use categories
- Terrain height
- Annual mean deep soil temperature
- Monthly vegetation fraction
- Monthly albedo
- Maximum snow albedo
- Slope category

As this data does not change with time, it needs to be downloaded only once and can be reused for subsequent simulations. Global datasets for each field are provided through the Geographical Static Data Downloads page (https://www2.mmm.ucar.edu/wrf/users/download/get_sources_wps_geog.html).

2.2.1.2 Meteorological Gridded Data

Meteorological gridded data comprises meteorological fields positioned on a regular grid at the Earth's surface and three-dimensional levels in the atmosphere. This data is obtained from global weather prediction models such as the Global

This project has received funding from the Europeans Union’s Horizon 2020 research & innovation programme under grant agreement number 101036457.

Forecasting System (GFS), ECMWF Integrated Forecasting System (IFS), Copernicus Regional Reanalysis for Europe (CERRA), and the UK MetOffice Unified Model (UM). Each model provides gridded data at different resolutions.

The meteorological gridded data is time-dependent and needs to be downloaded for each time step of the WRF model simulation. The following basic meteorological fields are essential for successful integration in the WRF model:

- 3-dimensional air temperature
- 3-dimensional relative humidity
- 3-dimensional specific humidity
- 3-dimensional wind u-component
- 3-dimensional wind v-component
- 3-dimensional geopotential height
- 3-dimensional pressure
- Surface pressure
- Mean sea-level pressure
- Skin temperature
- Soil height
- 2-meter air temperature
- 2-meter relative humidity
- 2-meter specific humidity
- 10-meter wind u-component
- 10-meter wind v-component
- Land-sea mask
- Soil moisture
- Soil temperature

The meteorological gridded data is available in the GRIB format, which is specifically designed for use in numerical weather prediction models. There are many meteorological datasets that exist currently, out of which the following two reanalysis datasets are used in the present work.

2.2.1.2.1 ERA5 reanalysis

ERA5 is the most commonly used global reanalysis dataset amongst those currently available, produced by the European Centre for Medium-Range Weather Forecasts (ECMWF). ERA5 has been released progressively since 2017 and is considered to be more wind-power friendly than its predecessor, ERA-Interim, offering an hourly resolution and a finer horizontal grid spacing of about 30km. The dataset includes data from 1950 to the present day and is regularly updated with new data.

For the modelling purposes of our WRF framework, the ERA5 hourly data on pressure levels between 1800UTC on February 21st and 1800UTC on February 22nd, 2016, as well as between 1800UTC on March 3rd and 1800UTC on March 4th, 2016, are used as driving data for numerical simulations. The data is available in the Copernicus Climate Data Store (https://cds.climate.copernicus.eu/#!/home).

This project has received funding from the Europeans Union's Horizon 2020 research & innovation programme under grant agreement number 101036457.

2.2.1.2.2 CERRA reanalysis

The Swedish Meteorological and Hydrological Institute (SMHI), in collaboration with the Norwegian Meteorological Institute (MET Norway) and Meteo-France, has developed a new reanalysis system for Europe called CERRA (Schimanke S., 2021).

This modernized system covers the period from the early 1980s to near real-time. It uses the Harmonie NWP system with ALADIN physics, Operational Interpolation (OI), and 3D-VAR for surface and upper-air analysis. CERRA provides a high-resolution pan-European reanalysis with a 5.5 km horizontal resolution and 106 vertical levels, covering Europe, Northern Africa, and the Southeastern parts of Greenland. The system is forced by the global ERA5 reanalysis and has an Ensemble Data Assimilation (EDA) system coupled with the deterministic CERRA system to regularly update the flow-dependent information in the background error covariance matrix (B-Matrix) used in the 3D-VAR deterministic system. The NWP has a 3-hourly cycling interval and produces 30 h forecasts at 00 and 12z assimilation times, while six h forecasts are generated at the 03, 06, 09, 15, 18, and 21z assimilation times. The EDA system is comprised by ten ensemble members with an 11 km horizontal resolution and a 6-hour cycling interval.

Unlike the ERA5 data, CERRA provides an analysis every three hours. Thus, in the current framework, the CERRA 3-hourly data on pressure levels and single levels between 1800UTC on February 21st and 1800UTC on February 22nd, 2016, as well as between 1800UTC on March 3rd and 1800UTC on March 4th, 2016, are used as driving data for numerical simulations. The CERRA dataset has been continuously updated and is available in the Copernicus Climate Data Store ().

2.2.1.3 Observational Data

Observational data is collected from various instruments, including buoys, radiosondes, radars, and satellites. This data also consists of meteorological fields but is instrument-specific. For instance:

- Radiosondes measure altitude, pressure, temperature, relative humidity, and wind profiles in the atmosphere.
- Radars measure the reflectivity of hydrometeors, providing information on precipitation patterns.
- Satellites measure brightness temperature and global winds, among other parameters, from space.

While the WRF model simulations primarily rely on terrestrial data and meteorological gridded data, observational data are used for data assimilation. Data assimilation helps correct the background error of the global meteorological gridded data, improving the accuracy of the model's initial conditions.

By utilizing these various types of data, the WRF model can effectively simulate atmospheric processes, enabling accurate numerical weather predictions and valuable insights for research and operational purposes.

2.2.2 Advanced Research WRF (ARW) dynamic core solver

The WRF model consists of Advanced Research WRF (ARW) dynamic core wrf.exe, which takes the wrfinput and wrfbdy files from real.exe and performs

This project has received funding from the Europeans Union's Horizon 2020 research & innovation programme under grant agreement number 101036457.

numerical integration, governed by the instructions provided in namelist.input file.

2.2.2.1 Governing equations

The dynamic core of the model is Advanced Research WRF (ARW), which solves the compressible, non-hydrostatic flux form of Euler equations. The equations governing the flow and heat transfer in a three-dimensional earth's atmosphere are the well-known continuity equation, the Navier-Stokes equations, the equation of energy together with the equation of geopotential, and the equation of state. The equations are formulated in terrain-following hydrostatic pressure coordinate system, taking the hydrostatic pressure as an independent variable.

2.2.2.2 Parameterization schemes

The physical processes which cannot be resolved to the model grid by an NWP model (sub-grid scale processes) are represented empirically or statistically by means of parameterization. The WRF model employs seven parameterization categories, each responsible for representing specific physical processes. These parameterization categories are as follows:

1. **Land Surface Parameterization:** This category deals with the physics of the Earth's land surface, including processes related to soil moisture, heat transfer, and vegetation dynamics.
2. **Surface Layer Parameterization:** Surface layer physics parameterization focuses on the interactions between the atmosphere and the Earth's surface, such as turbulent heat fluxes and momentum transfer.
3. **Planetary Boundary Layer Parameterization:** Planetary boundary layer physics parameterization accounts for the atmospheric layer closest to the Earth's surface, where turbulence plays a significant role in vertical mixing and exchange of properties like heat and moisture.
4. **Convective Parameterization:** Cumulus physics parameterization handles convective processes, representing the effects of subgrid-scale convective clouds that influence precipitation and vertical heat transport.
5. **Microphysics Parameterization:** Microphysics parameterization involves modeling processes related to cloud and precipitation formation, including the representation of cloud droplets, ice crystals, and precipitation particles.
6. **Shortwave Radiation Parameterization:** This parameterization represents the interactions of shortwave solar radiation with the atmosphere and the Earth's surface.
7. **Longwave Radiation Parameterization:** Longwave radiation parameterization deals with the interactions of longwave infrared radiation with the atmosphere and the Earth's surface.

Within each of these physics categories, several parameterization schemes have been developed by various researchers. These schemes utilize empirical or mathematical relationships to explain the behavior of specific physical processes and are designed to suit different atmospheric conditions and spatial scales.

This project has received funding from the Europeans Union's Horizon 2020 research & innovation programme under grant agreement number 101036457.

2.2.2.3 Numerical integration

The discretized form of Euler equations, **Error! Reference source not found.** is integrated in time using the third-order Runge-Kutta method. The courant number limitation of the model time step can be written as,

Equation 15 $$\Delta t_{max} < \frac{Cr_{theory}}{\sqrt{3}} \times \frac{\delta x}{u_{max}}$$

Where δx is the grid size, and u_{max} is the maximum horizontal velocity. For computational ease, the WRF model uses staggered grids, in which the *u*, *v*, and *w* velocities are computed at the cell boundaries, and mass-related quantities such as pressure, temperature, and humidity are computed at the cell center. The discretized equations are integrated into space using the 6th order center difference method.

2.3 Novel Hybrid CERRA-ERA5 based WRF simulation strategy

The WRF model version 4.4, publicly available at https://github.com/wrf-model/WRF/releases/tag/v4.4, was used to hindcast winds in the present study. The default configuration of WRFv4.4 includes reanalysis and forecast data types like ERA5 reanalysis and GFS forecasts for initial and boundary conditions. However, the newly available CERRA reanalysis data, released in August 2022, was not initially integrated into the model configuration. Upon evaluating the accuracy of the ERA5 and CERRA reanalysis datasets in comparison with the observations, it was found that the ERA5 overestimates the mode of wind speed and also underestimates the wind extremes. This is evident in Figure 14.

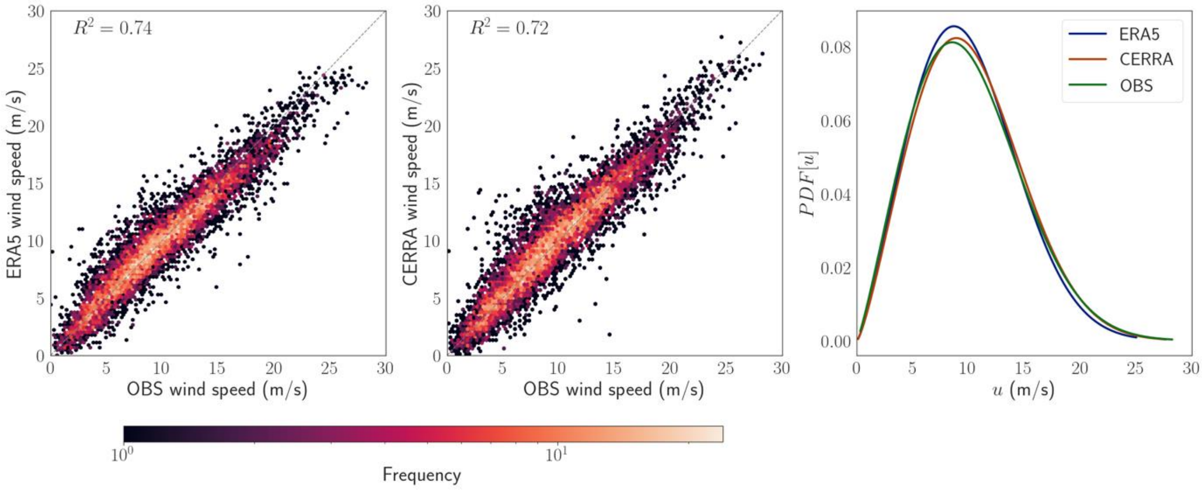

Figure 14: A comparison between the ERA5 and CERRA reanalysis with respect to the observations, at the FINO1 wind mast location. The datasets are obtained during 2011, at hourly interval.

To overcome this limitation, a novel hybrid simulation strategy was developed for the EU-SCORES project, combining the CERRA and ERA5 datasets. This approach allows for improved representation of atmospheric conditions and enhances the accuracy and applicability of the WRF model for the study's objectives.

To successfully incorporate the CERRA data into the WRF model, it is necessary to ensure that all the required meteorological variables are present in the dataset and

This project has received funding from the Europeans Union's Horizon 2020 research & innovation programme under grant agreement number 101036457.

can be understood by the model using a Vtable file. The WRFv4.4 user guide provides detailed instructions for creating a custom Vtable file containing the necessary meteorological variables. Upon investigation, it was determined that all surface and upper-level variables required by the WRF model, except soil moisture and soil temperature, are available in the CERRA data, as listed in Table 6.

Table 6: Overview of the meteorological variables obtained from the CERRA reanalysis.

CERRA data type	Variables
Pressure level	U wind, V wind, geopotential, temperature, relative humidity
Single level surface	Land-sea mask, mean sea level pressure, skin temperature, snow depth, surface pressure, water equivalent snow depth
Single level atmospheric	10m wind speed, 10m wind direction, 2m relative humidity, 2m temperature

The WRF model recognizes wind components (U and V) rather than wind speed and direction at 10 meters. Therefore, the 10-meter wind speed and direction from the CERRA data are converted into 10-meter U and V components and written to a separate grib2 file. Since the CERRA data is in grib2 format, similar to GFS forecasts, while ERA5 data is in grib1 format, a new Vtable specific to the CERRA data is created based on the GFS Vtable file. The variable grib codes in the newly created Vtable are adjusted according to the information provided in the downloaded CERRA data files.

Using the custom Vtable, the CERRA data is ungribbed first. However, since the CERRA data does not include soil moisture and soil temperature, these variables are obtained from the ERA5 reanalysis. To do this, a different Vtable corresponding to ECMWF pressure levels is used for ungribbing the ERA5 data.

Once the CERRA and ERA5 data are ungribbed, the final metfiles are generated, which incorporate all the necessary meteorological variables required for the WRF simulations. This comprehensive process ensures that the WRF model is well-informed with the appropriate data for a successful and accurate simulation using the CERRA dataset.

2.4 Wind Model Calibration

The WRF model simulation accuracy depends on several factors, including physics parameterization schemes, grid resolution, and domain configuration. Since the present work aims to obtain decadal super-scale resolution (500 m) hindcasts, it is necessary to conduct sensitivity of physics scheme and domain configuration, and obtain best combination.

In doing so, we chose to simulate two extreme events, that are frontal low-level jets (FLLJ), using different physics scheme configurations. The FLLJ is a band of strong winds with velocities ranging from 25 to 30 m/s, within the 900-850 mb pressure level, and typically forms ahead of a cold frontal surface. FLLJ is regarded as a synoptic scale phenomenon, stretching over several hundred kilometres ahead of the frontal surface, notably in the extratropical region. One significant

This project has received funding from the Europeans Union's Horizon 2020 research & innovation programme under grant agreement number 101036457.

characteristic of the FLLJs is that wind speed decreases abruptly right behind the frontal surface, accompanied by the abrupt change in wind direction.

2.4.1 Description of case studies

2.4.1.1 Case 1: Cold frontal passage during 22nd-23rd February 2016

On 22nd February 2016, the Belgian offshore wind farms observed a peak in wind speed at the hub height, resulting in maximum power output. However, the wind farms also experienced a 68% drop in their overall wind power within three hours, from 0515 UTC to 0815 UTC on 22nd February. The synoptic charts provided by UKMO, at 00UTC of 22nd and 00UTC of 23rd on February, are presented in Figure 15 (top panel), which illustrates a strong cold front (dark line with triangles pointing the direction of frontal movement) crossing the Belgian coast. In addition, the wind power production observed by the Belgian wind farms from 1800UTC of 21st to 1800UTC of 22nd February presented in Figure 15 (bottom panel) clearly shows the ramp-down event from 0500UTC to 0800UTC of 22nd February.

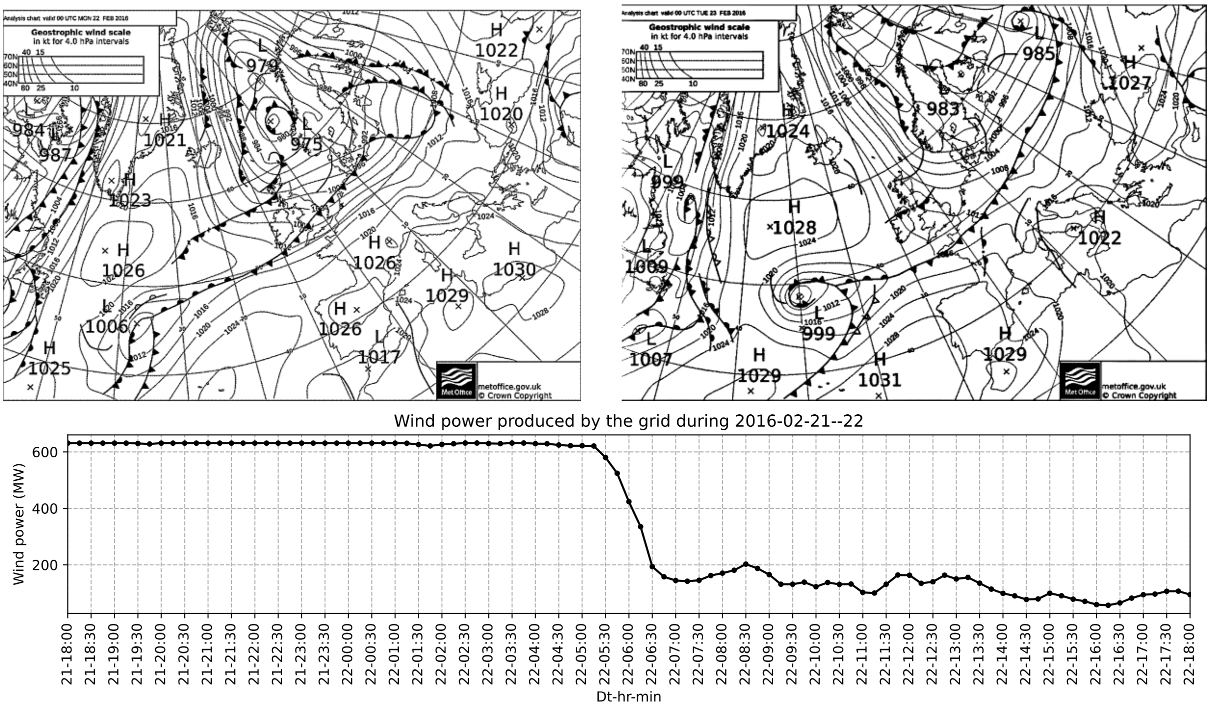

__Figure 15:__ Synoptic weather maps of cold frontal passage at 0000 UTC on 22nd (left panel) and 23rd February 2016 (right panel). The bottom panel shows the time series of wind power production by the Belgian offshore wind farms (bottom panel), from 1800 UTC on the 21st to 1800 UTC on the 22nd of February 2016, which depicts the wind ramp event. The total capacity of the wind farms is 712 MW. Source: https://www.elia.be/.

2.4.1.2 Case 2: Cold frontal passage during 4th-5th March 2016

In another event, On March 4th, 2016, the Belgian offshore wind farms experienced a sudden increase in wind speed at the hub height, resulting in maximum power output. However, this was short-lived as the wind farm suffered a 90% drop in capacity within just three hours (from 0515 UTC to 0815 UTC on the same day) due to a severe weather event. Figure 16 (top panel) displays the synoptic charts from UKMO at 00UTC on March 4th and 5th, which showed a strong cold front passing the Belgian coast during this time period. Figure 16 (bottom panel) depicts the wind power production by the wind farms between 1800UTC on the 4th to

1800UTC on the 5th, showing a ramp-down event from 0500UTC to 0800UTC on February 4th.

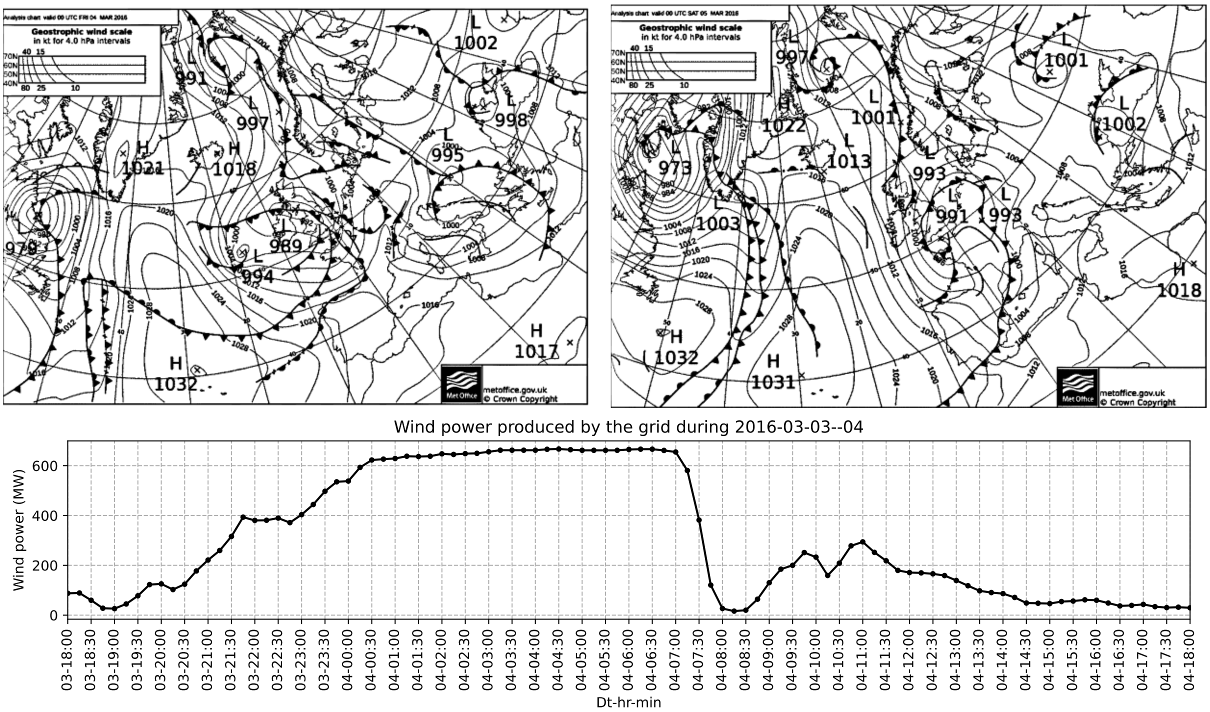

Figure 16: *Synoptic weather maps of cold frontal passage during 4th March 2016 (top left panel) and 5th March 2016 (top right panel). The bottom panel shows the time series of wind power measured by the Belgian offshore wind farms (bottom panel), from 1800 UTC on the 3rd to 1800 UTC on the 4th of March 2016. The total capacity of the wind farms is 712 MW.*

2.4.2 Description of dataset

In this calibration, diverse sets of data are utilized, such as the reanalysis and forecast data used to run the numerical simulations, whereas observations obtained from wind farms and meteorological instruments are employed to validate the simulations. The subsequent subsections offer a comprehensive overview of the data utilized in our framework.

During February-March 2016, the Belgium offshore wind farm consisted of three operational projects: the C-Power, Northwind, and Belwind-I, which have a capacity of 712MW combined. The aggregated power production data from these wind farms is available at a sampling rate of every 15 minutes, which has been quality-controlled by Elia to handle any missing data. The power production data during February and March of 2016 has been analyzed, and two case studies have been identified from the time-series analysis. Furthermore, the power production data from 1800UTC of 21st to 1800UTC of 22nd February 2016 has been utilized to evaluate the numerical simulations of case 1. Similarly, the data from 1800UTC of 3rd to 1800UTC of 4th March 2016 has been utilized in the evaluation of case 2.

During the observed weather events, a floating LiDAR (Light Detecting And Ranging) wind profiler has been operating in the North Sea, very close to the

Belgian offshore wind farms. FUGRO has deployed the SEAWATCH wind LiDAR buoys at LOT1 (latitude: 51°42.414' and longitude: 3°02.0771'). The LiDAR measure wind speed and direction at 4 m and 30 m height and from 40 m up to 200 m at 20 m intervals and record the data at a time latency of 10 minutes. The LiDAR has recorded 100% data during the selected weather events, and the data has been quality controlled and released to the public by TNO.

For our work within the project wind observations recorded between 1800UTC on February 21st and 1800UTC on February 22nd, 2016, as well as between 1800UTC on March 3rd and 1800UTC on March 4th, 2016, are utilized to assess the accuracy of the simulations. ERA5 hourly data on pressure levels between 1200UTC on February 21st and 1800UTC on February 22nd, 2016, as well as between 1200UTC on March 3rd and 1800UTC on March 4th, 2016, are used as driving data for numerical simulations.

the CERRA 3-hourly data on pressure levels and single levels between 1200UTC on February 21st and 1800UTC on February 22nd, 2016, as well as between 1200UTC on March 3rd and 1800UTC on March 4th, 2016, are used as driving data for numerical simulations.

The Global Forecast System (GFS) by the National Centers for Environmental Prediction (NCEP) provides forecasts for various weather variables globally. The GFS has a 0.25 horizontal resolution, 127 vertical layers, and offers hourly forecasts for the first 120 hours, followed by three-hourly forecasts for days 5-16. For the EU-SCORES model validation framework, GFS 0.25 forecast data at 3-hour intervals are used for WRF simulations.

2.4.3 Design of Experiments and Outcomes

A total of six simulations were conducted to investigate the influence three types of forcing data, two planetary boundary layer schemes, and three grid resolutions. Additionally, the study also assessed the impact of the wind farm parameterization (WFP) developed by (Fitch, 2012), which is included in WRF.

Table 7 provides a concise overview of the six WRF simulations conducted in the present study. The area of interest is centered around the wind farm zone, and three types of domain configurations and grid resolutions are used in the simulations. The experiments WRF-ERA5 utilize the ERA5 reanalysis at hourly frequency as driving data. The experiments are configured with three nested domains, downscaling from 9 km in the outer domain to 1 km in the inner domain, with the innermost domain consisting of 301*301 grid points. The experiments WRF-CERRA, WRF-CERRA*, and WRF-CERRA+ utilize the CERRA reanalysis data at a 3-hour input frequency. Since the CERRA data is available at a resolution of 5.5 km, these three experiments are configured with a single domain at a 1 km grid resolution, also consisting of 301*301 grid points, to maintain consistency.

The WRF-CERRA# experiment also uses the CERRA reanalysis, but the resolution in the interested domain is further reduced to 0.5 km to examine the impact of grid resolution. To accommodate this change, the experiment is configured with two nested domains, with the innermost domain consisting of 601*601 grid points, to maintain consistency.

This project has received funding from the Europeans Union's Horizon 2020 research & innovation programme under grant agreement number 101036457.

Further, the GFS forecast data at a 3-hour input frequency are utilized as the driving data in the WRF-GFS experiments to examine the forecasting ability of the WRF model for the selected cases. These experiments also utilize the same domain configuration as WRF-ERA5 due to the similarity in the resolution of the driving data.

Table 7: Overview of the WRF simulations conducted for the sensitivity assessment.

WRF run	**IC/BC (frequency)**	**Grid size, km**	**Grid points**	**Time step, s**	**PBL scheme**	**Wind farm scheme**
WRF-ERA5	ERA5 (1hr)	9, 3, 1	211x187, 244x244, 301x301	30, 10, 3.33	MYNN 2.5	on
WRF-CERRA	CERRA (3hr)	1	301x301	3	MYNN 2.5	on
WRF-CERRA*	CERRA (3hr)	1	301x301	3	MYNN 2.5	off
WRF-CERRA+	CERRA (3hr)	1	301x301	3	SH	off
WRF-CERRA#	CERRA (3hr)	1.5, 0.5	488x488, 601x601	6, 2	SH	off
WRF-GFS	GFS operational (3hr)	9, 3, 1	211x187, 244x244, 301x301	30, 10, 3.33	MYNN 2.5	on

Figure 17 illustrates the domain configuration adopted for all the experiments, where the three nested domains D01, D02, and D03 are used in WRF-ERA5 and WRF-GFS experiments, the two nested domains in Figure 17(b) and (c) are used in the WRF-CERRA# experiment, and the single domain in (c) is used in WRF-CERRA, WRF-CERRA*, and WRF-CERRA+ experiments. This ensures that the innermost domain size remains consistent across all experiments. The domain configuration is carefully chosen to ensure that the Alps fit completely into a domain, avoiding steep topography near the boundary edges. In (c), the locations of observations LOT1 are represented with violet star, while the wind turbines are represented with circles.

Previous research has emphasized the critical role of the planetary boundary layer (PBL) scheme in accurately representing wind interactions and turbulence in the lower atmosphere, specifically at the wind turbine hub height (Nunalee, 2014). In addition, the domains have been configured with sub-kilometer resolution, which is clearly a gray-zone for physics parameterization. In such cases, the use of appropriate gray-zone PBL scheme is inevitable. Therefore, our model focuses on evaluating the influence of two different PBL schemes, namely MYNN2.5, which has been adopted from the studies of (Li, 2021), and Shin Hong (SH) scheme, which is indeed a gray-zone scheme, adopted from the studies of (Vemuri, 2021).

This project has received funding from the Europeans Union's Horizon 2020 research & innovation programme under grant agreement number 101036457.

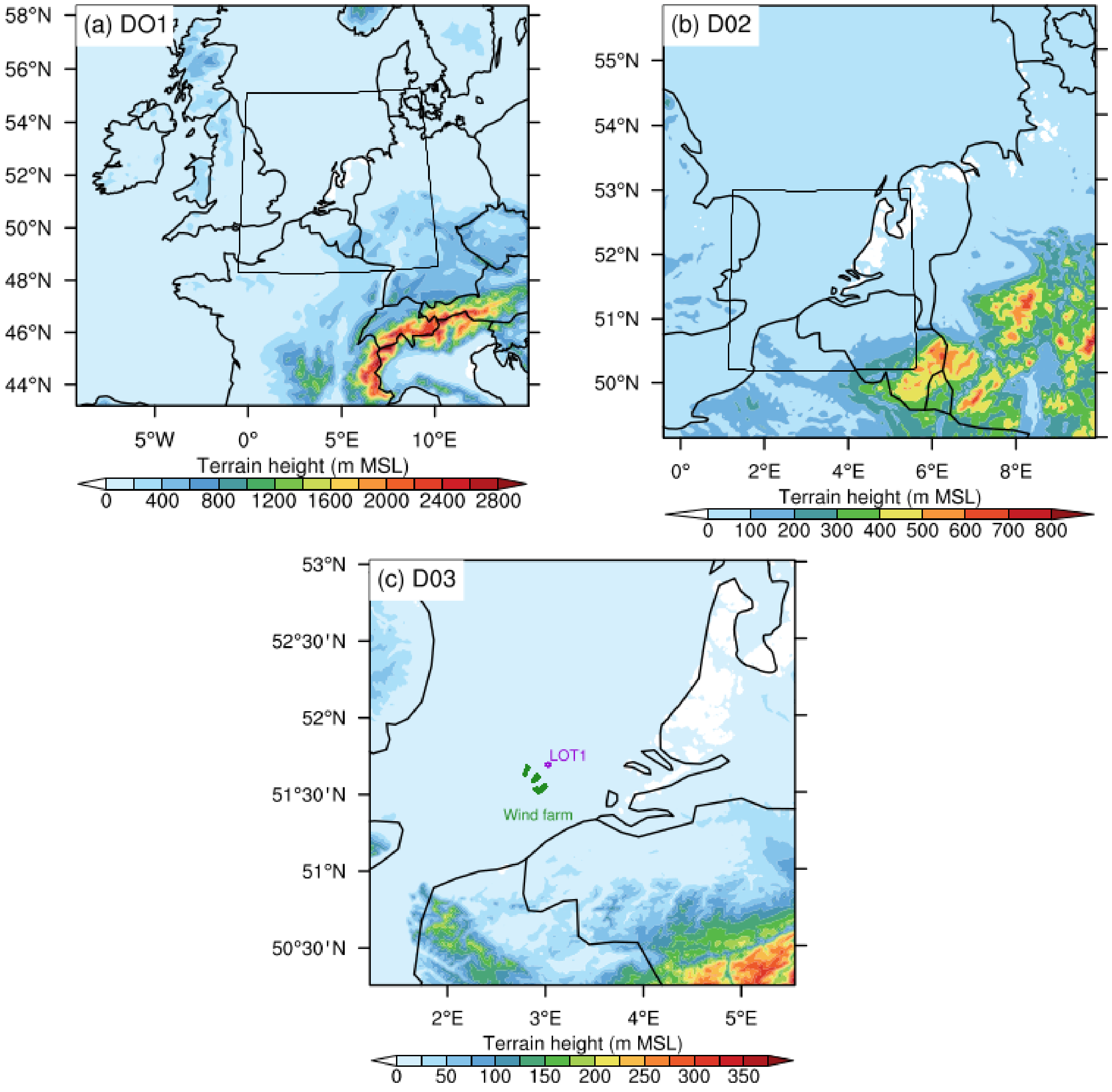

Figure 17: The simulation domains adopted for the WRF simulations are shown, providing a topographical overview. The domains are carefully designed to avoid any steep topography at the boundaries, ensuring that the Alps are fully contained within a domain. Subfigures (a), (b), and (c) illustrate the domain configuration for the WRF-ERA5 and WRF-GFS experiments, while subfigures (b) and (c) depict the domain configuration for the WRF-CERRA# experiment. Subfigure (c) showcases the domain configuration for the WRF-CERRA, WRF-CERRA*, and WRF-CERRA+ experiments. In subfigure (c), the location of LiDAR observational cite LOT1 is denoted with violet star, and the locations of the Belgium offshore wind farm are depicted with green circles.

Additionally, the impact of the Fitch wake flow parameterization (WFP) is assessed in conjunction with the MYNN2.5 PBL scheme, as the WFP has only been coupled with the MYNN2.5 scheme. The experiments WRF-CERRA, WRF-ERA5, and WRF-GFS employ the MYNN2.5 PBL scheme with the Fitch WFP activated, while the WRF-CERRA* experiment uses the MYNN2.5 scheme without any WFP. On the other hand, the WRF-CERRA+ and WRF-CERRA# experiments utilize the SH PBL scheme without any WFP activation. For our framework, the MYNN surface layer scheme is used in combination with the MYNN2.5 PBL scheme, while the Revised MM5 surface layer scheme is adopted for the experiments with the Shin-Hong PBL scheme. The remaining physics schemes, including WRF single moment 5-class scheme for microphysics, RRTMG for shortwave and longwave radiation, Unified NOAH for land surface physics, and Kain-Fritsch for cumulus physics, are adopted from the studies of (Li, 2021). The simulations are conducted with a total of 51 vertical levels, spanning from approximately 8 meters above the surface to around 16 kilometers high, with non-uniform grid spacing. The lowest 1 kilometer of the model atmosphere comprises 18 levels.

Event 1 is simulated from 1200 UTC on 21st February 2016 to 1800 UTC on 22nd February 2016, while Event 2 is simulated from 1200 UTC on 3rd March 2016 to 1800 UTC on 4th March 2016. The simulations run for a total of 30 hours, with the initial 6 hours considered as a spin-up period to allow the model to reach a steady state. Output variables, namely wind speed and direction are recorded at 5-minute intervals. If the WFP is activated, the WRF simulation can directly provide wind power production data. For simulations without WFP, wind power production is calculated utilizing the turbine thrust and power curves and the wind speed at the hub height.

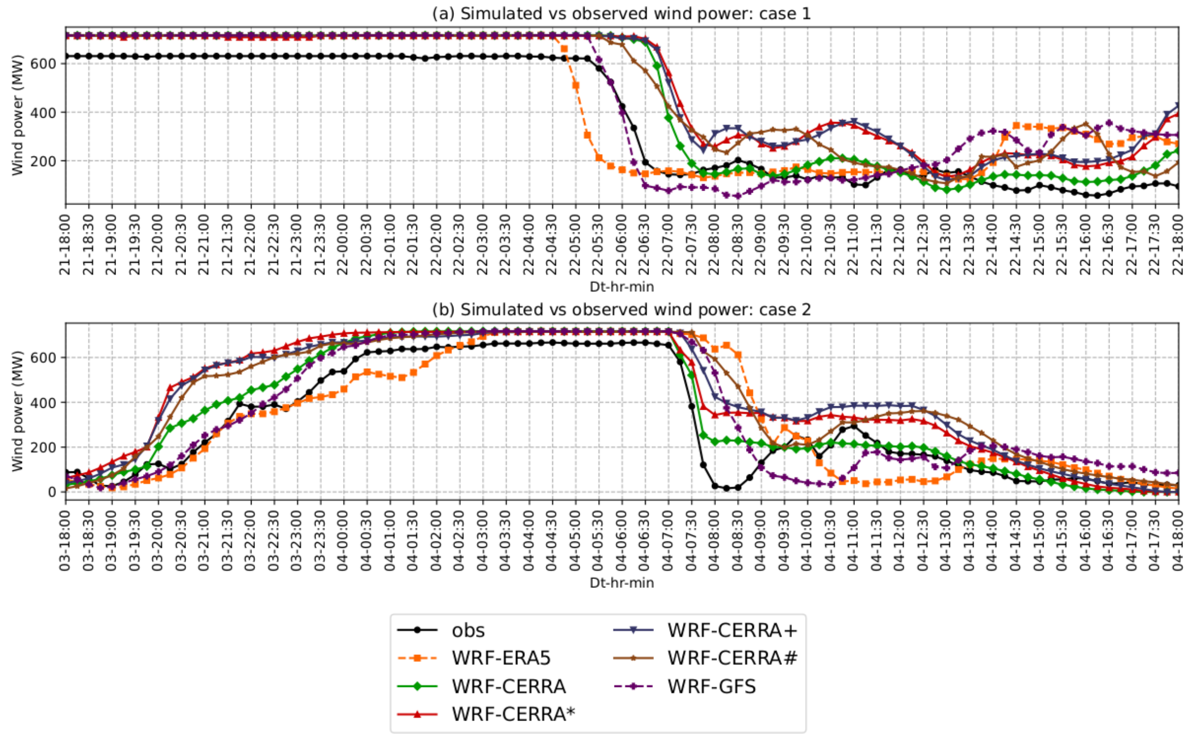

Figure 18: Illustration of the time series of wind power simulated by the six WRF model configurations WRF-ERA5, WRF-CERRA, WRF-CERRA*, WRF-CERRA+, WRF-CERRA#, and WRF-GFS, in comparison with the wind power produced by the Belgium offshore wind farm, (a) during 1800 UTC of 21st February to 1800 UTC of 22nd February 2016; and (b) during 1800 UTC of 3rd March to 1800 UTC of 4th March 2016.

This project has received funding from the Europeans Union's Horizon 2020 research & innovation programme under grant agreement number 101036457.

Figure 18 illustrates the time series of wind power obtained from the WRF simulations along with the generated power from the wind farms for case 1 and case 2. In case 1, the wind farms experienced a maximum wind power production for about 11 hours, beginning at 1800 UTC on the 21st and ending at 0500 UTC on the 22nd. However, the grid's wind power remained consistently about 100 MW lower than the rated power, suggesting curtailment likely for damage mitigation during peak wind speeds.

WRF simulations showed rated wind power production, overestimating compared to observations. The observational data reveals a significant decline in wind power, starting from its peak at 620 MW at 0515 UTC, subsequently dropping to its lowest point of 150 MW at 0715 UTC on the 22nd. Among all the simulations, the WRF-GFS simulation closely matched the observed ramp period. However, the wind power at the end of the ramp period was even lower than the observed data, signifying a substantial overestimation of the ramp's intensity. Subsequently, the WRF-ERA5 simulation exhibited an early power ramp, transitioning from 712 MW at 0430 UTC to 150 MW at 0630 UTC on the 22nd, indicating a slight overestimation of the ramp magnitude with a weak correlation to the observations.

WRF simulations driven by CERRA data, WRF-CERRA# demonstrated alignment in the start of the ramp but featured a prolonged ramp rate. Conversely, the remaining simulations produced a ramp much later in time and with a steep ramp rate. A notable observation is that only the WRF-CERRA simulations managed to replicate the wind power output of 150 MW at the end of the ramp period, mirroring the observational data, while the other simulations failed to attain the lower wind power level, reaching a minimum of 250 MW. However, the ramp intensity for the WRF-CERRA simulations was notably lower compared to the others due to the initial overestimation of wind power at the commencement of the ramp period. Following the ramp period, only the WRF-CERRA simulation demonstrated power levels close to 100 MW, consistent with the observed data, while all other simulations significantly overestimated wind power, generating more than 200 MW.

In case 2, a significant increase in wind power production was observed from 1800 UTC on the 3rd to 0030 UTC on the 4th. During this period, wind power generated by the wind farms gradually rose from a minimum of 20 MW to 600 MW. Notably, WRF-ERA5, WRF-GFS, and WRF-CERRA simulations exhibited a similar trend in wind power, while the remaining simulations displayed a substantial increase that deviated from the observational data. The wind farms consistently produced 600 MW from 0030 UTC to 0700 UTC on the 4th, exceeding 620 MW post 0300 UTC. During this interval, all simulations yielded a rated wind power output of 712 MW, with the exception of WRF-ERA5, suggesting an overestimation of intensity but a good correlation with the observations. The observed wind power exhibited a sharp decline from 650 MW at 0700 UTC to a subsequent minimum of 10 MW at 0815 UTC on the 4th, indicative of an intense power ramp event characterized by a steep ramp rate gradient. Wind power gradually increased from this minimum, reaching 300 MW at 1100 UTC, before steadily decreasing thereafter. Among the WRF simulations, only WRF-CERRA closely mirrored the observed ramp rate,

This project has received funding from the Europeans Union's Horizon 2020 research & innovation programme under grant agreement number 101036457.

dropping from 712 MW to 210 MW during the observed ramp period, implying the occurrence of a significant power ramp event.

WRF-ERA5 exhibited the most significant deviation from the observed ramp event, while the remaining simulations fell in between. Notably, none of the CERRA simulations managed to replicate the observed low-power levels. Although WRF-ERA5 and WRF-GFS produced a period of low power, they exhibited a substantial timing error, resulting in a weak correlation with the observed data. From the end of the ramp event until 1300 UTC on the 4th, the WRF simulations significantly deviated from the observed wind power levels, with the exception of WRF-CERRA, which closely followed the observed data. Beyond this period, all simulations produced wind power levels that closely matched the observed data, with minor deviations. The time series of wind power from both cases clearly underscores the superior performance of the CERRA driving data when combined with the Fitch wind farm parameterization.

Figure 19(a-g) provide visual representations of time-height cross-sections for wind speed from observations as well as simulations at the LOT1 site. From 1800 UTC on the 21st until 0100 UTC on the 22nd, the LiDAR buoy measurements vividly exhibit wind speed peaks exceeding 19 m/s, occurring as low as 50 m level, which further escalates to over 26 m/s at a height of 200 m level. Wind speed at the turbine height level (70 m to 100 m) consistently ranges between 21-18 m/s from 1800 UTC on the 21st until 0100 UTC on the 22nd and then stays at 18-16 m/s until 0530 UTC. These noticeable wind speed maxima strongly indicate the presence of an FLLJ and are indeed responsible for the peak wind power production experienced by the wind farms.

All the WRF simulations have reproduced the FLLJ but show significant differences in the cross-sectional structure and magnitude. In the WRF-ERA5 simulation, the FLLJ is seen earlier than observed, due to which the wind speeds at different vertical levels are notably higher than the corresponding observational data. For instance, at the 50 m level, wind speeds reach 21 m/s, while at the turbine height level (70-100 m), they range between 22-23 m/s.The wind speed cross-section obtained from the WRF-GFS simulation, which is conducted to emulate a forecast, closely resembles that of the WRF-ERA5 due to the similarity in domain configuration and physics schemes. The intense FLLJ of 25 m/s at 200m level is seen from 1800 UTC to 2100 UTC on the 21st, which is even more short-lived than WRF-ERA5 and observations. However, WRF-GFS shows relatively constant FLLJ strength at and below the turbine height level until 0130 UTC on the 22nd, which is in better agreement with the observation than WRF-ERA5.

This project has received funding from the Europeans Union's Horizon 2020 research & innovation programme under grant agreement number 101036457.

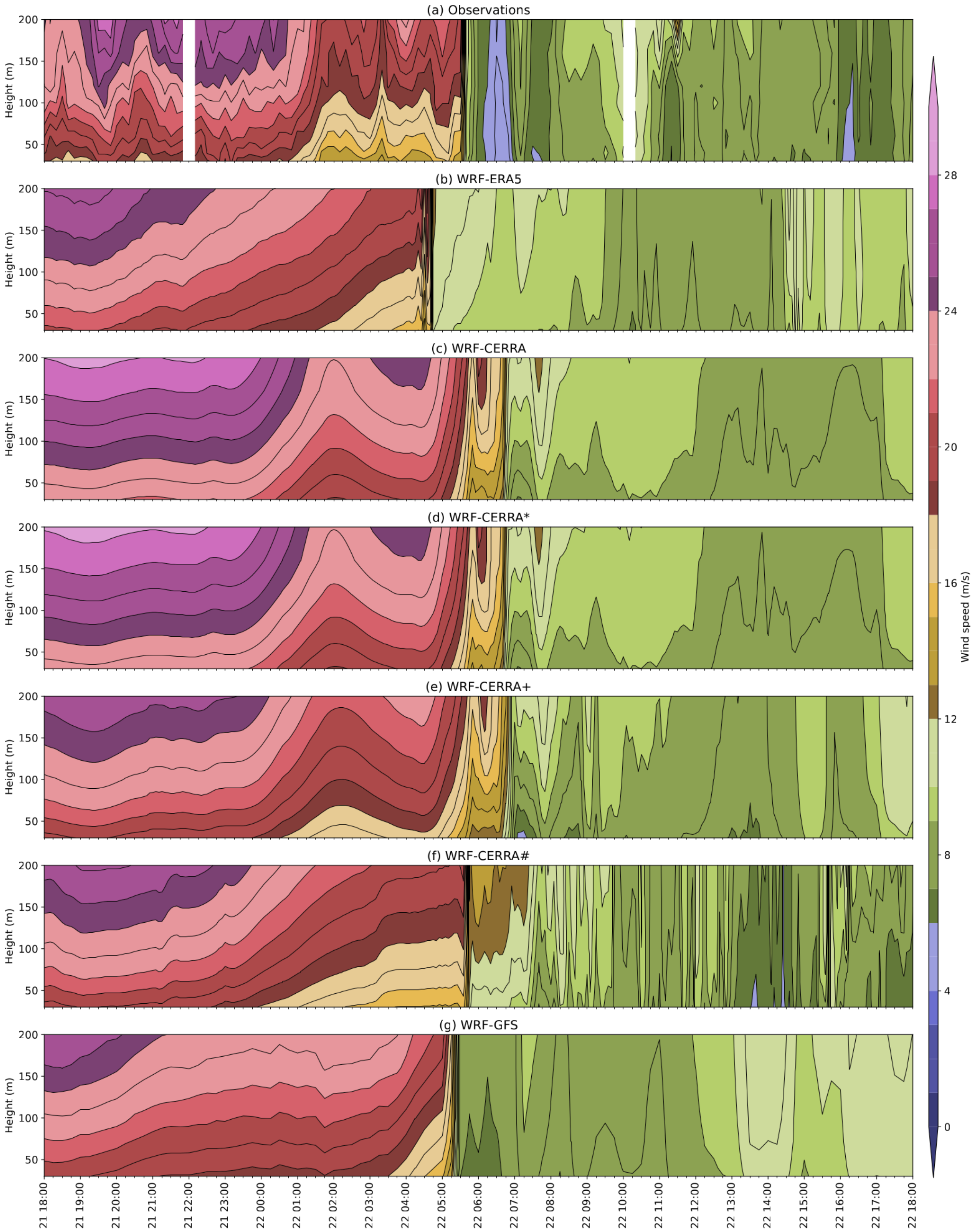

Figure 19: Time-height cross-sections of wind speed at the LOT1 location for Case 1, spanning from 1800 UTC on February 21st to 1800 UTC on February 22nd, 2016. The cross-sections include wind speed data obtained from various sources: (a) observational data and WRF model simulations using different configurations, including (b) WRF-ERA5, (c) WRF-CERRA, (d) WRF-CERRA*, (e) WRF-CERRA+, (f) WRF-CERRA#, and (g) WRF-GFS. The simulated data is taken from the innermost domains, which is D03 for WRF-ERA5 and WRF-GFS, D01 for WRF-CERRA, WRF-CERRA*, and WRF-CERRA+, and D02 for WRF-CERRA#.

This project has received funding from the Europeans Union's Horizon 2020 research & innovation programme under grant agreement number 101036457.

The vertical structure of wind speed seen in the WRF simulations with the CERRA driving data exhibit notable similarities among one another and show subtle differences compared to the WRF-ERA5 and WRF-GFS. In particular, the WRF-CERRA, WRF-CERRA*, and WRF-CERRA+ have similar structures due to the use of the same domain configuration. Further, the WRF-CERRA and WRF-CERRA* have exactly identical structures since the only difference between them is the use of Fitch WFP, which seems to have no influence on the wind speed simulation due to the fact that the observational site lies outside of the wind farm zone. This could be attributed to the fact that the LOT1 location lies outside of the wind farm zone.

The MYNN 2.5 PBL scheme adopted in these two simulations greatly overestimated the FLLJ strength, with wind speeds at the 50m level reaching as high as 23 m/s, at 200m level peaks greater than 28 m/s, and within the turbine level height (70-100 m) reaching as high as 24 m/s. These findings suggest that the FLLJ occurred at a lower height with greater intensity compared to the observations. On the other hand, the SH PBL scheme adopted in WRF-CERRA+ shows an FLLJ of strength consistently 2 m/s lower at all vertical levels compared to the MYNN 2.5 simulations and is aligning more closely with the observation. These findings suggest that the SH scheme, which is a gray-zone scheme, has better predictability of wind speed than the MYNN2.5. These three simulations show a slight drop in wind speed at 0200 UTC on the 22nd, similar to that of the observed one, but fail to stabilize, instead increasing again.

The WRF-CERRA# simulation, which is primarily distinguished by the use of nested domain configuration with a super-scale resolution of 0.5 km and the SH PBL scheme, exhibits subtle differences when compared to the other CERRA simulations. From 1800 UTC on the 21st to 0100 UTC on the 22nd, the cross-section is similar to that of the WRF-CERRA+ and also aligns closely with the observations. The peak wind speed of the FLLJ at 200 m altitude exceeds 25 m/s, mirroring the observed value but with a temporal shift. The slight wind speed drop seen at 0130 UTC is also replicated by the WRF-CERRA#, but this simulation alone reproduces the subsequent period of steady wind speeds from 0130 to 0530 UTC.

The aforementioned findings corroborate the existence of FLLJ and its contribution to the maximum wind power production. However, right after 0530 UTC, the observed wind speed precipitously drops to 11 m/s within 30 minutes, eventually reaching an all-time low of 4 m/s by 0615 UTC. This abrupt drop in wind speed within the short span indicates the occurrence of an extreme wind ramp event. Once the frontal system completely overpasses the location, wind speeds seem to stabilize close to 7-8 m/s, with occasional fluctuations around 6 m/s. On the other hand, the WRF simulations successfully reproduced this extreme ramp event but with differences in ramp timing and intensity. Particularly, the WRF-ERA5 shows the wind speed ramp 1 hour earlier than observed, whereas WRF-GFS closely aligns with the observed timing. After analyzing the ERA5 reanalysis, it was found that a gradual wind ramp is indeed present around 0630 UTC, but the WRF model simulated it much earlier. Furthermore, these two simulations show a uniform wind speed drop across all levels, with no vertical variation, a behavior seen in the observations. In contrast, the CERRA simulations do show a wind fluctuation

This project has received funding from the Europeans Union's Horizon 2020 research & innovation programme under grant agreement number 101036457.

around the observed instance but have a secondary strong ramp after 1 hour. When we checked the CERRA reanalysis, a ramp with less rate was observed around 0600-0700 UTC, which is indeed coinciding with the secondary ramp in the WRF simulations. In addition, all these simulations seem to have vertical variations in wind speed during the ramp, unlike the observations. The post-frontal conditions simulated by all the WRF simulations seem to stabilize around 8 m/s, similar to that of the observations.

The time-height cross-sections of wind speed from observations and simulations for case 2 are presented in Figure 20(a-g). In the observed cross-section, wind speeds consistently exceed 12 m/s at all altitudes from 2330 UTC on the 3rd onward, aligning with turbine peak power specifications for maximum wind power production. The onset of the FLLJ occurs at 0330 UTC on the 4th, with a consistent intensity of 16 m/s at all altitudes, although this intensity is lower than that in case 1. The FLLJ gradually strengthens, reaching its maximum at 0400 UTC on the 4th, with wind speeds at 50 m reaching 18 m/s and 200 m reaching 20 m/s.

All WRF simulations successfully captured the presence of the FLLJ, although they tend to overestimate its intensity. In the case of WRF-ERA5, the onset of intense winds exceeding 12 m/s commences at 0030 UTC on the 4th, delayed by 1 hour compared to the observation. Conversely, in the other simulations, winds surpassing 12 m/s initiate at the same observed time. Additionally, all simulations reproduced the onset of the FLLJ, exhibiting an intensity of 16 m/s at 0330 UTC, aligning with the observation. However, WRF-CERRA, WRF-CERRA*, and WRF-GFS notably overestimated the intensity, with winds at the 50 m level reaching as high as 18 m/s. Notably, among all simulations, WRF-CERRA+ closely replicated the observed FLLJ intensity at and below the 100 m level, albeit with a significant timing discrepancy. On the other hand, WRF-CERRA# showed an FLLJ for a prolonged duration, contrary to the observation. Despite these discrepancies, the WRF model effectively simulated the characteristics of the FLLJ.

Analyzing the ramp statistics, observed winds gradually diminished to 12 m/s by 0700 UTC on the 4th, followed by a rapid decrease to 6 m/s within 15 minutes, ultimately dropping to 4 m/s at 0730 UTC, indicating an intense wind ramp event coinciding with the frontal passage. After this event, wind conditions fluctuated within the range of 5-7 m/s. Among all WRF simulations, WRF-ERA5 simulated winds diminished gradually without displaying a distinct wind ramp. However, a mild ramp was observed around 0830 UTC, where wind speeds dropped from 13 m/s to 11 m/s, likely coinciding with the frontal passage. Nevertheless, the timing and intensity of this ramp did not closely match the observations. On the contrary, the ERA5 reanalysis does show a peculiar ramp during 0700-0800 UTC, which the WRF model seems failed to simulate. All CERRA simulations exhibited relatively similar ramp timing and intensity, reducing from 15 m/s at 0730 UTC to 10 m/s within 15 minutes. However, the ramp rate in WRF-CERRA# was comparatively less than in the other CERRA simulations.

This project has received funding from the Europeans Union's Horizon 2020 research & innovation programme under grant agreement number 101036457.

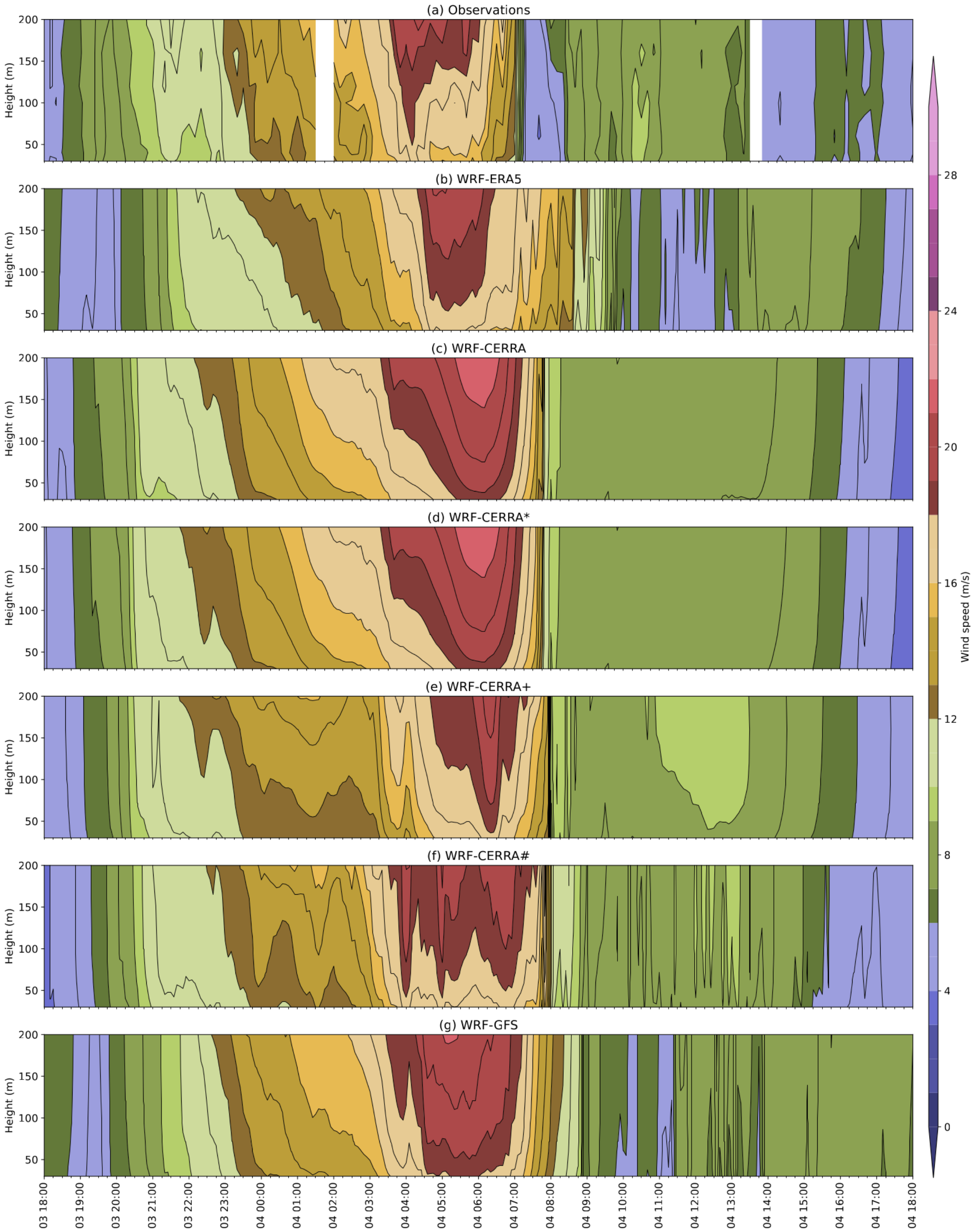

Figure 20: Time-height cross-sections of wind speed at the LOT1 location for Case 2, spanning from 1800 UTC on March 3rd to 1800 UTC on March 4th, 2016. The cross-sections include wind speed data obtained from various sources: (a) observational data, and WRF model simulations using different configurations, including (b) WRF-ERA5, (c) WRF-CERRA, (d) WRF-CERRA*, (e) WRF-CERRA+, (f) WRF-CERRA#, and (g) WRF-GFS.

Surprisingly, the CERRA reanalysis is seen to have a gradual wind drop during 0730-0830 UTC, but the WRF model was able to reproduce a strong and drastic wind ramp, comparable to that of the observation. Lastly, WRF-GFS simulation displayed a gradual decrease in wind speed, dropping to 10 m/s at 0845 UTC and further decreasing to 6 m/s within 15 minutes, resulting in a wind ramp event. Surprisingly, the ramp intensity surpassed that of the ERA5 simulation, comparable to the CERRA simulations, but with a significant timing error.

In the pursuit of identifying the most suitable model configuration for the current FLLJ and power ramp conditions, this study evaluates the Taylor skill scores for both wind speed and wind power using Equation 16, considering the combined impact of the two cases. For wind speed assessment, a comprehensive evaluation by aggregating data across all levels was conducted.

Equation 16

$$TSS = \frac{4(1+CC)^2}{(1+CC_0)^2\left(SDR+\frac{1}{SDR}\right)^2}$$

Here, CC is the correlation coefficient, CC_0 is the maximum correlation coefficient attainable (0.9999), and SDR is the standard deviation of the model normalized with the observed standard deviation. The central objective of our study is to demonstrate the superior predictive capabilities of the CERRA dataset compared to the widely adopted ERA5 dataset. To substantiate this claim, the TSS scores derived and compared from all simulations against those from the WRF-ERA5 reference, thereby quantifying the percentage improvement over WRF-ERA5. These comparative scores are presented in Table 8, providing a clear and concise overview.

Table 8: Taylor skill scores of wind power and wind speed obtained from the six WRF simulations. The percentage values indicate the improvement seen in TSS with respect to the WRF-ERA5 simulation.

Run	Wind Power	Wind Speed
WRF-ERA5	0.866	0.9254
WRF-CERRA	0.9541	0.9398
	-10.17%	-1.56%
WRF-CERRA*	0.928	0.9381
	-7.16%	-1.37%
WRF-CERRA+	0.9232	0.9434
	-6.60%	-1.94%
WRF-CERRA#	0.9227	0.9559
	-6.54%	-3.30%
WRF-GFS	0.9181	0.9243
	-6.02%	-0.1172%

A careful examination of the table reveals that the WRF simulations driven by CERRA data exhibit substantial enhancements in both wind speed and wind power predictions compared to those driven by ERA5 data. The utilization of the SH PBL scheme demonstrates notable improvements in wind speed, as evidenced by the results obtained with the WRF-CERRA+ and WRF-CERRA# configurations.

Employing a finer grid resolution of 0.5 km further enhances the accuracy of wind speed simulations. In conclusion, the WRF-CERRA# configuration achieves a noteworthy 3.3% improvement in wind speed simulations. When evaluating wind power, our results highlight the better predictability of the MYNN 2.5 scheme combined with the Fitch WFP, which showed an improvement of 10.17%. This observation underscores the pivotal role of wind farm parameterization in bolstering wind power predictions. Overall, our comprehensive analysis strongly advocates for the adoption of CERRA driving data, which offers a distinct advantage over ERA5 data in our study.

A marginal reduction in wind speed forecast accuracy is observed when utilizing the WRF-GFS configuration. However, it is crucial to note that this configuration yields a 6.54% improvement in wind power forecast accuracy, hinting at its potential for early detection of intense FLLJs and power ramp events. In conclusion, our findings emphasize the importance of data sources, PBL schemes, and wind farm parameterization in enhancing wind speed and wind power predictions and have significant implications for modelling FLLJs and associated extreme wind ramps.

2.4.4 Best set of physics schemes

Through this study, a final set of physics schemes and the model configuration is obtained, as illustrated in Table 9, which will be adopted for the full-scale simulations for the wind dataset generation.

Table 9: WRF model configuration and parameterization options obtained from the calibration study.

Horizontal resolution	0.5 km
Vertical levels	49
Terrain resolution	30 s
Initial and boundary conditions	CERRA 5.5 km and a temporal resolution of 3 hours
Radiation	RRTMG for shortwave and longwave
PBL physics	Shin-Hong
Surface layer physics	Revised MM5
Land surface physics	Unified NOAH
Microphysics	WRF single moment 5-class
Cumulus physics	Kain-Fritsch

This project has received funding from the Europeans Union's Horizon 2020 research & innovation programme under grant agreement number 101036457.

3 Solar Energy Resource Assessment

3.1 Limitations of Existing Solar Databases

Solar resource assessment is crucial for evaluating the potential of a site for solar energy generation. However, existing solar datasets, including ground-measured data, satellite data, and reanalysis data, come with inherent limitations that hinder accurate assessments.

Ground-measured data, considered the most reliable source, require expensive instruments, regular cleaning, and monitoring. However, these requirements often result in incomplete long-term time series at potential sites, limiting their utility for comprehensive assessments.

Satellite estimates of solar radiation are commonly used in the absence of ground-measured data, offering the advantage of long-term time series. However, satellite datasets are developed by various organizations and may not be globally available free of cost. Additionally, the accuracy of these datasets is uncertain, particularly in regions lacking ground measurements, leading to potential inaccuracies in solar resource assessments.

Reanalysis datasets, on the other hand, provide globally available data free of cost, covering long periods and offering data for locations or time steps where observations are not available. The global reanalysis datasets are developed by several organizations which include the Japan Meteorological Agency (JMA), the European Centre for Medium-Range Weather Forecasts (ECMWF), the National Aeronautics and Space Administration (NASA), the United States National Centers for Environmental Prediction (NCEP) and the United States National Center for Atmospheric Research (NCAR). The reanalysis dataset produced by JMA is the Japanese Reanalysis (JRA-25 and JRA-55), by ECMWF is the European Reanalysis (ERA-15, ERA-40, ERA-Interim and ERA-5) by NASA is Modern-Era Retrospective Analysis for Research and Applications (MERRA and MERRA-2), by NCEP is Climate Forecast System Reanalysis (CFSR), and by NCEP in collaboration with others are NCEP-NCAR, NCEP-DOE. The reanalysis datasets produced by these organizations have different versions and categories in different generations.

Despite these advantages, reanalysis data are subject to biases resulting from data assimilation methods and factors such as cloud cover and aerosols (Azhar M. a., 2020; Azhar M. a., 2020; Zhang, 2016). The reanalysis datasets often predict clear-sky conditions while actual conditions are cloudy-sky, the opposite is also true but less pronounced, actual clear-sky conditions are predicted as cloudy-sky (Azhar M. a., 2020). The reanalysis datasets have problems in the estimation of GHI for intermediate-sky and cloudy-sky conditions, the reanalysis datasets show overestimation and underestimation under different sky conditions.

To address these limitations and enhance the accuracy of solar resource assessments, we conducted simulations using the Weather Research and Forecasting (WRF) model at a resolution of 0.5 km. We incorporated the WRF-Solar module, which accounts for clouds and aerosols, allowing for more precise estimations of solar radiation. Furthermore, our dataset spans 31 years,

This project has received funding from the Europeans Union's Horizon 2020 research & innovation programme under grant agreement number 101036457.

emphasizing the importance of temporal scale in comprehensive solar resource assessments.

3.2 Solar model description (WRF-Solar EPS)

WRF-Solar® is the first numerical weather prediction model specifically designed to meet the growing demand for specialized numerical forecast products for solar energy applications (Jimenez P. A.-A., 2016). WRF-Solar is a specific configuration and augmentation of the WRF model.

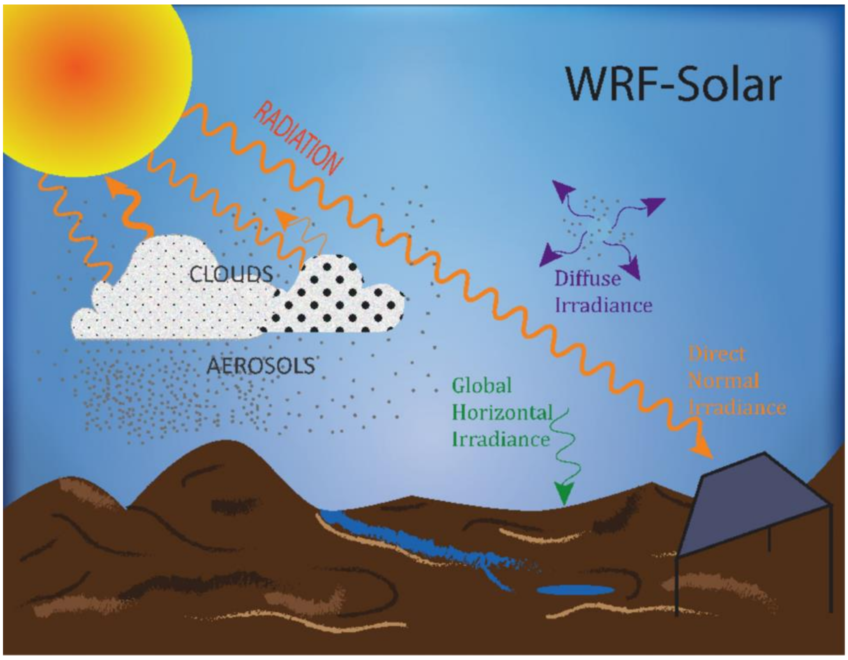

Figure 21: Sketch representing the physical processes that WRF-Solar® improves. The different components of the radiation are indicated. Source: https://ral.ucar.edu/solutions/products/wrf-solar

WRF-Solar added the direct normal irradiance (DNI) and diffuse (DIF) components from the radiation parameterization to the model output, which are not part of the conventional WRF model output. Several works highlighted the benefits of the solar augmentations for solar irradiance forecasting. WRF-Solar largely reduced errors in the simulation of clear sky irradiances wherein are important to properly account for the impacts of atmospheric aerosols (Jimenez P. A.-A., 2016). WRF-Solar have also been shown to reduce biases in the surface irradiance over the contiguous U.S. in all sky conditions (Jimenez P. A., 2016) In a formal comparison to the NAM baseline, WRF-Solar showed improvements in the Day-Ahead forecast of 22-42% (Haupt, 2016). Another work has pointed out the potential of WRF-Solar for nowcasting applications (Lee, 2016). The study compared solar irradiance predictions using different nowcasting methodologies based on artificial intelligence or the utilization of satellite imagery to detect clouds. The comparison has shown that WRF-Solar was competitive, and in many times superior to these state-of-the-science methodologies of the short-term prediction (1-6 h).

WRF-Solar® calculates the direct and diffuse surface irradiance. The direct and diffuse irradiance are calculated directly by RRTMG (sw_physics = 4) and Goddard (sw_physics = 5) shortwave radiation parameterizations. For the rest of the shortwave parameterizations WRF-Solar parameterizes the contributions of the direct and diffuse components. The direct normal irradiance (DNI) is stored in the SWDDNI variable and the diffuse in the SWDDIF variable. RRTMG also outputs the clear sky GHI and DNI on variables SWDOWNC and SWDDNIC, respectively. By default, these variables are not in the standard output. To add them to the standard output the user needs to add a h in the IO column in the rows of the registry file containing these variables.

To activate the effects of unresolved clouds on shortwave radiation, set shcu_physics = 5. The Cu parameterization should be turned off since the WRF-Solar shallow cumulus scheme also accounts for deep convection. This option only works with two planetary boundary layer parameterizations, bl_pbl_physics = 2 or 5. The option 5 is recommended.

By setting swint_opt = 2 the Fast All-sky Radiation Model for Solar applications (FARMS) scheme is activated. FARMS calculates the surface irradiance every model time step and stores the values in SWDOWN2, SWDDNI2 and SWDDIF2 variables. It also provides clear sky irradiances (SWDOWNC2 and SWDDNIC2). This option uses the current atmospheric state, including hydrometeors, to calculate the surface irradiance and it is the recommended one.

WRF-Solar includes a solar diagnostic package (solar_diagnostic = 1). This option adds to the standard output a number of two-dimensional variables (e.g., cloud fraction, vertically integrated hydrometeor content, clearness index, etc). A complete list of the variables can be found in the README.tslist file in the run directory. If the tslist option is activated, the solar diagnostic package outputs these variables and the surface irradiances every model time step at selected locations. This requires an ascii file with the latitude and longitude of the sites to output the time series (see README.tslist file in the run directory).

4 Gray-zone resolution wind and solar dataset (SWaGZ) generation and validation

For the generation of super-scale resolution wind and solar datasets, we used the WRF model V4.4. To account for the betterment in solar statistics, we included the WRF-Solar EPS in numerical simulations. The global aim of the work is to generate hindcasts at 0.5 km resolution for 31 years, over three locations: Iberia, Ireland, and BeNeLux. The locations of interest (as per the project requirement) are presented in Figures 22, 23, and 24, for Iberia, Ireland, and BeNelux, respectively.

This project has received funding from the Europeans Union's Horizon 2020 research & innovation programme under grant agreement number 101036457.

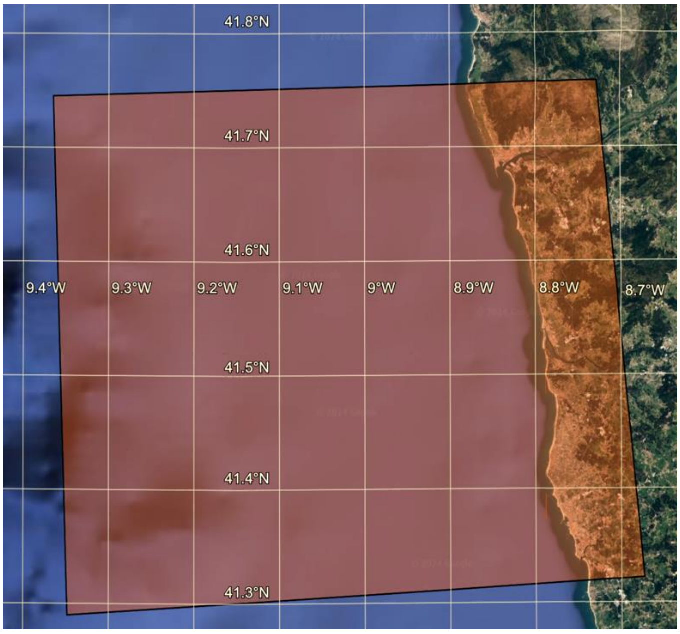

Figure 22: Iberia location (according to the project requirement), for the generation of 30 years super-scale resolution wind and solar hindcasts.

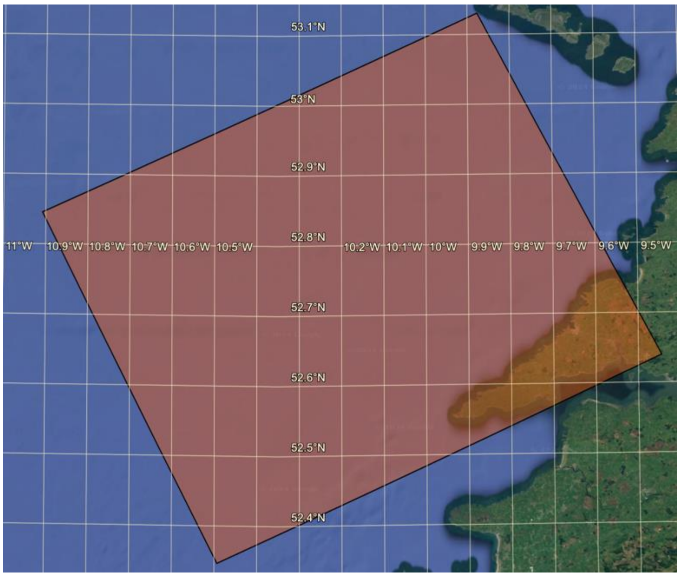

Figure 23: Ireland location (according to the project requirement), for the generation of 30 years super-scale resolution wind and solar hindcasts.

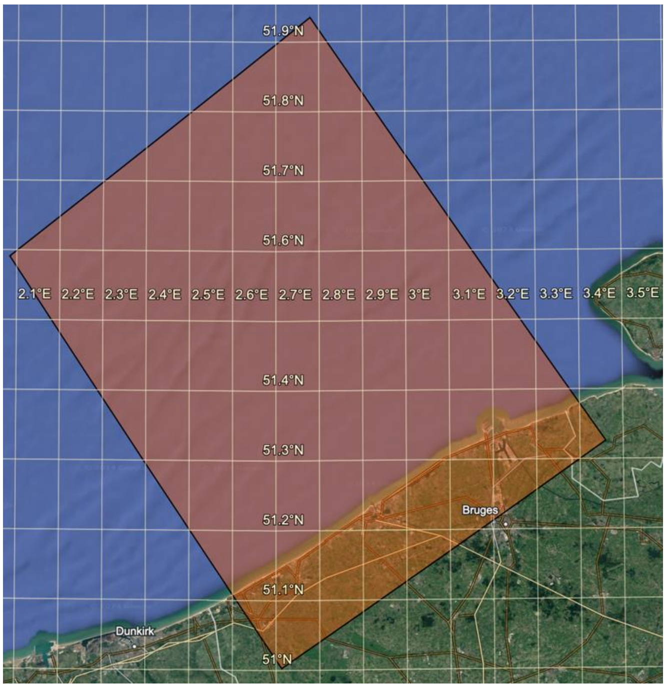

Figure 24: BeNeLux location (according to the project requirement), for the generation of 30 years super-scale resolution wind and solar hindcasts.

Based on these regions of interest, we tried to configure the WRF model domains as suitable as possible. The WRF model simulations are conducted individually at the three locations and generated the hindcasts for 30 years.

Based on the physics schemes calibration, we adopted the Shin-Hong scheme for planetary boundary layer parameterization, without windfarm parameterization, which is shown to perform better at the 0.5 km resolution. The remaining physics schemes and the domain configuration levels are presented in Table 10.

Table 10: WRF model configuration and parameterization options.

Horizontal resolution	0.5 km
Vertical levels	49
Terrain resolution	30 s
Initial and boundary conditions	CERRA 5.5 km and a temporal resolution of 3 hours
Radiation	RRTMG for shortwave and longwave
PBL physics	Shin-Hong
Surface layer physics	Revised MM5
Land surface physics	Unified NOAH
Microphysics	WRF single moment 5-class
Cumulus physics	Kain-Fritsch

A total of 31 years (1990-2021) of numerical simulations are conducted using the SCORES domain configuration, such that the simulations are reinitialized at 0000 UTC every 5 days and run for 6 days. After excluding the first 24-h spin-up time, the simulated outputs from the 5-day periods are considered for analysis. For our framework, 2265 runs are performed to cover the entire 31-year period.

The following sections give detailed of data generation and validation at the respective locations.

4.1 Iberia

4.1.1 WRF model domain configuration

The WRF model is configured with single domain, of 0.5 km resolution. Figure 25(a) illustrates the WRF model domain configuration adopted for the numerical simulations of 31 years hindcasts, which is termed as SCORES domain here after. The SCORES domain consists of 128*128 grid points in the latitude and longitudinal directions. In the absence of observational data within the specified SCORES domain, a critical component of our study involves the validation of model simulations through the utilization of an Extended domain. This larger domain encompasses not only the SCORES domain but also incorporates additional observational sites, as shown in Figure 25(b). The Extended domain consists of 168 grid points in longitude direction and 240 grid points in latitude direction. To assess the accuracy of our model outputs, we performed a comprehensive set of simulations spanning a duration of 1 year (2011-07-01 to 2012-07-01) using this Extended domain. These experiments also follow a similar strategy adopted for the SCORES domain simulations. By extending the geographical coverage to include areas with available observational data, we aim to enhance the robustness and reliability of our model's simulation capabilities.

This project has received funding from the Europeans Union's Horizon 2020 research & innovation programme under grant agreement number 101036457.

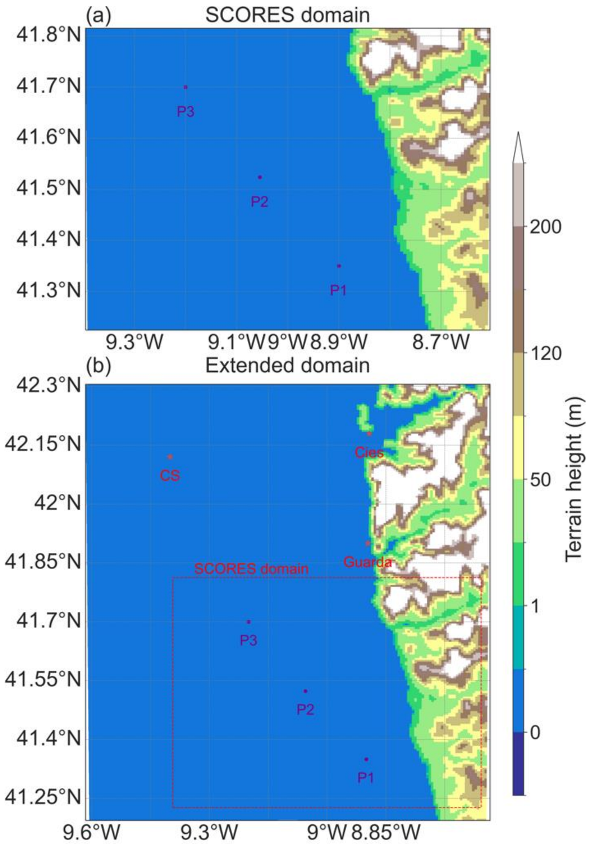

Figure 25: WRF model domain configurations: (a) SCORES domain for 30-year hindcast simulations (1990-01-01 to 2020-01-01), consisting of 128*128 grid points; (b) Extended domain for 1-year validation simulations (2011-07-01 to 2012-07-01), consisting of 168*240 grid points. Three coastal buoys are shown with stars in (b), and purple locations (P1-P3) are used for intermodel comparison and resource assessment.

4.1.2 Observational data

Observations used for the model validation were collected from three coastal marine buoys, namely Guarda, Cies, and Cabo Silleiro (CS). Table 11 provides important information about the buoys, while the locations of these buoys are illustrated in Figure 25. Wind and surface air temperature measurements taken from the 1st of July 2021 to the 1st of July 2012 (1 year) were selected, and the choice of this period was related to measured data availability and quality criteria.

Table 11: Some important features of the marine buoys used in Portugal simulation validation.

Name	**Location**	**Distance to shore**	**Height (m)**	**Sampling rate (min)**	**Programme**	**Period**	**WMO number**
Guarda	41.9°N, 8.896°W	1.5 km	4.5	60	Xunta de Galicia	29-07-2010 to 30-09-2022	6201031
Cies	42.179°N, 8.892°W	1.2 km	4.5	60	Xunta de Galicia	04-04-2008 to 30-09-2022	6201040
Cabo Silleiro	42.12°N, 9.4°W	40 km	3	60	Puertos del Estado	06-07-1998 to Present	6200084

The buoys considered for our framework collect measurements at 3-4.5m above sea level (asl), necessitating extrapolation to near surface ocean wind level, typically

This project has received funding from the Europeans Union's Horizon 2020 research & innovation programme under grant agreement number 101036457.

10m asl. Traditional methods like the Monin–Obukhov theory require additional data (friction velocity, temperature, heat fluxes), which are unavailable from these buoys. In the absence of essential data, a simplified logarithmic wind profile expression as follows is adopted for extrapolation from buoy height to 10 m asl (Carvalho, 2017; Remmers, 2019).

Equation 17

$$U_Z = U_{Z_m}\frac{ln\left(\frac{Z}{Z_0}\right)}{ln\left(\frac{Z_m}{Z_0}\right)}$$

Here, U_Z refres to the wind speed at a height Z, Z_m is the measurement height (3m asl), and Z_0 is the local roughness length. A roughness length of 0.0002m is appropriate for ocean surface, and the same has been adopted for our framework (Carvalho, 2017; Remmers, 2019).

Apart from the observations, the reanalysis dataset, namely ERA5 is also used for the model validation. Published in 2019, ERA5 is the 5th generation European Centre for Medium-Range Weather Forecasts (ECMWF) reanalysis dataset, stands as the most recent iteration among the ECMWF global reanalysis products. It delivers 1-hour estimates for various variables, with a spatial resolution of approximately 31 km (0.25° × 0.25°) and covers 137 vertical levels up to 0.01 hPa. The dataset spans from 1950 to the present, offering comprehensive information that includes wind speed, not only at the standard 10 m level seen in its predecessors but also at the elevated 100 m level.

4.1.3 Model evaluation metrics

To assess the degree of agreement between the simulations and observations, several statistical metrics are used. The Root Mean Square Error (RMSE) quantifies the square root of the average squared differences between model predictions and corresponding observations, providing insight into the magnitude of errors. Pearson's Correlation Coefficient (r) assesses the linear relationship between model and observed values. The Scatter Index (SI) normalizes model performance against the scale of observed data by comparing RMSE to the mean observed value. Lastly, the Mean Absolute Error (MAE) provides an average of absolute differences between model and observed values, offering a straightforward measure of accuracy.

Equation 18

$$RMSE = \sqrt{\frac{1}{n}\sum_1^n (S_i - M_i)^2}$$

Equation 19

$$r = \frac{\sum_1^n (M_i - \bar{M})(S_i - \bar{S})}{\sqrt{\sum_1^n (M_i - \bar{M})^2 \sum_1^n (S_i - \bar{S})^2}}$$

Equation 20

$$bias = \frac{1}{n}(S_i - M_i)$$

Equation 21

$$SI = \frac{RMSE}{\bar{M}}$$

Equation 22

$$MAE = \frac{1}{n}|S_i - M_i|$$

Here, M_i represents for model predictions, S_i represents observed or reference data, $\bar{M}$ and $\bar{S}$ represent mean values, and n representing the number of data points in the dataset.

These traditional metrics provide valuable insights into model accuracy, but may overlook the significance of subtle changes in the shape of the wind speed distribution. In wind energy applications, where wind power density is proportional to the cube of wind speed, small variations in the distribution can have a pronounced impact on power generation. To address this limitation, the Earth Mover's Distance (EMD) (Rubner, 2000) is introduced as a metric that evaluates differences in the shape of frequency distributions, which has been referred to as various names: transportation distance, Kantorovich metric, Vasershtein metric, Hutchinson metric, etc. The EMD can be interpreted as the amount of physical work needed to move a pile of soil in the shape of one distribution to that of another distribution, making it particularly relevant for applications where the shape of the distribution is crucial, such as wind resource assessments and estimates in power production (Hahmann, 2020). The EMD, calculated using the python scipy stats package, offers a more nuanced perspective on distribution dissimilarity, providing valuable insights for wind energy assessments and other applications.

Apart from these quantitative measures, several other comparison techniques used in qualitative evaluation. Bivariate histograms of wind speed provide joint distribution of two continuous variables and illustrate the frequency of occurrence of binned wind. Wind rose, another graphical tool provide concise and insightful representation of wind direction and their frequency, on a polar chart. Finally, the probability distribution of wind speed are represented through histograms and their corresponding Weibull distributions.

4.1.4 Wind dataset validation

Figure 26 illustrates bivariate histograms of 10m wind speeds from ERA5 and WRF_{Ext} simulations at the Guarda buoy site, compared with observations. The ERA5 dataset appears to largely underestimate wind speeds at this location, as evident from the significant biases observed. Furthermore, the ERA5 data show a limitation in reproducing winds exceeding 13 m/s near coastal boundaries, while observed winds reach up to 20 m/s. In contrast, bivariate histograms of wind speeds from WRF_{Ext} simulations are performing better by reducing the bias.

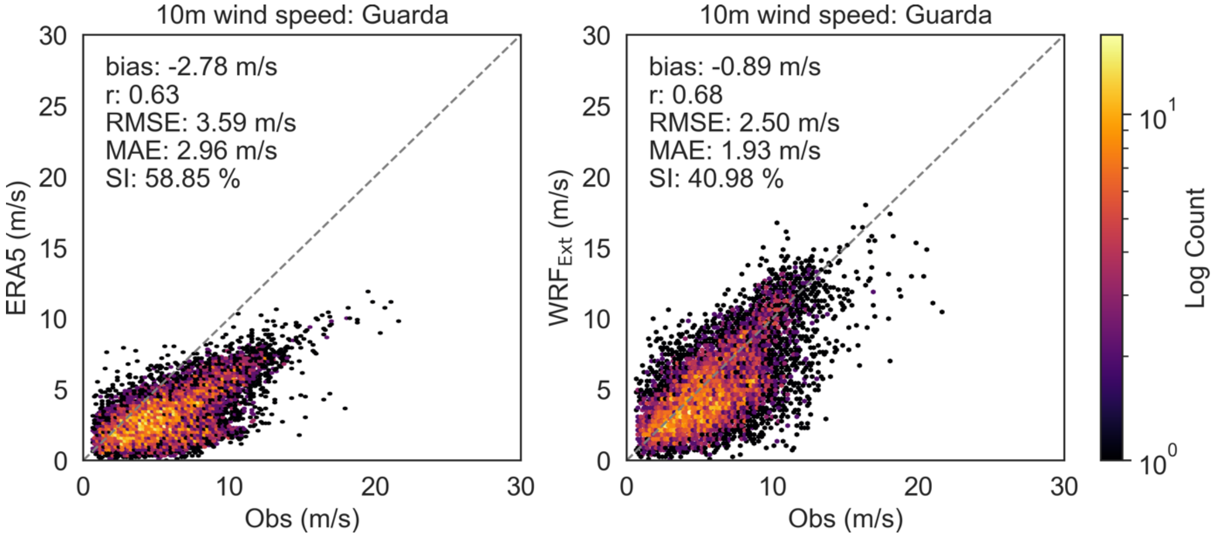

Figure 26: Bivariate histograms depicting the 10m wind speed distribution from ERA5 (1st column and WRF_{Ext} simulations (2nd column), compared with the buoy observations: Gaurda. The number of occurrences is presented in log count, with darker (lighter) color indicating low

This project has received funding from the Europeans Union's Horizon 2020 research & innovation programme under grant agreement number 101036457.

(high) occurrence. The evaluation statistics including bias, RMSE, Pearson's correlation (r), mean absolute error (MAE), and the Scatter Index (SI) are computed to assess the agreement between the three datasets and observational data. The data spans a collection period from 01-07-2011 to 01-07-2022, covering a year-long duration.

Figure 27 illustrates the 10m wind speed distributions from the ERA5 and $\mathrm{WRF}_{\mathrm{Ext}}$ datasets in comparison with buoy observations at the Guarda location. The observed distribution extends over a considerable range, centered around a mode of 5 m/s. ERA5 exhibits a skewed distribution centered around a mode of 3 m/s. The ERA5 significantly underestimates wind speed frequencies beyond 7 m/s, while overestimating frequencies around 3 m/s. These findings align with the large negative biases estimated earlier. The simulations from $\mathrm{WRF}_{\mathrm{Ext}}$ underestimate high wind speed frequencies and overestimate low wind speed frequencies, slightly aligning better with the observed one. This alignment is consistent with the negative biases observed earlier.

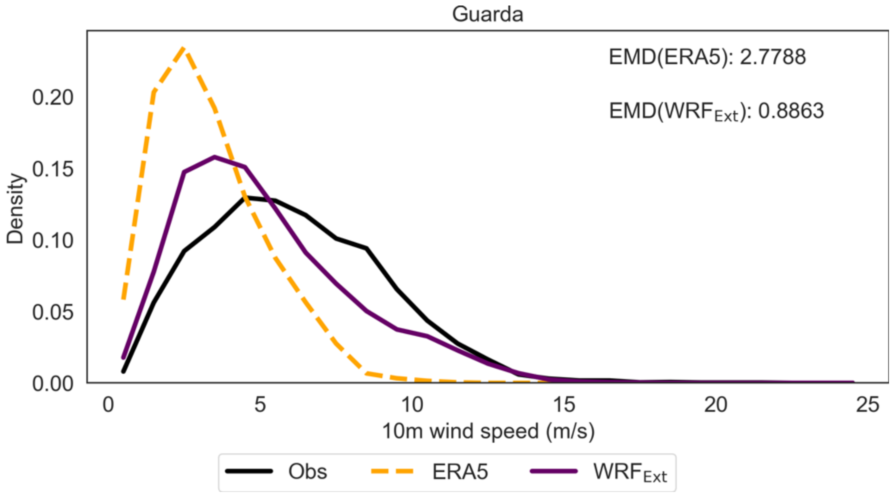

Figure 27: Comparison of 10m wind speed distributions from ERA5 $\mathrm{WRF}_{\mathrm{Ext}}$ datasets, with respect to the buoy observations, at location Guarda. The Earth Movers Distance (EMD) is calculated and shown, assessing dissimilarities between the datasets and observational data.

Figure 28 illustrates bivariate histograms of 10m wind speeds from ERA5 and $\mathrm{WRF}_{\mathrm{Ext}}$ simulations at the CS buoy site, compared with observations. This observational cite is located far offshore, thus away from any land interactions. At this cite, both the ERA5 and $\mathrm{WRF}_{\mathrm{Ext}}$ are performing better, with the latter reducing the bias.

This project has received funding from the Europeans Union's Horizon 2020 research & innovation programme under grant agreement number 101036457.

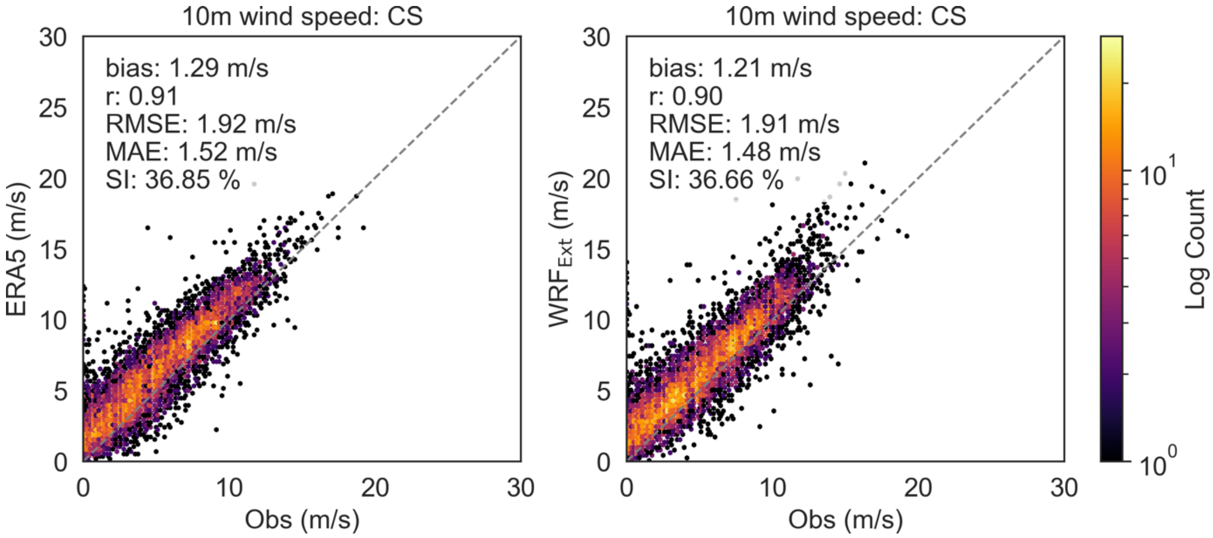

Figure 28: Same as Figure 26, but at the CS buoy location.

Figure 29 illustrates the 10m wind speed distributions from the ERA5 and WRF$_{Ext}$ datasets in comparison with buoy observations at the CS location. The observations reveal a wider distribution with two peaks, one at 3 m/s and another at 7 m/s. The distributions from ERA5, and WRF$_{Ext}$ also exhibit bimodal peaks and consistently shift to the right of the observed one, implying an overestimation of all wind speed frequencies. Notably, the WRF$_{Ext}$ distribution is slightly closer to the observed one during high wind speeds, leading to the reduction in wind speed bias, as observed earlier. At this location, the WRF$_{Ext}$ distribution has the least EMD value, indicating better agreement of the WRF simulations with observations.

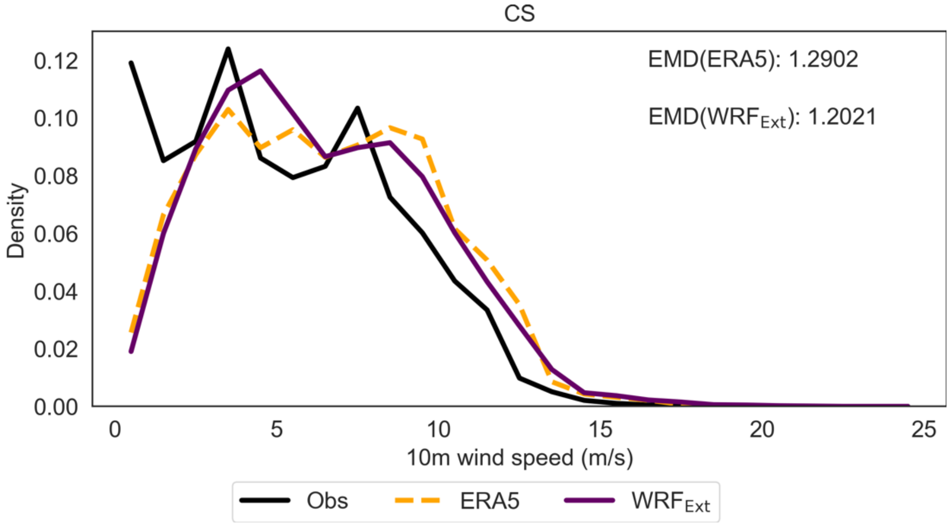

Figure 29: Same as Figure 27, but at the CS location.

Figure 30 illustrates bivariate histograms of 10m wind speeds from ERA5 and WRF$_{Ext}$ simulations at the Cies buoy site, compared with observations. The ERA5 dataset appears to largely underestimate wind speeds at this location, as evident from the significant biases observed. Furthermore, the ERA5 data show a limitation

This project has received funding from the Europeans Union's Horizon 2020 research & innovation programme under grant agreement number 101036457.

in reproducing winds exceeding 13 m/s near coastal boundaries, while observed winds reach up to 20 m/s. In contrast, bivariate histograms of wind speeds from WRF_{Ext} simulations are performing better by reducing the bias. Though the Pearson's correlation is same for ERA5 and WRF_{Ext}, the latter have least RMSE, MAE, and SI scores.

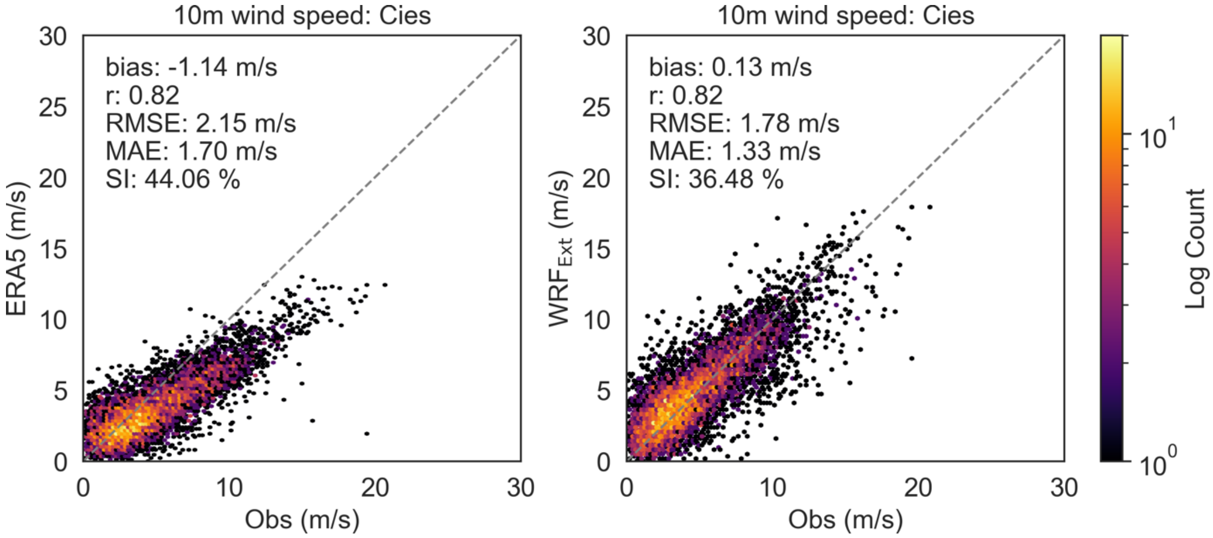

Figure 30: Same as Figure 26, but at the Cies buoy cite.

Figure 31 illustrates the 10m wind speed distributions from the ERA5 and WRF_{Ext} datasets in comparison with buoy observations at the Cies location. The observed distribution extends over a considerable range, centered around a mode of 3 m/s. ERA5 exhibits a skewed distribution centered around a mode of 3 m/s. The ERA5 significantly underestimates wind speed frequencies beyond 7 m/s, while overestimating frequencies around 3 m/s. On the contrary, the simulations from WRF_{Ext} slightly underestimate high wind speed frequencies and marginally overestimate low wind speed frequencies, closely aligning better with the observed one. This alignment is consistent with the metrics observed earlier.

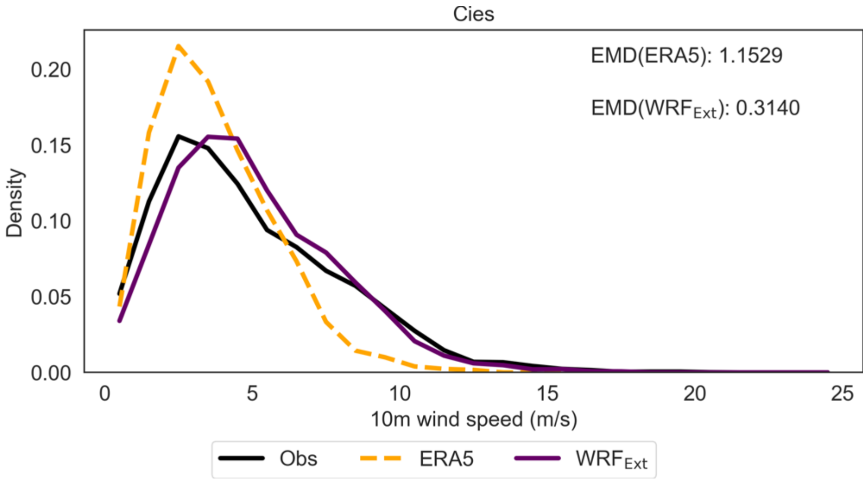

Figure 31: Same as Figure 27, but at the Cies location.

This project has received funding from the Europeans Union's Horizon 2020 research & innovation programme under grant agreement number 101036457.

So far, we've assessed the accuracy of the WRF$_{\text{Ext}}$ simulations, covering the observational period from 01-01-2011 to 01-01-2012. However, our primary focus is on evaluating the 31-year wind resources from 01-01-1990 to 01-01-2021 using the SCORES domain. To do this, we must now analyze the accuracy of WRF$_{\text{SCORES}}$ simulations. Given the observed better agreement with WRF$_{\text{Ext}}$ seen earlier, we utilize WRF$_{\text{Ext}}$ simulations as a reference to evaluate the accuracy of WRF$_{\text{SCORES}}$ simulations. In doing so, we compared wind speed at three heights (100m, 120m, and 150m), extracted at three sample points P1, P2, and P3, from both the domains (which are illustrated in Figure 25), spanning for a period of 1 year from 01-07-2011 to 01-07-2012, and the results are illustrated in Figures 32, 33, and 34.

The bivariate histograms shows that the clearly show that the wind speeds are perfectly aligning along the q-q line, with a Pearson's correlation coefficient ranging between 0.96 and 0.98, implying a better agreement between the two datasets. Upon a close inspection, it is observed that the histograms have thinner spread at the sample points P1 and P2, while the spread is little higher at point P3. The same is quantified through the scatter index, which is seen to be around 15% at P1 and P2, while around 20% at P3. These deviations lead to the marginal differences seen in terms of RMSE, MAE, and EMD.

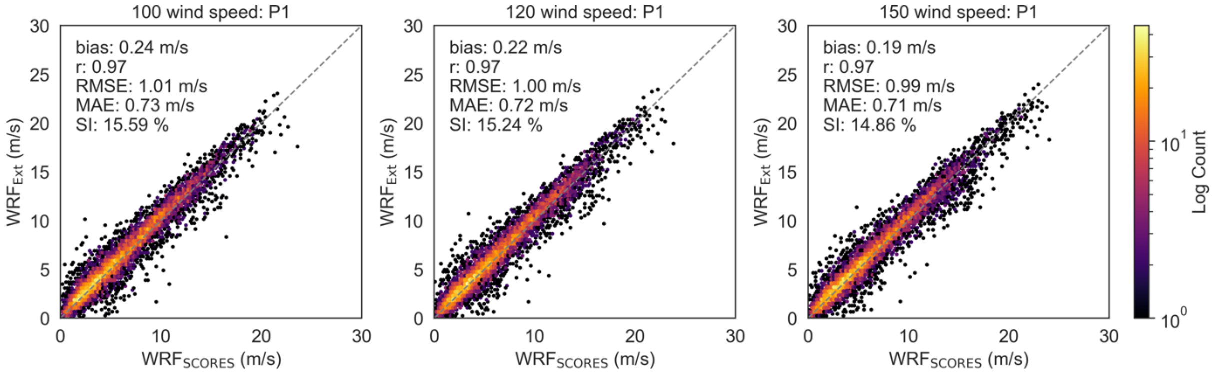

Figure 32: Bivariate histograms depicting the 100m (column 1), 120m (column 2), and 150m (column 3) wind speed distributions from WRF$_{\text{SCORES}}$ and WRF$_{\text{Ext}}$ simulations, at point P1, during the period from 01-07-2011 to 01-07-2012, covering a year-long duration. The evaluation statistics (RMSE, r, MAE, and SI) are computed to assess the agreement between the two datasets.

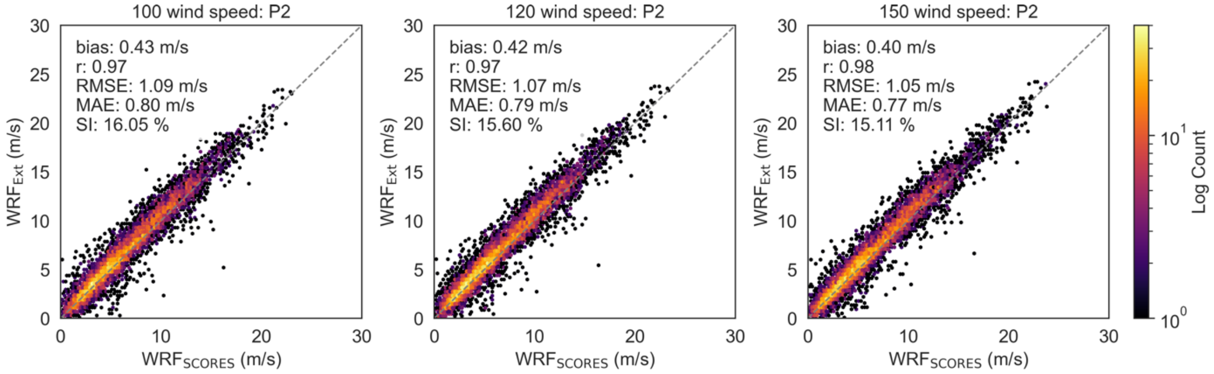

Figure 33: Same as Figure 32, but at point P2.

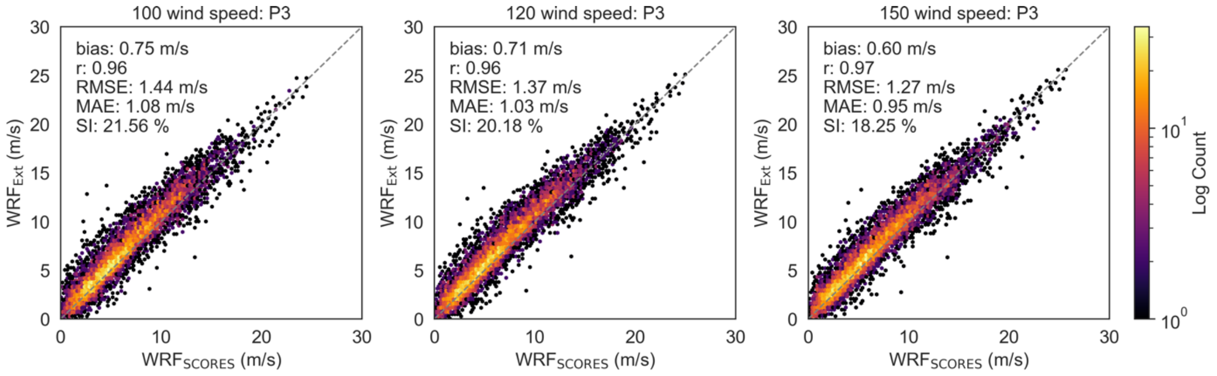

Figure 34: Same as Figure 32, but at point P3.

From these model evaluation, it is evident that the WRF$_{SCORES}$ simulations having superior performance than ERA5, and are well comparable with the observations, in wind resources.

4.1.5 Temperature validation

Similar to the wind data validation, the temperature validation is also conducted at the three observational cites. Figure 35 illustrates the bivariate histograms of 2m temperature, from ERA5 and WRF$_{Ext}$, compared with the buoy observation at the Guarda cite. From this, it is clearly evident that the ERA5 overestimates surface air temperature, with a positive bias of 0.81 °C, whereas the WRF$_{Ext}$ simulated surface air temperature closely follows observations, with minimum bias of 0.22 °C. In addition, the Pearson's correlation is also 0.94 for WRF$_{Ext}$, indicating a better simulation capability.

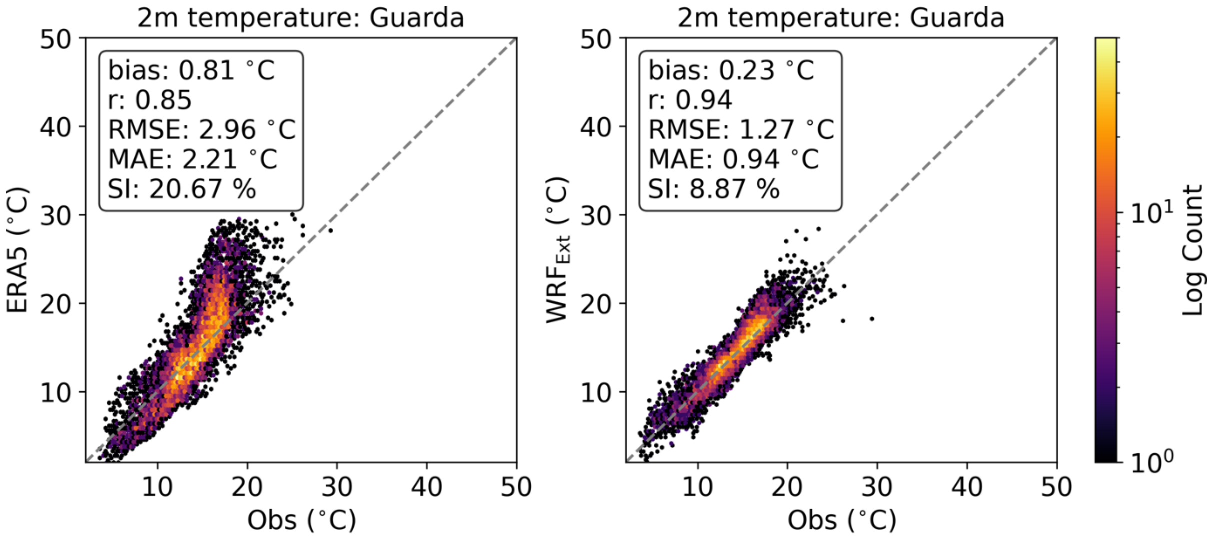

Figure 35: Bivariate histograms depicting the 2m temperature distribution from ERA5 (1st column and WRF$_{Ext}$ simulations (2nd column), compared with the buoy observation Gaurda. The number of occurrences is presented in log count, with darker (lighter) color indicating low (high) occurrence. The evaluation statistics including bias, RMSE, Pearson's correlation (r), mean absolute error (MAE), and the Scatter Index (SI) are computed to assess the agreement between the three datasets and observational data. The data spans a collection period from 01-07-2011 to 01-07-2022, covering a year-long duration.

Figure 36 illustrates the 2m temperature distributions from the ERA5 and WRF_{Ext} datasets in comparison with buoy observations at the Guarda location. The observations reveal a wider distribution with two peaks, one at 12 °C and another at 16 °C. The distributions from WRF_{Ext} also exhibit bimodal peaks and consistently shift to the right of the observed one, implying a marginal overestimation of all temperature frequencies. Notably, the WRF_{Ext} distribution perfectly closer to the observed one during low and high temperatures, leading to the reduction in temperature bias, as observed earlier. In contrast, the ERA5 temperature does not show bimodal peaks, and greatly underestimates low temperature frequencies and overestimates high temperature frequencies. At this location, the WRF_{Ext} distribution has the least EMD value, indicating better agreement of the WRF simulations with observations.

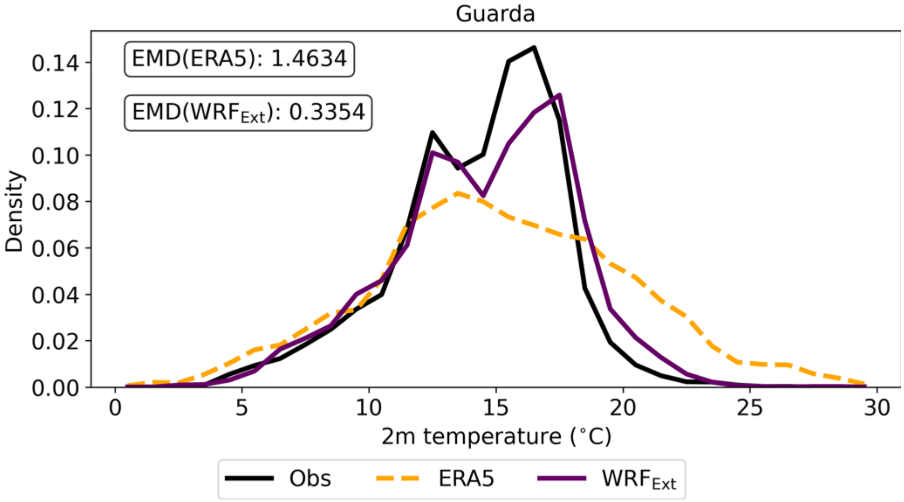

Figure 36: Comparison of 2m temperature distributions from ERA5 WRF_{Ext} datasets, with respect to the buoy observations, at location Guarda. The Earth Movers Distance (EMD) is calculated and shown, assessing dissimilarities between the datasets and observational data.

Figure 37 and Figure 38 illustrate the bivariate histograms and distributions of 2m temperature, from ERA5 and WRF_{Ext}, compared with the CS buoy observation. From these figures, it is clearly evident that the ERA5 and WRF_{Ext} perfectly captured observed surface air temperature, with a negligible biases. In addition, the Pearson's correlation is also 0.97 for both datasets, indicating a better simulation capability. The observations reveal a wider distribution with two peaks, one at 12 °C and another at 16 °C. The distributions from ERA5 and WRF_{Ext} also exhibit bimodal peaks. Notably, the WRF_{Ext} distribution perfectly closer to the observed one during low and high temperatures, leading to the reduction in temperature bias, as observed earlier. In contrast, the ERA5 distribution shows marginal underestimation of medium temperature frequencies.

This project has received funding from the Europeans Union's Horizon 2020 research & innovation programme under grant agreement number 101036457.

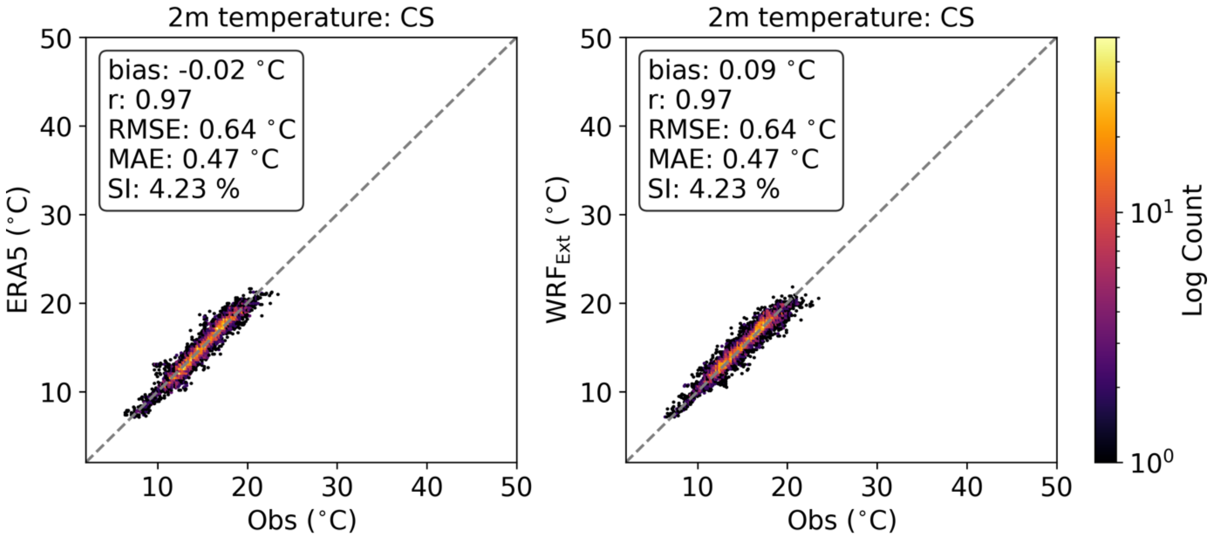

Figure 37: Same as Figure 35, but for buoy location CS.

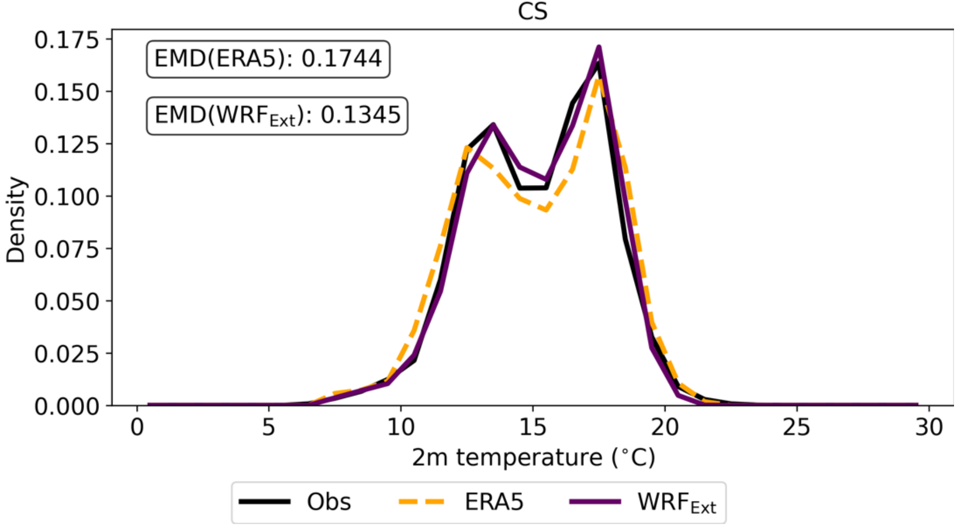

Figure 38: Same as Figure 36, but for buoy location CS.

Figure 39 illustrates the bivariate histograms of 2m temperature, from ERA5 and WRF$_{Ext}$, compared with the Cies buoy observation. Here, the WRF$_{Ext}$ show remarkable similarity to that of the observations, with a Pearson's correlation of 0.95, and a scatter index of 6.66%, indicating a better simulation capability. On the other hand, the ERA5 overestimates surface air temperature, however the bias is seem to be lesser than the WRF$_{Ext}$.

This project has received funding from the Europeans Union's Horizon 2020 research & innovation programme under grant agreement number 101036457.

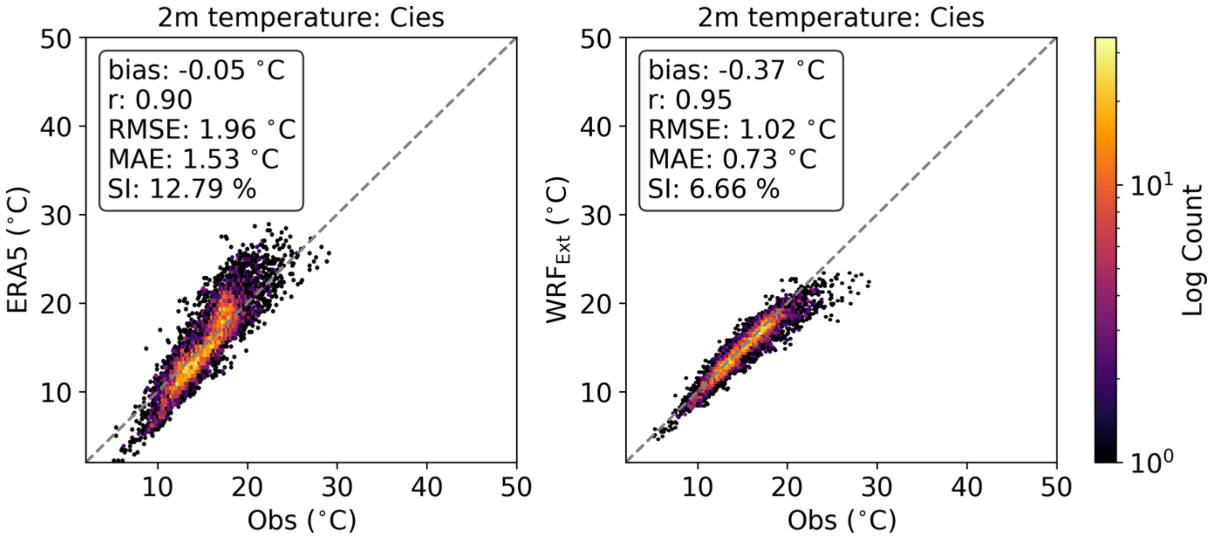

Figure 39: Same as Figure 35, but for buoy location Cies.

Figure 40 illustrates the 2m temperature distributions from the ERA5 and WRF_{Ext} datasets in comparison with buoy observations at the Cies location. The observations reveal a wider distribution with two peaks, one at 12 °C and another at 17 °C. The distributions from WRF_{Ext} also exhibit bimodal peaks, while the ERA5 show a weak secondary distribution at 19 °C. Notably, the WRF_{Ext} distribution perfectly closer to the observed one during low and high temperatures, leading to the reduction in temperature bias, as observed earlier. In contrast, the ERA5 temperature does not show bimodal peaks, and greatly underestimates medium temperature frequencies and overestimates high temperature frequencies. At this location, the WRF_{Ext} distribution has the least EMD value, indicating better agreement of the WRF simulations with observations.

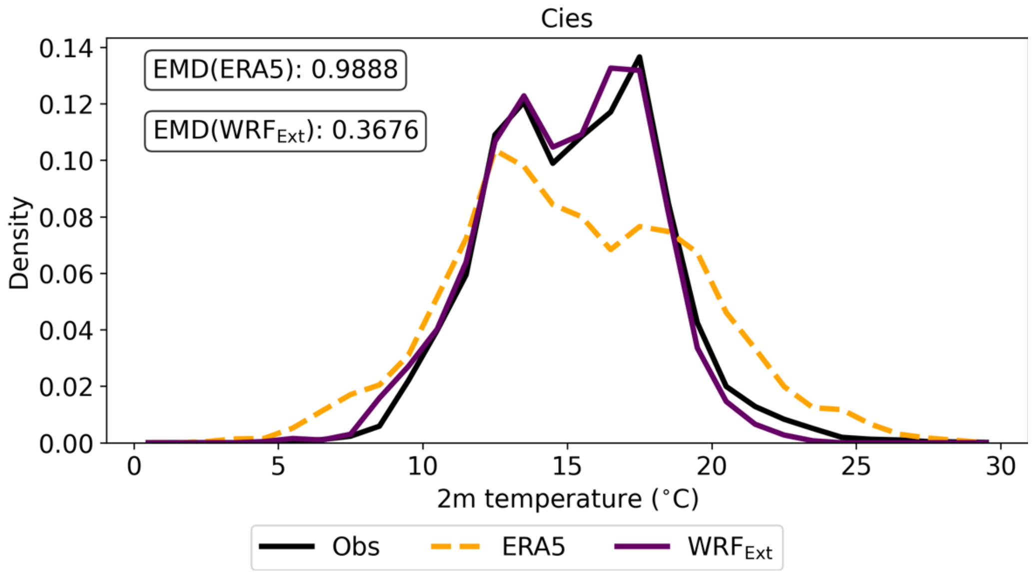

Figure 40: Same as Figure 36, but for buoy location Cies.

This project has received funding from the Europeans Union's Horizon 2020 research & innovation programme under grant agreement number 101036457.

These comparisons strengthen the better simulation capability of the WRF in generating wind and solar datasets. So far, we've assessed the accuracy of the $\mathrm{WRF}_{\mathrm{Ext}}$ simulations, covering the observational period from 01-01-2011 to 01-01-2012. Same as we did for wind validation, we have to evaluate the 31-year solar resources from 01-01-1990 to 01-01-2021 using the SCORES domain. Given the observed better agreement with $\mathrm{WRF}_{\mathrm{Ext}}$ seen earlier, we utilize $\mathrm{WRF}_{\mathrm{Ext}}$ simulations as a reference to evaluate the accuracy of $\mathrm{WRF}_{\mathrm{SCORES}}$ simulations. In doing so, we compared 2m temperature, extracted at three sample points P1, P2, and P3, from both the domains (which are illustrated in Figure 25), spanning for a period of 1 year from 01-07-2011 to 01-07-2012, and the results are illustrated in Figure 41.

The bivariate histograms clearly show that the temperatures are perfectly aligning along the q-q line, with a Pearson's correlation coefficient 0.99, implying a better agreement between the two datasets. In addition, the other evaluation metrics also show negligible deviations from one another, indicating that the SCORES domain simulations are indeed similar to that of the Extended domain simulations.

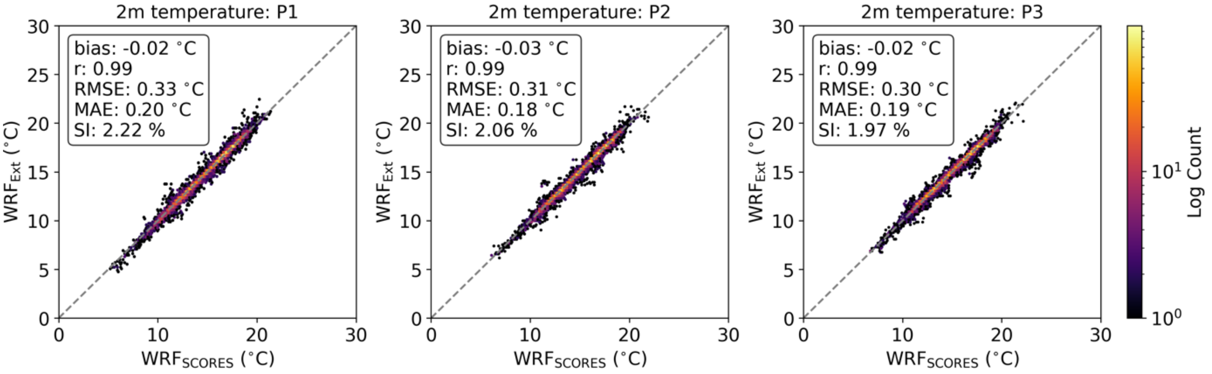

Figure 41: Bivariate histograms depicting the 2m temperature distributions from $\mathrm{WRF}_{\mathrm{SCORES}}$ and $\mathrm{WRF}_{\mathrm{Ext}}$ simulations, at point P1 (1st column), P2 (2nd column), and P3 (3rd column), during the period from 01-07-2011 to 01-07-2012, covering a year-long duration. The evaluation statistics (RMSE, r, MAE, SI, and the EMD) are computed to assess the agreement between the two datasets.

4.1.6 Overview of the utilized computational facilities

The WRF model simulations are carried out on the DelftBlue High Performance Computing Centre (DHPC) (https://doc.dhpc.tudelft.nl/delftblue/). Table 12 illustrates the details of computational facilities utilized for a single WRF model run, with the Extended domain configuration for the validation simulations and SCORES configuration for the 31-year simulations, over the Portugal coast. As mentioned earlier, a single WRF model run is simulated for 6 days, in which the first day of simulation is discarded as spin-up and the remaining five days of simulations are considered as useful. Through this design, a total of 74 runs are performed for validation simulations (covering 1 year period), while a total of 2265 runs are performed for the SCORES simulations (covering 31-year period). Based on the statistics provided, a total of 78,144 CPU hours were utilized for the validation simulations (74 runs), while a total of 8,15,400 CPU hours were utilized for the SCORES simulations (2265 runs), excluding the queue time. To give an idea about the actual time taken for the simulations, divide the CPU hours by the number of

CPUs since they run in parallel, which will give 4884 hours for the validation simulations and 1,01,925 hours for the SCORES simulations, excluding the queue time and analysis time. Technically, the whopping amount of time required for the data generation is impossible. The work was only possible with a strategic simulation design and execution to submit multiple jobs in parallel.

Table 12: Details of computational facilities utilized for a single WRF model run over the Portugal coast

	WRF_{Ext} simulations	**WRF_{SCORES} simulations**
Grid size	164*240	128*128
Simulation Duration (h)	144	144
Nodes	1	1
Cores per node	16	8
Total CPU hours	1056	360
Storage accumulation (GB)	14	9

4.2 Ireland

4.2.1 WRF model domain configuration

The WRF model is configured with single domain, of 0.5 km resolution. Figure 42(a) illustrates the WRF model domain configuration adopted for the numerical simulations of 31 years hindcasts, which is termed as SCORES domain here after. The SCORES domain consists of 128*128 grid points in the latitude and longitudinal directions. In the absence of observational data within the specified SCORES domain, a critical component of our study involves the validation of model simulations through the utilization of an Extended domain. This larger domain partially intersects with the SCORES domain while covering a single buoy observational cite, as shown in Figure 42(b). The Extended domain consists of 200 grid points in longitude direction and 200 grid points in latitude direction. To assess the accuracy of our model outputs, we performed a comprehensive set of simulations spanning a duration of 1 year (2003-03-01 to 2004-03-01) using this Extended domain. These experiments also follow a similar strategy adopted for the SCORES domain simulations. By extending the geographical coverage to include areas with available observational data, we aim to enhance the robustness and reliability of our model's simulation capabilities.

This project has received funding from the Europeans Union's Horizon 2020 research & innovation programme under grant agreement number 101036457.

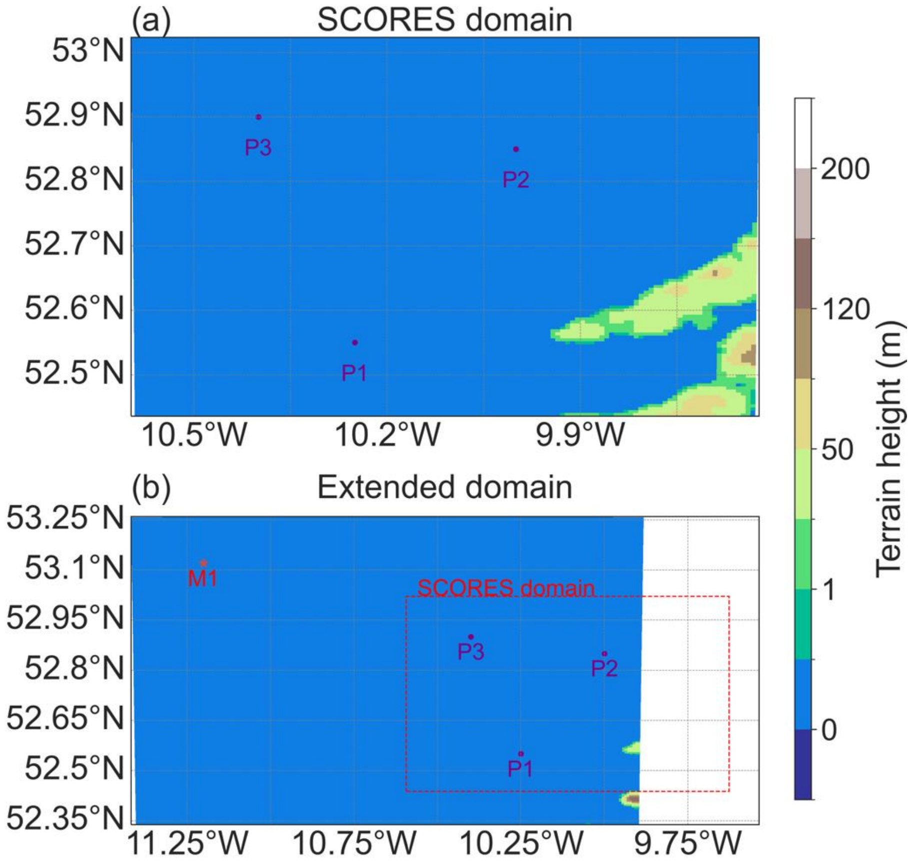

Figure 42: WRF model domain configurations: (a) SCORES domain for 31-year hindcast simulations (1990-01-01 to 2021-01-01), consisting of 128*128 grid points; (b) Extended domain for 1-year validation simulations (2003-03-01 to 2004-03-01), consisting of 200*200 grid points. One coastal buoy is shown with stars in (b), and purple locations (P1-P3) are used for intermodel comparison and resource assessment.

4.2.2 Observational data

Observations used for the model validation were collected from a single coastal marine buoy, M1. Table 13 provides important information about the buoys, while the locations of these buoys are illustrated in Figure 42. Wind and surface air temperature measurements taken from the 1st of March 2003 to the 1st of March 2004 (1 year) were selected, and the choice of this period was related to measured data availability and quality criteria. The wind speed at 3m are extrapolated to 10m using the log law equation.

Table 13: Some important features of the marine buoy used in Ireland simulation validation.

Name	Location	Distance to shore	Height (m)	Sampling rate (min)	Programme	Period	WMO number
M1	53.1266°N , 11.2°W	~100 km	3	60	Iris Weather Buoy Network	06-02-2001 to 09-07-2007	

4.2.3 Wind data validation

Figure 43 illustrates bivariate histograms of 10m wind speeds from ERA5 and WRF_{Ext} simulations at the M1 buoy site, compared with observations. Both the

This project has received funding from the Europeans Union's Horizon 2020 research & innovation programme under grant agreement number 101036457.

datasets are seen to have similar statistics, with the ERA5 having superior correlation with observations, than $\mathrm{WRF}_{\mathrm{Ext}}$. On the contrary, the ERA5 shows a consistant positive bias, which is considerably reduced in by the $\mathrm{WRF}_{\mathrm{Ext}}$. As mentioned in the Iberia simulation evaluation, the ERA5 shows good accuracy far offshore, which is evident in this case as well. The WRFExt simulations have large spread around the mean, with several points being outliers. This suggest that the wind resource assessment far offshore does not require expensive, high resolution WRF simulations, rather ERA5 works well. However, it is noteworthy that the super-scale resolution wind data is essential in wind wake estimation, which the ERA5 is not capable of.

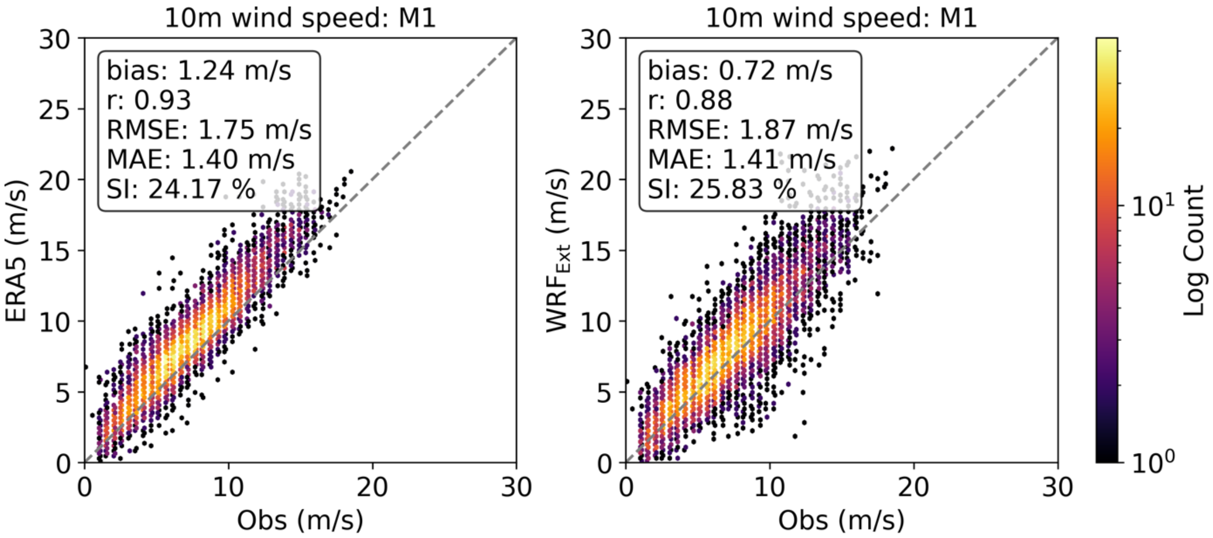

Figure 43: Bivariate histograms depicting the 10m wind speed distribution from ERA5 (1st column and $\mathrm{WRF}_{\mathrm{Ext}}$ simulations (2nd column), compared with the buoy observations: M1. The number of occurrences is presented in log count, with darker (lighter) color indicating low (high) occurrence. The evaluation statistics including bias, RMSE, Pearson's correlation (r), mean absolute error (MAE), and the Scatter Index (SI) are computed to assess the agreement between the three datasets and observational data. The data spans a collection period from 01-03-2003 to 01-03-2004, covering a year-long duration.

When we look at the distributions of the wind speed, as shown in Figure 44, it is clearly visible that the observed distribution is centred around 6 m/s, and has a large swath, where as the ERA5 distribution is centred around 9 m/s and consistently shifts towards right of the observed distribution. In contrast, the $\mathrm{WRF}_{\mathrm{Ext}}$ distribution is centred around 7 m/s, indicating an underestimation of low wind frequencies, but matches to that of the observed distribution over the range of high wind frequencies. In addition, the EMD score is also seen to be less for $\mathrm{WRF}_{\mathrm{Ext}}$, compared to the ERA5, indicating the $\mathrm{WRF}_{\mathrm{Ext}}$ having a close resemblance with observed distribution. From these comparisons, it is evident that the $\mathrm{WRF}_{\mathrm{Ext}}$ simulations are well comparable with the observations.

This project has received funding from the Europeans Union's Horizon 2020 research & innovation programme under grant agreement number 101036457.

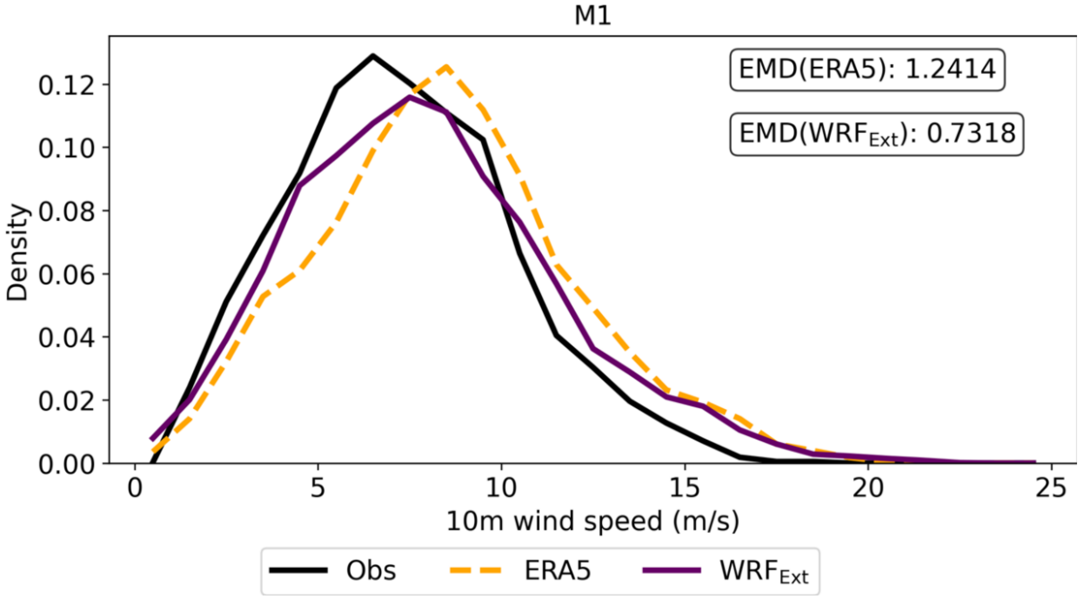

Figure 44: Comparison of 10m wind speed distributions from ERA5 WRF$_{Ext}$ datasets, with respect to the buoy observations, at location M1. EMD is calculated and shown, assessing dissimilarities between the datasets and observational data.

So far, we've assessed the accuracy of the WRF$_{Ext}$ simulations, covering the observational period from 01-01-2011 to 01-01-2012. However, our primary focus is on evaluating the 31-year wind resources from 01-01-1990 to 01-01-2021 using the SCORES domain. Given the observed better agreement with WRF$_{Ext}$ seen earlier, we utilize WRF$_{Ext}$ simulations as a reference to evaluate the accuracy of WRF$_{SCORES}$ simulations. In doing so, we compared wind speed at three heights (100m, 120m, and 150m), extracted at three sample points P1, P2, and P3, from both the domains (which are illustrated in Figure 42), spanning for a period of 1 year from 01-03-2003 to 01-03-2004, and the results are illustrated in Figure 45, Figure 46, and Figure 47.

The bivariate histograms clearly show that the wind speeds are perfectly aligning along the q-q line, with a Pearson's correlation coefficient ranging between 0.93 and 0.96, implying a better agreement between the two datasets. The biases between the datasets are marginal, ranging from -0.29 m/s to 0.08 m/s, implying the dissimilarities between the datasets are infinitesimal. Upon a close inspection, it is observed that the histograms have thinner spread at the sample points P1 and P3, while the spread is little higher at point P2. The same is quantified through the scatter index, which is seen to be around 15% at P1 and 13% at P3, while around 17% at P3. These deviations lead to the marginal differences seen in terms of RMSE and MAE. This validation underscores the accuracy of the WRF$_{SCORES}$ wind dataset, and making it suitable for further wind resource assessments.

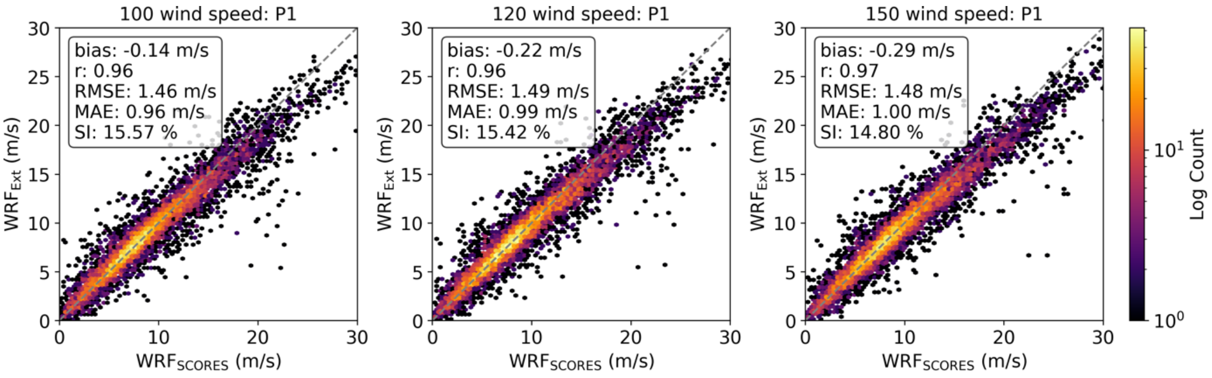

Figure 45: Bivariate histograms depicting the 100m (column 1), 120m (column 2), and 150m (column 3) wind speed distributions from WRF_{SCORES} and WRF_{Ext} simulations, at point P1, during the period from 01-03-2003 to 01-03-2004, covering a year-long duration. The evaluation statistics (RMSE, r, MAE, and SI) are computed to assess the agreement between the two datasets.

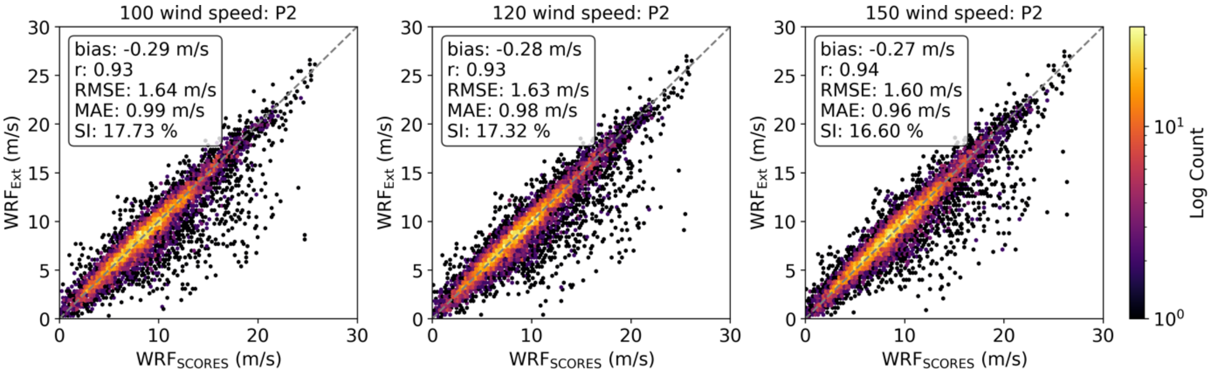

Figure 46: Same as Figure 45, but at point P2.

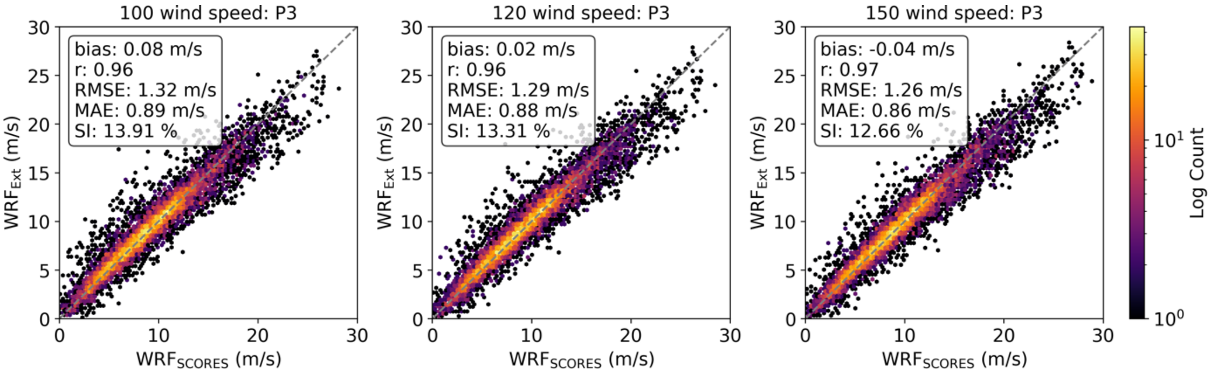

Figure 47: Same as Figure 45, but at point P3.

4.2.4 Temperature validation

Similar to the wind data validation, the temperature validation is also conducted at the buoy observational M1. Figure 48 illustrates the bivariate histograms of 2m temperature, from ERA5 and WRF_{Ext}, compared with the buoy observation at the M1 cite. The comparison clearly shows that the WRF_{Ext} and ERA5 having similar statistics, and are closely following the observations, with a Pearson's correlation of

0.98. Though bias is seen to be lesser in ERA5, the remaining statistics are better seen in WRF$_{\text{Ext}}$, implying the superior accuracy, compared to the ERA5.

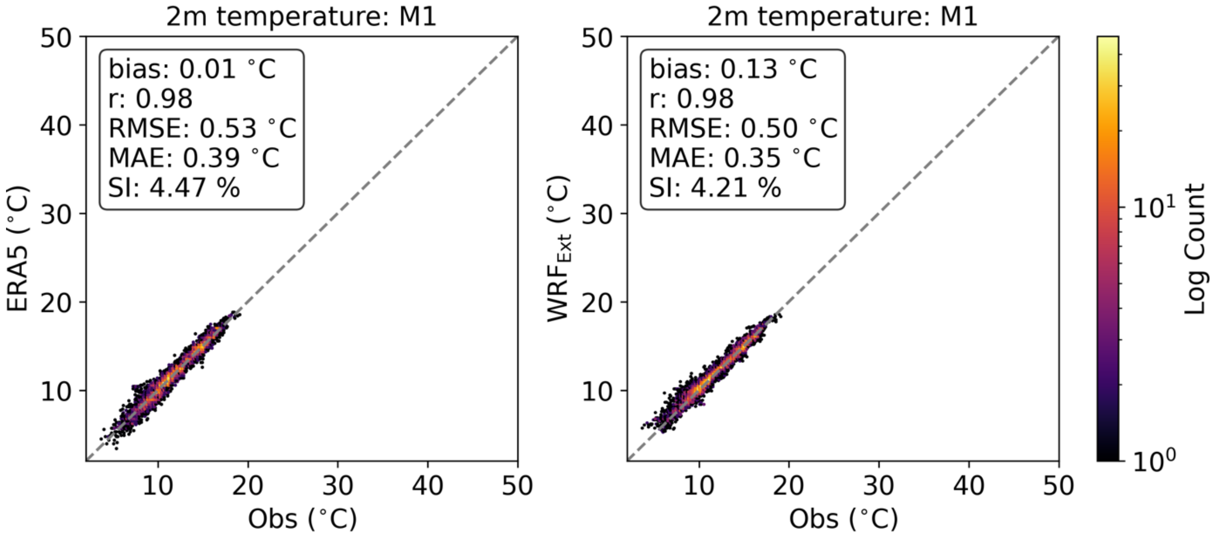

Figure 48: Bivariate histograms depicting the 2m temperature distribution from ERA5 (1st column and WRF$_{\text{Ext}}$ simulations (2nd column), compared with the buoy observation M1. The number of occurrences is presented in log count, with darker (lighter) color indicating low (high) occurrence. The evaluation statistics including bias, RMSE, Pearson's correlation (r), mean absolute error (MAE), and the Scatter Index (SI) are computed to assess the agreement between the three datasets and observational data. The data spans a collection period from 01-03-2003 to 01-03-2004, covering a year-long duration.

Figure 49 illustrates the 2m temperature distributions from the ERA5 and WRF$_{\text{Ext}}$ datasets in comparison with buoy observations at the M1 location. The observations reveal a wider distribution with two peaks, one at 11 °C and another at 15 °C. The distributions from both ERA5 and WRF$_{\text{Ext}}$ also exhibit bimodal peaks, while the ERA5 is slightly underestimating the temperature frequencies between 10 and 15 °C, which lead to the marginal better accuracy in WRF$_{\text{Ext}}$. However, the EMD values is seen to be smaller for ERA5, than the WRF$_{\text{Ext}}$, which is attributed to the better agreement over the range of low temperature frequencies. Irrespective, the temperature dataset obtained through the WRF$_{\text{Ext}}$ simulations is well comparable with the observations as well as the ERA5 reanalysis.

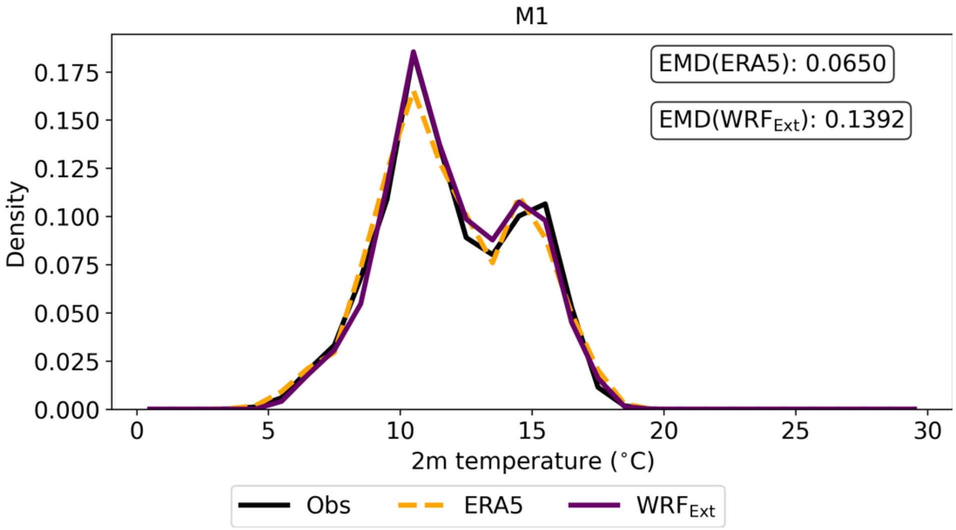

Figure 49: Comparison of 2m temperature distributions from ERA5 WRF$_{Ext}$ datasets, with respect to the buoy observations, at location M1. The Earth Movers Distance (EMD) is calculated and shown, assessing dissimilarities between the datasets and observational data.

Same as we did for wind validation, we have to evaluate the 31-year solar resources from 01-01-1990 to 01-01-2021 using the SCORES domain. Given the observed better agreement with WRF$_{Ext}$ seen earlier, we utilize WRF$_{Ext}$ simulations as a reference to evaluate the accuracy of WRF$_{SCORES}$ simulations. In doing so, we compared 2m temperature, extracted at three sample points P1, P2, and P3, from both the domains (which are illustrated in Figure 42), spanning for a period of 1 year from 01-03-2003 to 01-03-2004, and the results are illustrated in Figure 50.

The bivariate histograms clearly show that the temperatures are perfectly aligning along the q-q line, with a Pearson's correlation coefficient 1, implying a better agreement between the two datasets. In addition, the other evaluation metrics also show negligible deviations from one another, indicating that the SCORES domain simulations are indeed similar to that of the Extended domain simulations.

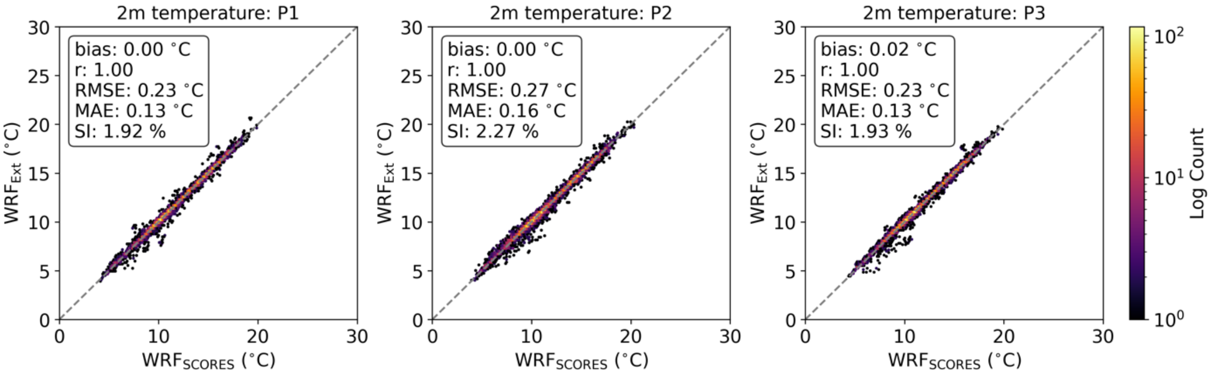

Figure 50: Bivariate histograms depicting the 2m temperature distributions from WRF$_{SCORES}$ and WRF$_{Ext}$ simulations, at point P1 (1st column), P2 (2nd column), and P3 (3rd column), during the period from 01-03-2003 to 01-03-2004, covering a year-long duration. The evaluation statistics (RMSE, r, MAE, SI, and the EMD) are computed to assess the agreement between the two datasets.

This project has received funding from the Europeans Union's Horizon 2020 research & innovation programme under grant agreement number 101036457.

4.2.5 Overview of the utilized computational facilities

Table 14 illustrates the details of computational facilities utilized for a single WRF model run, with the Extended domain configuration for the validation simulations and SCORES configuration for the 31-year simulations, over the Ireland coast. A total of 74 runs are performed for validation simulations (covering 1 year period), while a total of 2265 runs are performed for the SCORES simulations (covering 31-year period). Based on the statistics provided, a total of 83,472 CPU hours were utilized for the validation simulations (74 runs), while a total of 8,15,400 CPU hours were utilized for the SCORES simulations (2265 runs), excluding the queue time. dividing the CPU hours by the number of CPUs since they run in parallel, which will give 4884 hours of real-time for the validation simulations and 1,01,925 hours of real-time for the SCORES simulations, excluding the queue time and analysis time.

Table 14: Details of computational facilities utilized for a single WRF model run over the Ireland coast

	WRF_{Ext} simulations	**WRF_{SCORES} simulations**
Grid size	200*200	128*128
Simulation Duration (h)	144	144
Nodes	1	1
Cores per node	16	8
Total CPU hours	1128	360
Storage accumulation (GB)	14	9

4.3 BeNeLux

4.3.1 WRF model domain configuration

The WRF model is configured with single domain, of 0.5 km resolution. Figure 51 illustrates the WRF model domain configuration adopted for the numerical simulations of 31 years hindcasts, which is termed as SCORES domain here after. The SCORES domain consists of 200*200 grid points in the latitude and longitudinal directions. There are two observational cites identified within the domain, which are shown in Figure 51. In addition, three sample points P1 to P3, are used for intramodel validation and resource assessment. The model simulations are performed according to the simulation strategy stated earlier.

This project has received funding from the Europeans Union's Horizon 2020 research & innovation programme under grant agreement number 101036457.

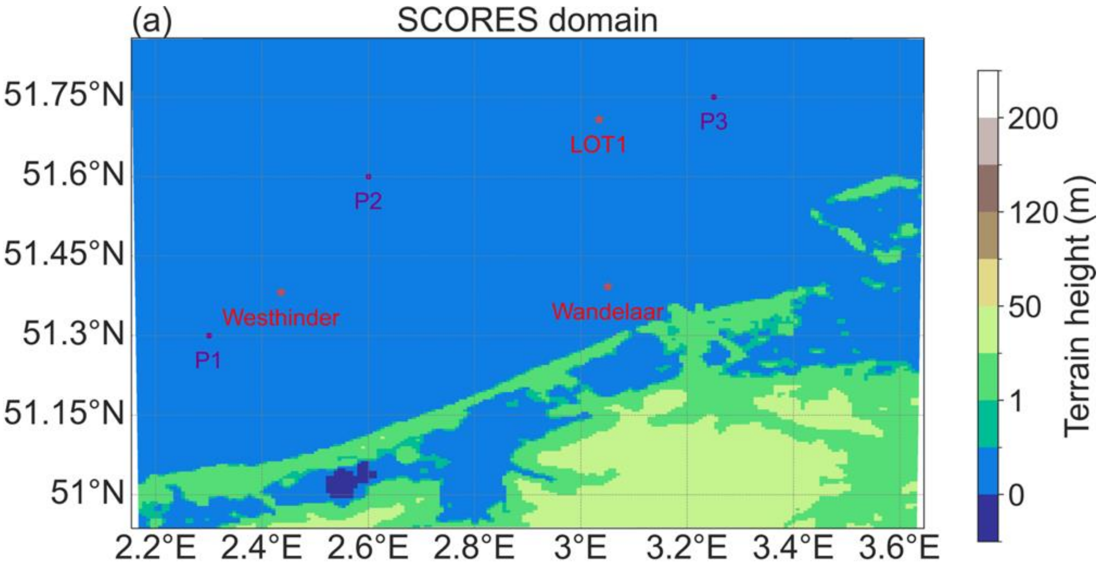

Figure 51: WRF model domain configurations: SCORES domain for 31-year hindcast simulations (1990-01-01 to 2021-01-01), consisting of 200*200 grid points. two coastal buoy is shown with stars, and purple locations (P1-P3) are used for intermodel comparison and resource assessment.

4.3.2 Observational data

Observations used for the model validation were collected from two coastal measuring piles, namely Wandelaar and Westhinder. Table 15 provides important information about the measurements, while the locations of them are illustrated in Figure 51. Wind and surface air temperature measurements taken from the 1st of February 2016 to the 1st of February 2017 (1 year) were selected, and the choice of this period was related to measured data availability and quality criteria. Wind speed is available at 10m height, thus no extrapolation is performed.

Table 15: Some important features of the marine measuring piles used in BeNeLux simulation validation

Name	**Location**	**Distance to shore**	**Height (m)**	**Sampling rate (min)**	**Programme**	**Period**	**WMO number**
Wandelaar	51.329°N, 3.051°E	~5 km	10	60	Flemish banks monitoring network	01-02-2016 to 01-02-2017	9030
Westhinder	51.381°N, 2.436°E	~15 km	10	60	Flemish banks monitoring network	01-02-2016 to 01-02-2017	9035

4.3.3 Wind data validation

Figure 52 illustrates bivariate histograms of 10m wind speeds from ERA5 and WRF_{Ext} simulations at the Wandelaar site, compared with observations. The ERA5 dataset appears to largely underestimate wind speeds at this location, as evident from the significant negative bias observed. Furthermore, the ERA5 data show a limitation in reproducing winds exceeding 15 m/s near coastal boundaries, while observed winds reach up to 24 m/s. In contrast, bivariate histograms of wind speeds from WRF_{Ext} simulations are performing better by reducing the bias. Also, the WRF simulations reproduced high winds reaching 24 m/s, with a Pearsons' correlation of 0.89, indicating the superior accuracy. The reason could be the land-

This project has received funding from the Europeans Union's Horizon 2020 research & innovation programme under grant agreement number 101036457.

sea interactions, which the WRF model is well capable of resolving due to the super-scale resolution, while the ERA5 failed due to its coarse resolution.

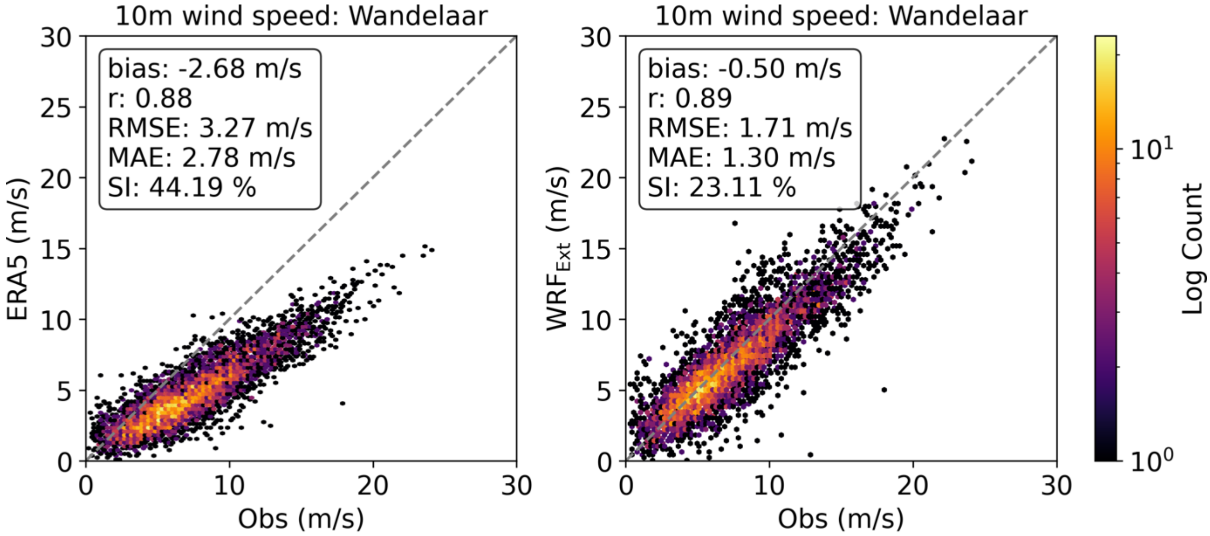

Figure 52: Bivariate histograms depicting the 10m wind speed distribution from ERA5 (1st column and WRF$_{Ext}$ simulations (2nd column), compared with the observations, at Wandelaar. The number of occurrences is presented in log count, with darker (lighter) color indicating low (high) occurrence. The evaluation statistics including bias, RMSE, Pearson's correlation (r), mean absolute error (MAE), and the Scatter Index (SI) are computed to assess the agreement between the three datasets and observational data. The data spans a collection period from 01-02-2016 to 01-02-2017, covering a year-long duration.

When we look at the distribution, as shown in Figure 53, the observed distribution extends over a considerable range, centered around a mode of 5 m/s. ERA5 exhibits a skewed distribution centered around a mode of 3 m/s, which significantly underestimates wind speed frequencies beyond 5 m/s, while overestimating frequencies around 3 m/s. These findings align with the large negative biases estimated earlier. The simulations from WRF$_{Ext}$ are closely follows the observed distribution at all wind speeds. This alignment is consistent with the marginal negative bias seen earlier. The EMD, which quantifies the similarity between the distributions, clearly shows that the WRF$_{Ext}$ is having least score, implying a better agreement with the observed distribution, than the ERA5.

This project has received funding from the Europeans Union's Horizon 2020 research & innovation programme under grant agreement number 101036457.

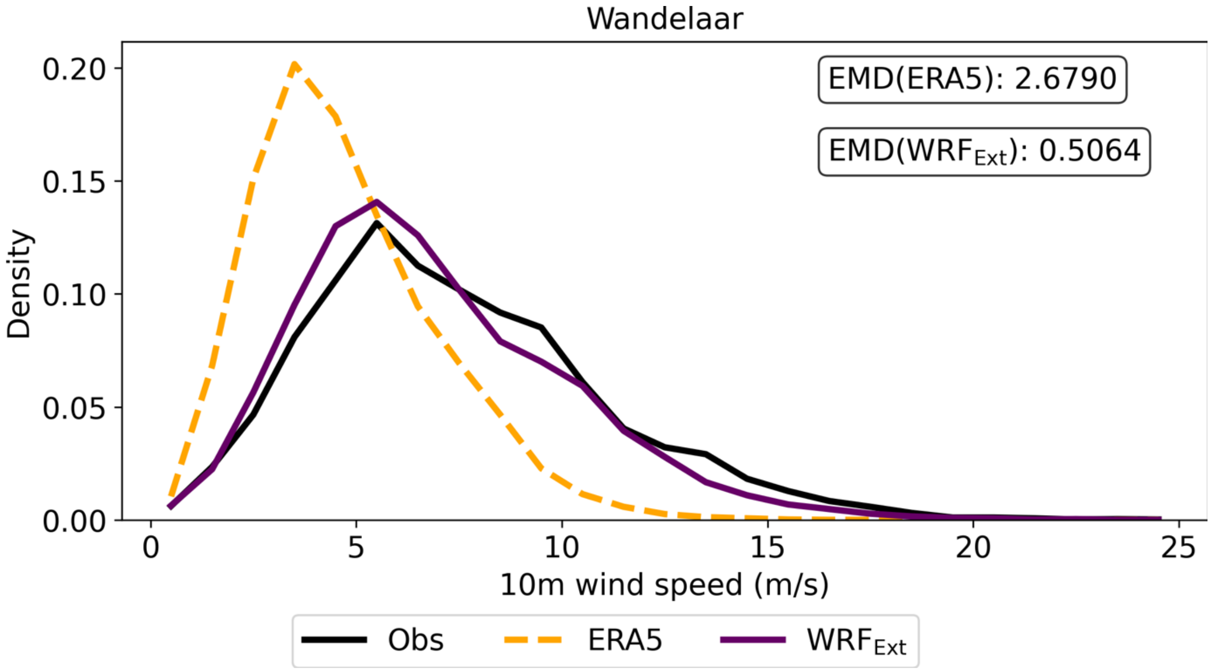

Figure 53: Comparison of 10m wind speed distributions from ERA5 WRF$_{Ext}$ datasets, with respect to the observations, at location Wandelaar. The Earth Movers Distance (EMD) is calculated and shown, assessing dissimilarities between the datasets and observational data.

Figure 54 illustrates bivariate histograms of 10m wind speeds from ERA5 and WRF$_{Ext}$ simulations at the Westhinder site, compared with observations. The ERA5 dataset appears to underestimate wind speeds over high wind speeds, as evident from the negative bias. Furthermore, the ERA5 data show a limitation in reproducing winds exceeding 20 m/s, while observed winds reach up to 29 m/s. In contrast, the bivariate histograms of wind speeds from WRF$_{Ext}$ simulations are seen to marginally improve the bias, but the remaining statistics, such as Pearson's correlation, RMSE, MAE, and SI are comparably poorer than ERA5. One possible reason for this marginal poor performance is that the simulations doesnot use ny kind of assimilation during the course of simulation duration, while the ERA5 does. Since each run is performed for six days, the simulation accuracy degrades with each passing hour, which is well known fact. Neverthles, the WRF$_{Ext}$ simulations are well comparable with the observations and ERA5, far offshore.

This project has received funding from the Europeans Union's Horizon 2020 research & innovation programme under grant agreement number 101036457.

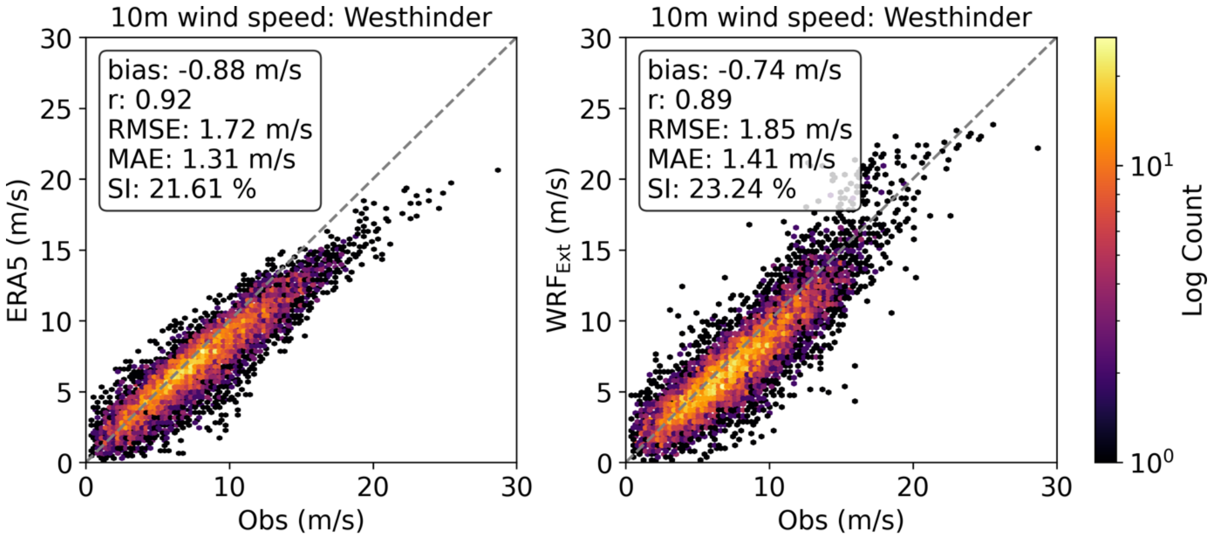

Figure 54: Same as Figure 52, but at observational location Westhinder.

Figure 55 illustrates the 10m wind speed distributions from the ERA5 and WRF$_{Ext}$ datasets in comparison with buoy observations at the Westhinder location. The observed distribution extends over a considerable range, centered around a mode of 7 m/s. Interestingly, both ERA5 and WRF$_{Ext}$ exhibit a skewed distribution towards left of the observed one, the WRF$_{Ext}$ is centered around 5 m/s, while the ERA5 is centered around a mode of 6 m/s. Both the datasets underestimate winds frequencies at all ranges. However, the WRF$_{Ext}$ distribution is relatively closer to the observed one during high winds, compared to the ERA5, which lead to the less bias in seen earlier. The EMD of WRF$_{Ext}$ is seen to be less than that of the ERA5, implying a better accuracy of WRF$_{Ext}$ simulations.

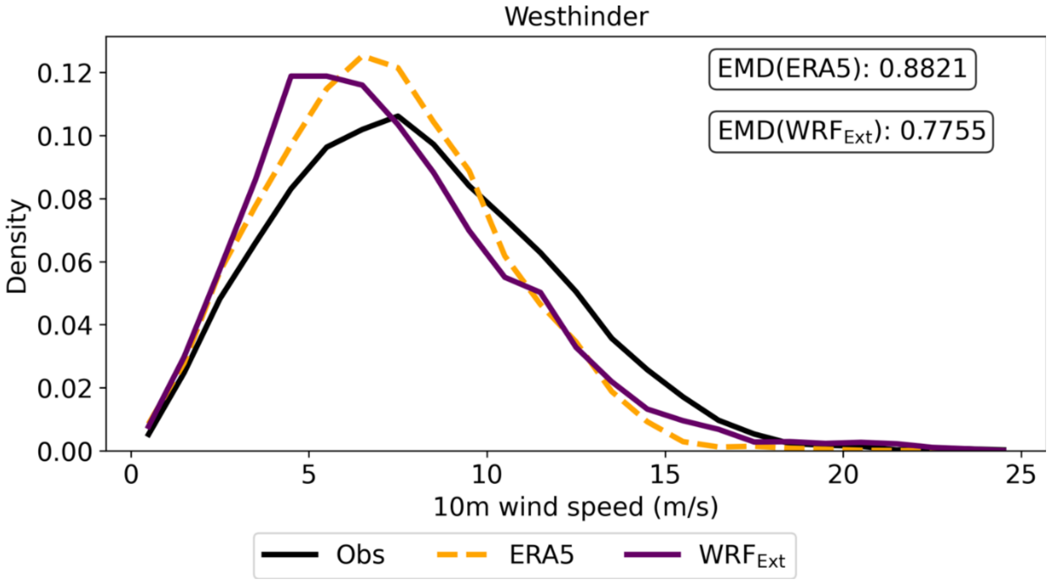

Figure 55: Same as Figure 53, but at observational location Westhinder.

4.3.4 Temperature validation

Similar to the wind data validation, the temperature validation is also conducted at the observational cites. Figure 56 illustrates the bivariate histograms of 2m

This project has received funding from the Europeans Union's Horizon 2020 research & innovation programme under grant agreement number 101036457.

temperature, from ERA5 and WRF_{Ext}, compared with the observations at the Wandelaar cite. The comparison clearly shows that the WRF_{Ext} simulations having highest similarity with the observations, with Pearson's correlation of 0.99, while that of the ERA5 is 0.96. Apart from *r*, the other metrics are also seen to be better for WRF_{Ext} simulations, compared to the ERA5, indicating the superior accuracy of WRF_{Ext} simulating surface air temperature. The ERA5, on the other hand, is seen to have two peaks, and clearly off the diagonal line, implying poor accuracy, which is attributed to the land-sea interactions, due the close proximity of the observational cite to the shore.

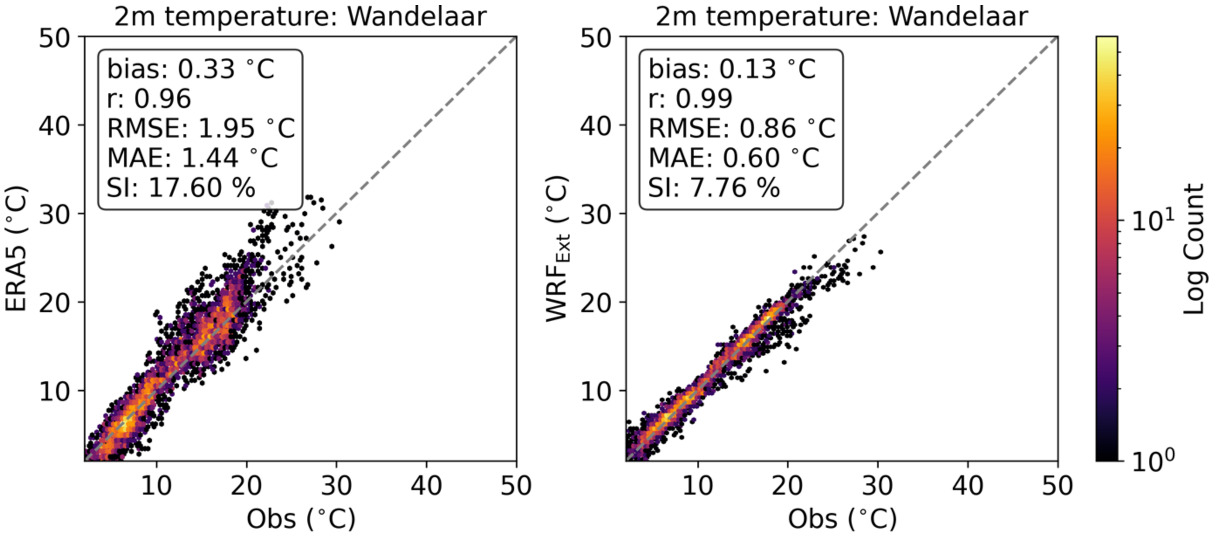

Figure 56: Bivariate histograms depicting the 2m temperature distribution from ERA5 (1st column and WRF_{Ext} simulations (2nd column), compared with the observations, at Wandelaar. The number of occurrences is presented in log count, with darker (lighter) color indicating low (high) occurrence. The evaluation statistics including bias, RMSE, Pearson's correlation (r), mean absolute error (MAE), and the Scatter Index (SI) are computed to assess the agreement between the three datasets and observational data. The data spans a collection period from 01-02-2016 to 01-02-2017, covering a year-long duration.

Figure 57 illustrates the 2m temperature distributions from the ERA5 and WRF_{Ext} datasets in comparison with observations at the Wandelaar location. The observations reveal a wider distribution with three peaks, one at 7 °C, another at 15 °C, and the last at 17 °C. The distribution from WRF_{Ext} also exhibit three peaks, while the ERA5 only shows bimodal peaks. The ERA5 overestimates low (<5°C) and high (>20°C) temperature frequencies, while consistently underestimates temperatures in within the range. On the contrary, the WRF_{Ext} distribution closely follows the observed distribution, at all temperature ranges, indicating a superior accuracy. The same has been quantified through the EMD, which is seen to be lesser for WRF_{Ext} than the ERA5.

This project has received funding from the Europeans Union's Horizon 2020 research & innovation programme under grant agreement number 101036457.

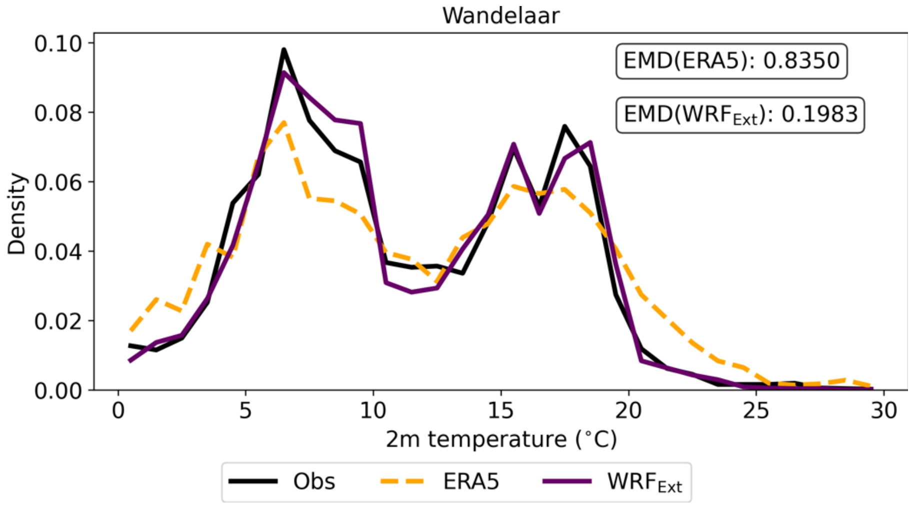

Figure 57: Comparison of 2m temperature distributions from ERA5 WRF$_{Ext}$ datasets, with respect to the observations, at location Wandelaar. The Earth Movers Distance (EMD) is calculated and shown, assessing dissimilarities between the datasets and observational data.

Figure 58 illustrates the bivariate histograms of 2m temperature, from ERA5 and WRF$_{Ext}$, compared with the observations at the Westhinder cite. The comparison clearly shows that the datasets from ERA5 and WRF$_{Ext}$ simulations having similar statistics, with a Pearson's correlation of 0.99, implying the comparable accuracy among the two datasets.

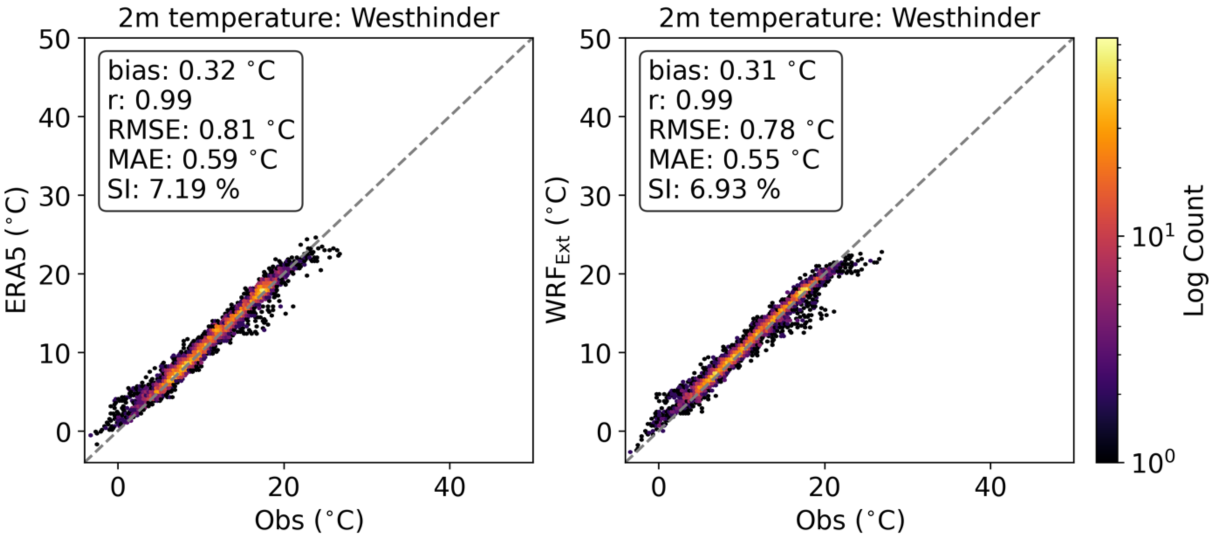

Figure 58: Same as Figure 56, but for observational location Westhinder.

When we look at the distributions, as shown in Figure 59, The observations reveal a wider distribution with three distinct peaks, one at 7 °C, another at 15 °C, and the last at 17 °C. The distributions from ERA5 and WRF$_{Ext}$ are also having three peaks, and are closely following the observed distribution. However, the ERA5 is showing slight underestimation around 17 °C. Nevertheless, the WRF$_{Ext}$ simulations are well comparable with the observations as well as the ERA5 reanalysis.

This project has received funding from the Europeans Union's Horizon 2020 research & innovation programme under grant agreement number 101036457.

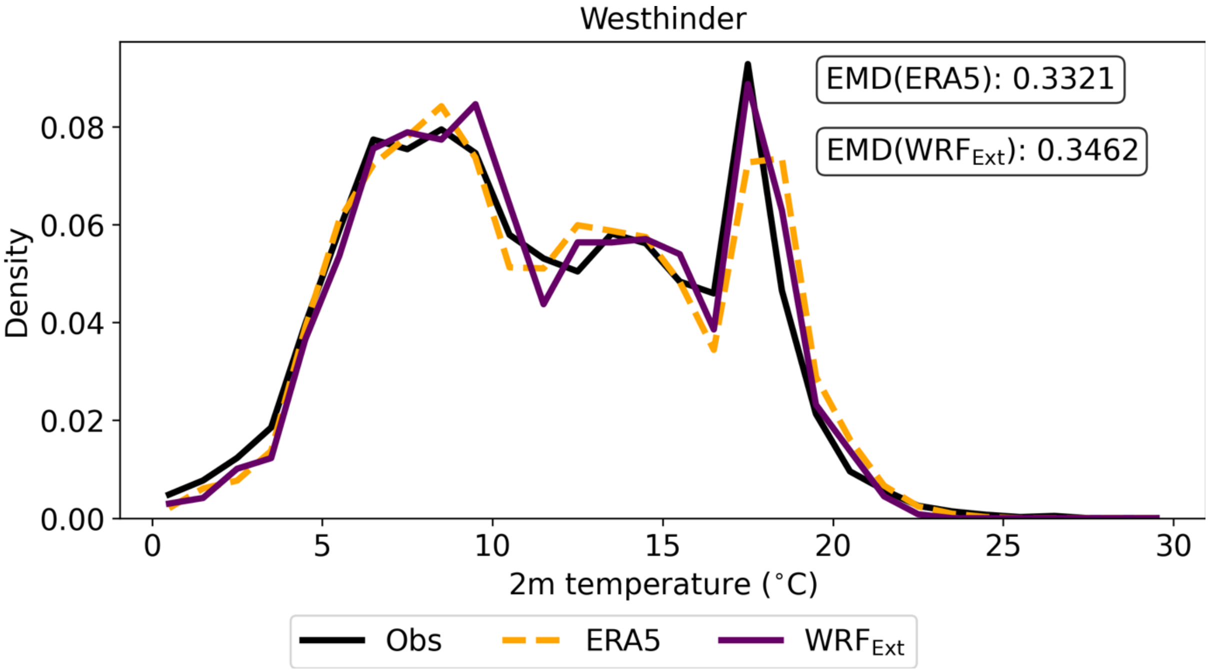

Figure 59: Same as FIgure 57, but for observational location Westhinder.

4.3.5 Overview of the utilized computational facilities

Table 14 illustrates the details of computational facilities utilized for a single WRF model run, with the SCORES configuration for the 31-year simulations, over the Ireland coast. A total of 2265 runs are performed for the SCORES simulations (covering 31-year period). Based on the statistics provided, a total of 25,50,390 CPU hours were utilized for the SCORES simulations (2265 runs), excluding the queue time. dividing the CPU hours by the number of CPUs since they run in parallel, which will give 159400 hours of real-time for the SCORES simulations, excluding the queue time and analysis time.

Table 16: Details of computational facilities utilized for a single WRF model run over the BeNeLux coast

	WRF$_{SCORES}$ simulations
Grid size	200*200
Simulation Duration (h)	144
Nodes	1
Cores per node	16
Total CPU hours	1128
Storage accumulation (GB)	14

This project has received funding from the Europeans Union's Horizon 2020 research & innovation programme under grant agreement number 101036457.

5 Data series descriptions and repositories

Where the open source data are located and detailed README file explained here

5.1 The ECHOWAVE hindcast

The 32 years of output files from the ECHOWAVE hindcast are in NetCDF format. All generated files have a 1-hour output time resolution.

There are 3 types of gridded output, corresponding to each one of the grid domains described in the model setup (Figure 1). The gridded output is referred to as the "field" files. The standardized name structure of the field files is:

TU-MREL_<Grid_ID>_YYYY.nc

Here **<Grid_ID>**, can have 3 different IDs:

- **N_ATL-15M** (field output from the North Atlantic grid)
- **N_ATL-8M** (field output from the European coastal shelf grid)
- **EU_ATL-2M** (field output from the high resolution coastal grid)

Then, **YYYY** indicates the modelled year: 1990 to 2021.

The following variables are included in the yearly field files:

- hs: Significant wave height in m.
- fp: Spectral peak frequency in Hz. (fp^{-1}=peak period in s).
- dp: Peak direction (Nautical convention "wave from").
- dir Mean wave direction in degrees (Nautical convention "wave from").
- lm: Mean wave length in m.
- t01: Mean wave period from first frequency moment in s.
- t02: Mean wave period from second frequency moment in s.
- spr: Directional spreading
- ucur: eastward current in m/s.
- vcur: northward current in m/s.
- uwnd: eastward wind in m/s.
- vwnd: northward wind in m/s.
- wlv: sea surface height above mean sea level in m.
- phs0: Significant wave height of partition 0.
- phs1: Significant wave height of partition 1.
- phs2: Significant wave height of partition 2.
- ptp0: Dominant (peak) wave period at partition 0.
- ptp1: Dominant (peak) wave period at partition 1.
- ptp2: Dominant (peak) wave period at partition 2.
- pdir0: Mean wave direction of partition 0.
- pdir1: Mean wave direction of partition 1.
- pdir2: Mean wave direction of partition 2.
- pdp0: Dominant (peak) wave direction from partition 0.
- pdp1: Dominant (peak) wave direction from partition 1.
- pdp2: Dominant (peak) wave direction from partition 2.

- dpt: Depth in m.

The directional wave spectrum is also outputted at specific locations. An output grid of about 6x6 km resolution was created to extract the 2D wave spectrum. Among many applications, these files can be used as boundary conditions for the development of future higher resolution models in coastal areas. The standardized name structure of the 2D spectral files is:

TU-MREL_**<location_ID>**_**YYYY**_spec.nc

Here, **<location_ID>** is the name code for a specific location corresponding to the position of a buoy (like the ones used for validation), or the output grid coordinates, for example: **1056W5244N**. This location code mean that the spectral data is taken from longitude 10.56° W, latitude 52.44° N. A total of 5485 spectral files were created per year.

As for the field files, **YYYY** indicates the modelled year: 1990 to 2021.

The 2D spectral files contain the following variables:

- efth: Spectral direction al wave variance in m^2s/rad (as function of frequency, direction and time). In this case the directional convention is nautical “wave to”.
- dpt: Depth in m.
- wnd: Wind speed at 10 m (m/s).
- wnddir: Wind direction (nautical from convention).
- cur: Sea water speed (current) in m/s.
- curdir: Current direction (nautical from convention).

Finally, output files with the 1D frequency spectrum are also created base on the directional spectral files. The standardized name structure of the 1D spectral files is:

TU-MREL_**<location_ID>**_**YYYY**_spec.nc

As before, **<location_ID>** is the name code for a specific location corresponding to the position of a buoy (like the ones used for validation), or the output grid coordinates, and **YYYY** indicates the modelled year: 1990 to 2021.

The 1D frequency spectrum files contain the following variables:

- ef: spectral wave variance spectrum in m^2s (as function of frequencies and time).
- th1m mean wave direction from first frequency moment in degrees (Nautical convention “wave from”).
- th2m mean wave direction from second frequency moment in degrees (Nautical convention “wave from”).
- sth1m mean wave spreading direction from first frequency moment (in degrees).
- sth2m mean wave spreading direction from second frequency moment (in degrees).
- dpt: depth in m.

- wnd: Wind speed at 10 m (m/s).
- wnddir: Wind direction (nautical from convention).
- cur: Sea water speed (current) in m/s.
- curdir: Current direction (nautical from convention).

For further details on how the variables are computed ,please refer to the WW3 manual (The WAVEWATCH III® Development Group, 2019).

5.2 The SWaGZ dataset

The 31 years of wind and solar datasets, called SWaGZ (Solar Wind at Gray-Zone), simulated at the 0.5 km gray-zone resolution, are provided in netCDF format. All output variables are stored at a 1-hour temporal resolution.

The datasets are saved individually for the three locations: Portugal coast, Ireland coast, and the Netherlands coast. The following is a tree of file structure, consistent across all the locations. Each file contains 31 years of data at every hour.

- XLAND.nc: Land sea mask, either 0 or 1, indicating land or sea. Only available for 1 time step. This file also contains the XLAT and XLONG coordinates, which are also present in each of the following variables.
- ws_10.nc: wind speed at 10 m level, in m/s
- ws_80.nc: wind speed at 80 m level, in m/s
- ws_100.nc wind speed at 100 m level, in m/s
- ws_120.nc: wind speed at 120 m level, in m/s
- ws_150.nc: wind speed at 150 m level, in m/s
- wpd_80.nc: wind power density at 80 m level, in W/m^2
- wpd_100.nc: wind power density at 100 m level, in W/m^2
- wpd_120.nc: wind power density at 120 m level, in W/m^2
- wpd_150.nc: wind power density at 150 m level, in W/m^2
- 8MW: This is a folder, corresponds to 8 MW turbine model
    - tp_80.nc: turbine power obtained using the 8MW turbine model and wind speed at 80 m level, in KW
    - tp_100.nc: turbine power obtained using the 8MW turbine model and wind speed at 100 m level, in KW
    - tp_120.nc: turbine power obtained using the 8MW turbine model and wind speed at 120 m level, in KW
    - tp_150.nc: turbine power obtained using the 8MW turbine model and wind speed at 150 m level, in KW
- 15MW: This is a folder, corresponds to 15 MW turbine model
    - tp_80.nc: turbine power obtained using the 15MW turbine model and wind speed at 80 m level, in KW
    - tp_100.nc: turbine power obtained using the 15MW turbine model and wind speed at 100 m level, in KW
    - tp_120.nc: turbine power obtained using the 15MW turbine model and wind speed at 120 m level, in KW
    - tp_150.nc: turbine power obtained using the 15MW turbine model and wind speed at 150 m level, in KW
- T2.nc: Air temperature at 2 m level, in °C
- SWDOWN2.nc: Downward solar shortwave radiation at the surface (equivalent to the Global Horizontal Irradiance (GHI)), in W/m^2

- spv.nc: Solar power obtained using the utilized solar module, in W/m^2

This project has received funding from the Europeans Union’s Horizon 2020 research & innovation programme under grant agreement number 101036457.

6 References

The WAVEWATCH III® Development Group. (2019). *User Manual and System Documentation*. Tech. Note, NOAA/NWS/NCEP/MMAB.

Accensi, M., Alday, M., Maisondieu, C., Raillard, N., Darbynian, D., Old, C., . . . others. (2021). ResourceCODE framework: A high-resolution wave parameter dataset for the European Shelf and analysis toolbox. Retrieved from https://archimer.ifremer.fr/doc/00736/84812/

Alday, M., Accensi, M., Ardhuin, F., & Dodet, G. (2021). A global wave parameter database for geophysical applications. Part 3: Improved forcing and spectral resolution. *Ocean Modelling, 166*, 101848.

Alday, M., Ardhuin, F., Dodet, G., & Accensi, M. (2022). Accuracy of numerical wave model results: application to the Atlantic coasts of Europe. *Ocean Science, 18*(6), 1665--1689. doi:10.5194/os-18-1665-2022

Ardhuin, F., & Roland, A. (2012). Coastal wave reflection, directional spreading, and seismo-acoustic noise sources. *Journal of Geophysical Research, 117*, C00J20. doi:10.1029/2011JC007832

Ardhuin, F., Chapron, B., & Collard, F. (2009). Observation of swell dissipation across oceans. *Geophysical Research Letters, 36*, L06607. doi:10.1029/2008GL037030

Ardhuin, F., Dumas, F., Bennis, A.-C., Roland, A., Sentchev, A., Forget, P., . . . Benoit, M. (2012). Numerical wave modeling in conditions with strong currents: dissipation, refraction and relative wind. *Journal of Physical Oceanography, 42*, 2101-2120. doi:https://doi.org/10.1175/JPO-D-11-0220.1

Ardhuin, F., O'Reilly, W. C., Herbers, T. H., & Jessen, P. F. (2003). Swell transformation across the continental shelf. Part I: Attenuation and directional broadening. *Journal of Physical Oceanography, 33*, 1921-1939. doi:doi/pdf/10.1175/1520-0485%282003%29033%3C1921%3ASTATCS%3E2.0.CO%3B2

Ardhuin, F., Otero, M., Merrifield, S., Grouazel, A., & Terrill, E. (2020). Ice Breakup Controls Dissipation of Wind Waves Across Southern Ocean Sea Ice. *Geophysical Research Letters, 47*, e2020GL087699. doi:10.1029/2020GL087699

Ardhuin, F., Rogers, E., Babanin, A. V., Filopot, J.-F., Magne, R., Roland, A., . . . others. (2010). Semiempirical Dissipation Source Functions for Ocean Waves. Part I: Definition, Calibration, and Validation. *Journal of Physical Oceanography, 40*, 1917--1941. doi:DOI: 10.1175/2010JPO4324.1

Azhar, M. a. (2020). Evaluation of the reanalysis surface solar radiation from NCEP, ECMWF, NASA, and JMA using surface observations for Balochistan, Pakistan. *Journal of Renewable and Sustainable Energy, 12*(2).

Azhar, M. a. (2020). The evaluation of reanalysis and analysis products of solar radiation for Sindh province, Pakistan. *Renewable energy*, 347-362.

This project has received funding from the Europeans Union's Horizon 2020 research & innovation programme under grant agreement number 101036457.

Boutin, G., Ardhuin, F., Dumont, D., Sévigny, C., & Girard-Ardhuin, F. (2018). Floe size effects on wave-ice interactions: theoretical background, implementation and applications. *Journal of Geophysical Research, 123*, 4779-4805. doi:doi.org/10.1029/2017JC013622

Carvalho, D. a.-G. (2017). Offshore winds and wind energy production estimates derived from ASCAT, OSCAT, numerical weather prediction models and buoys--A comparative study for the Iberian Peninsula Atlantic coast. *Renewable energy*, 433-444.

Chawla, A., & Tolman, H. L. (2008). Obstruction grids for spectral wave models. *Ocean Modelling, 22*, 12-25. doi:doi.org/10.1016/j.ocemod.2008.01.003

Chawla, A., Spindler, D. M., & Tolman, H. L. (2013). Validation of a thirty year wave hindcast using the Climate Forecast System Reanalysis winds. *Ocean Modelling, 70*, 189--206. doi:https://doi.org/10.1016/j.ocemod.2012.07.005

Chawla, A., Tolman, H. L., Gerald, V., Spindler, D., Spindler, T., Alves, J.-H., . . . Eve-Marie. (2013). A Multigrid Wave Forecasting Model: A New Paradigm in Operational Wave Forecasting. *Weather and Forecasting, 28*, 1057-1078. doi:10.1175/waf-d-12-00007.1

Dee, D. P. (2011). The ERA-Interim reanalysis: Configuration and performance of the data assimilation system. *Quarterly Journal of the royal meteorological society*, 553-597.

Dibarboure, G., Lamy, A., Pujol, M.-I., & Jettou, G. (2018). The drifting phase of SARAL: Securing stable ocean mesoscale sampling with an unmaintained decaying altitude. *Remote Sensing, 10*, 1051. doi:https://doi.org/10.3390/rs10071051

Dodet, G., Piolle, J.-F., Quilfen, Y., Abdalla, S., Accensi, M., Ardhuin, F., . . . others. (2020). The Sea State CCI dataset v1: towards a sea state climate data record based on satellite observations. *Earth System Sci. Data, 12*, 1929--1951. doi:10.5194/essd-12-1929-2020

Draxl, C. a.-M. (2015). The wind integration national dataset (wind) toolkit. *Applied Energy*, 355-366.

Durrant, T. H., Greenslade, D. J., & Simmonds, I. (2009). Validation of Jason-1 and Envisat remotely sensed wave heights. *Journal of Atmospheric and Oceanic Technology, 26*, 123-134. doi:https://doi.org/10.1175/2008JTECHO598.1

Echevarria, E. R., Hemer, M. A., & Holbrook, N. J. (2021). Global implications of surface current modulation of the wind-wave field. *Ocean Modelling, 161*, 101792. doi:https://doi.org/10.1016/j.ocemod.2021.101792

Eriksson, O. a.-P. (2015). Wake downstream of the Lillgrund wind farm-A Comparison between LES using the actuator disc method and a Wind farm Parametrization in WRF. *Journal of physics: Conference series*, 12-28.

Fischereit, J. a. (2022). Review of mesoscale wind-farm parametrizations and their applications. *Boundary-Layer Meteorology*, 175-224.

This project has received funding from the Europeans Union's Horizon 2020 research & innovation programme under grant agreement number 101036457.

Fitch, A. C. (2012). Local and mesoscale impacts of wind farms as parameterized in a mesoscale NWP model. *Monthly Weather Review*, 3017-3038.

Frank, C. W. (2020). The added value of high resolution regional reanalyses for wind power applications. *Renewable Energy*, 1094-1109.

Gelaro, R. a. (2017). The modern-era retrospective analysis for research and applications, version 2 (MERRA-2). *Journal of climate*, 5419-5454.

Girard-Ardhuin, F., & Ezraty, R. (2012). Enhanced Arctic sea ice drift estimation merging radiometer and scatterometer data. *IEEE Transactions on Geoscience and Remote Sensing, 50*(7), 2639--2648.

Goccmen, T. a.-E. (n.d.). Wind turbine wake models developed at the technical university of Denmark: A review. *Renewable and Sustainable Energy Reviews*, 752-769.

Grant, W. D., & Madsen, O. S. (1979). Combined wave and current interaction with a rough bottom. *Journal of Geophysical Research: Oceans, 84*, 1797-1808.

Gualtieri, G. (2022). Analysing the uncertainties of reanalysis data used for wind resource assessment: A critical review. *Renewable and Sustainable Energy Reviews, 167*, 112741.

Hahmann, A. N.-B.-R. (2020). The making of the New European Wind Atlas--part 1: model sensitivity. *Geoscientific model development*, 5053-5078.

Hanafin, J., Quilfen, Y., Ardhuin, F., Sienkiewicz, J., Queffeulou, P., Obrebski, M., . . . others. (2012). Phenomenal sea states and swell radiation: a comprehensive analysis of the 12-16 February 2011 North Atlantic storms. *Bulletin of the American Meteorological Society, 93*, 1825-1832. doi:10.1175/BAMS-D-11-00128.1

Hasselmann, S., & Hasselmann, K. (1985). Computations and parameterizations of the nonlinear energy transfer in a gravity-wave spectrum. Part I: A new method for efficient computations of the exact nonlinear transfer integral. *Journal of Physical Oceanography, 15*, 1369-1377.

Haupt, S. E. (2016). The SunCast solar-power forecasting system: the results of the public-private-academic partnership to advance solar power forecasting. *National Center for Atmospheric Research (NCAR), Boulder (CO): Research Applications Laboratory, Weather Systems and Assessment Program (US).*

Hersbach, H. a.-S. (2020). The ERA5 global reanalysis. *Quarterly Journal of the Royal Meteorological Society*, 1999-2049.

Hersbach, H., Bell, B., Berrisford, P., Hirahara, S., Horányi, A., Muñoz-Sabater, J., . . . others. (2020). The ERA5 global reanalysis. *Quarterly Journal of the Royal Meteorological Society, 146*, 1999--2049. doi:10.1002/qj.3803

Janssen, P. A. (1991). Quasi-linear theory of wind wave generation applied to wave forecasting. *Journal of Physical Oceanography, 21*, 1631-1642.

This project has received funding from the Europeans Union's Horizon 2020 research & innovation programme under grant agreement number 101036457.

doi:http://journals.ametsoc.org/doi/pdf/10.1175/1520-0485%281991%29021%3C1631%3AQLTOWW%3E2.0.CO%3B2

Jimenez, P. A. (2015). Mesoscale modeling of offshore wind turbine wakes at the wind farm resolving scale: A composite-based analysis with the Weather Research and Forecasting model over Horns Rev. *Wind Energy*, 559-566.

Jimenez, P. A. (2016). The role of unresolved clouds on short-range global horizontal irradiance predictability. *Monthly Weather Review*, 3099-3107.

Jimenez, P. A.-A. (2016). WRF-Solar: Description and clear-sky assessment of an augmented NWP model for solar power prediction. *Bulletin of the American Meteorological Society*, 1249-1264.

Krishna, D., Vikram, K., & Sreejith, K. (2023). SARAL/AltiKa measurements for geodetic applications: Impact of drifting and mispointing phase data. *Advances in Space Research, 72*, 4021-4030. doi:https://doi.org/10.1016/j.asr.2023.07.032

Lee, J. A. (2016). Solar energy nowcasting case studies near Sacramento. *Weather Forecasting*.

Lekler, F., Ardhuin, F., Filipot, J.-F., & Mironov, A. (2013). Dissipation source terms and whitecap statistics. *Ocean Modelling, 70*, 62-74.

Li, B. a. (2021). Mesoscale modeling of a “Dunkelflaute” event. *Wind Energy*, 5-23.

Marechal, G., & Ardhuin, F. (2021). Surface currents and significant wave height gradients: matching numerical models and high-resolution altimeter wave heights in the Agulhas current region. *Journal of Geophysical Research: Oceans, 126*, e2020JC016564. doi:10.1002/essoar.10505343.1

Mentaschi, L., Besio, G., Cassola, F., & Mazzino, A. (2015). Performance evaluation of Wavewatch III in the Mediterranean Sea. *Ocean Modelling, 90*, 82-94. doi:https://doi.org/10.1016/j.ocemod.2015.04.003

Mulet, S., Rio, M.-H., Etienne, H., Artana, C., Cancet, M., Dibarboure, G., . . . Strub, P. T. (2021). The new CNES-CLS18 global mean dynamic topography. *Ocean Science, 17*, 789-808. doi:10.5194/os-2020-117

Nunalee, C. G. (2014). Mesoscale modeling of coastal low-level jets: implications for offshore wind resource estimation. *Wind Energy*, 1199--1216.

Perignon, Y., Ardhuin, F., Cathelain, M., & Robert, M. (2014). Swell dissipation by induced atmospheric shear stress. *Journal of Geophysical Research, 119*, 6622-6630. doi:10.1002/2014JC009896

Pineau-Guillou, L., Ardhuin, F. B.-N., J.-L. Redelsperger, J.-L., Chapron, B., Bidlot, J., & Quilfen, Y. (2018). Strong winds in a coupled wave-atmosphere model during a North Atlantic storm event: evaluation against observations. *Quarterly Journal of the Royal Meteorological Society, 144*, 317-332. doi:10.1002/qj.3205

This project has received funding from the Europeans Union’s Horizon 2020 research & innovation programme under grant agreement number 101036457.

Piolle, J.-F., Dodet, G., Quilfen, Y., Schwatke, C., Passaro, M., Quartly, G., & Thibaut, P. (2022). ESA Sea State Climate Change Initiative (Sea State cci): Global remote sensing multi-mission along-track significant wave height from altimetry, L2P product, version 3. *NERC EDS Centre for Environmental Data Analysis*. doi:https://dx.doi.org/10.5285/8cb46a5efaa74032bf1833438f499cc3

Port{\'e}-Agel, F. a. (2020). Wind-turbine and wind-farm flows: A review. *Boundary-layer meteorology*, 1-59.

Powers, J. K. (2017). *The weather research and forecasting model: Overview, system efforts, and future directions* (Vol. 98). Bulletin of the American Meteorological Society.

Rascle, N., & Ardhuin, F. (2013). A global wave parameter database for geophysical applications. Part 2: model validation with improved source term parameterization. *Ocean Modelling, 70*, 174-188. doi:10.1016/j.ocemod.2012.12.001

Remmers, T. a. (2019). The potential of advanced scatterometer (ASCAT) 12.5 km coastal observations for offshore wind farm site selection in Irish waters. *Energies*, 206.

Rio, M.-H., Mulet, S., & Picot, N. (2014). Beyond GOCE for the ocean circulation estimate: Synergetic use of altimetry, gravimetry, and in situ data provides new insight into geostrophic and Ekman currents. *Geophysical Research Letters, 41*(24), 8918--8925.

Rodrigo, J. S. (2020). Validation of meso-wake models for array efficiency prediction using operational data from five offshore wind farms. *Journal of Physics: Conference Series, 1618*(6).

Rubner, Y. a. (2000). The earth mover's distance as a metric for image retrieval. *International journal of computer vision*, 99-121.

Russo, M. a. (2023). Future perspectives for wind and solar electricity production under high-resolution climate change scenarios. *Journal of Cleaner Production*, 136997.

Schimanke S., R. M. (2021). *CERRA sub-daily regional reanalysis data for Europe on single levels from 1984 to present. Copernicus Climate Change Service (C3S) Climate Data Store (CDS).* Retrieved 02 16, 2024, from https://doi.org/10.24381/cds.622a565a

Smith, W. H., & Scharroo, R. (2015). Waveform Aliasing in Satellite Radar Altimetry. *{IEEE Trans. on Geoscience and Remote Sensing, 53*, 1671-1682. doi:10.1109/TGRS.2014.2331193

Stopa, J. E., Ardhuin, F., & Girard-Ardhuin, F. (2016). Wave climate in the Arctic 1992-2014: seasonality and trends. *The Cryosphere, 10*, 1605-1629. doi:10.5194/tc-10-1605-2016

This project has received funding from the Europeans Union's Horizon 2020 research & innovation programme under grant agreement number 101036457.

Tolman, H. L. (1991). A third generation model for wind on slowly varying, unsteady and inhomogeneous depth and currents. *Journal of Physical Oceanography, 21*, 766-781. doi:https://doi.org/10.1175/1520-0485(1991)021<0782:ATGMFW>2.0.CO;2

Tolman, H. L. (1992). Effects of numerics on the physics in a third-generation wind-wave model. *Journal of Physical Oceanography, 22*, 1095-1111.

Tolman, H. L. (1995). Subgrid modeling of moveable-bed bottom friction in wind wave models. *Coastal Engineering, 26*, 57-75.

Tolman, H. L. (2008). A mosaic approach to wind wave modeling. *Ocean Modelling, 25*, 35-47. doi:10.1016/j.ocemod.2008.06.005

Vemuri, A. a. (2021). Sensitivity analysis of mesoscale simulations to physics parameterizations: a case study of storm Ciara over the Belgian North Sea using WRF-ARW. *Wind Energy Science*, 1-23.

Zhang, X. a. (2016). Evaluation of the reanalysis surface incident shortwave radiation products from NCEP, ECMWF, GSFC, and JMA using satellite and surface observations. *Remote Sensing, 8*(3).

This project has received funding from the Europeans Union’s Horizon 2020 research & innovation programme under grant agreement number 101036457.

Appendix A: WW3 model switches and namelist

The following model “switches” were activated for WW3 compilation:

NOGRB SCRIP SCRIPNC TRKNC DIST MPI PR3 UQ FLX0 LN1 ST4 STAB0 NL1 BT4 DB1 MLIM TR0 BS0 IC2 IS2 REF1 IG1 WNT2 WNX1 RWND WCOR CRT1 CRX1 TIDE O0 O1 O2 O2a O2b O2c O3 O4 O5 O6 O7

The specific modifications applied to the model namelist, corresponding to the TUD-165 parameters is given below (as used in the input file for WW3):

```
&SIN4 BETAMAX = 1.65 , SWELLF = 0.68, TAUWSHELTER = 0.3,
 SWELLF3 = 0.022,  SWELLF4 = 90000.0, SWELLF7 = 360000.00 /
&SDS4 FXFM3 = 2.5 /
&OUTS P2SF = 1, E3D = 1, I1P2SF = 2, I2P2SF = 36 /
&PRO3 WDTHCG = 1.50, WDTHTH = 1.50  /
&REF1 REFCOAST = 0.05, REFCOSP_STRAIGHT = 4, REFFREQ = 1., REFICEBERG = 0.2,
     REFMAP = 0., REFSLOPE = 2., REFSUBGRID = 0.1, REFRMAX = 0.5 /
&SIC2 IC2DISPER = F, IC2TURB = 0.9 , IC2ROUGH = 0.001, IC2DMAX = 0.3,
     IC2REYNOLDS = 150000, IC2SMOOTH  = 200000., IC2VISC = 2.0  /
&SIS2 ISC1 = 0.2, IS2C2 = 0.000000, IS2C3 = 0. , IS2BACKSCAT = 0.8 ,
     IS2BREAK = T, IS2DUPDATE = F , IS2CREEPB = 0.2E8 , IS2CREEPD = 0.5,
     IS2CREEPN = 3.0, IS2BREAKF = 3.6, IS2WIM1 = 1.0, IS2FLEXSTR = 2.7414E+05,
     IS2CREEPC = 0.4, IS2ANDISE = 0.55 /
&MISC ICEHINIT = 0.8, ICEHMIN = 0.1, CICE0 = 0.25, NOSW =6,
     CICEN = 2.00, LICE = 40000., FLAGTR = 4, FACBERG = 0.2 ,
     WCOR1=20.5, WCOR2=1.04 /
END OF NAMELISTS
```